ACIBADEM MEHMET ALI AYDINLAR UNIVERSITY
GRADUATE SCHOOL OF HEALTH SCIENCES

FUNCTIONAL INVESTIGATIONS OF MUTATIONS IN *CCN6*, PROGRESSIVE PSEUDORHEUMATOID DYSPLASIA GENE, IN CHONDROCYTE CELL LINES

GÜLİPEK GÜVEN TAŞBİÇEN
PH.D. THESIS

DEPARTMENT OF MEDICAL BIOTECHNOLOGY

SUPERVISOR
Prof. Eda TAHİR TURANLI

SECONDARY SUPERVISOR
Prof. Yasemin ALANAY

ISTANBUL-2025

ACIBADEM MEHMET ALI AYDINLAR UNIVERSITY
GRADUATE SCHOOL OF HEALTH SCIENCES

FUNCTIONAL INVESTIGATIONS OF MUTATIONS IN *CCN6*, PROGRESSIVE PSEUDORHEUMATOID DYSPLASIA GENE, IN CHONDROCYTE CELL LINES

GÜLİPEK GÜVEN TAŞBİÇEN

PH.D. THESIS

DEPARTMENT OF MEDICAL BIOTECHNOLOGY

SUPERVISOR
Prof. Eda TAHİR TURANLI

SECONDARY SUPERVISOR
Prof. Yasemin ALANAY

ISTANBUL-2025

DECLARATION

I declare that this thesis work is my own work, I had no unethical behavior at any stages from the planning to the writing of the thesis, I obtained all the information in this thesis in accordance with academic and ethical rules, I cited all the information and comments that were not obtained with this thesis work, and I provided resources in the list of references. I also declare that there was no violation of any patents and copyrights during the study and writing of this thesis.

02.12.2025

Gülipek GÜVEN TAŞBİÇEN

PREFACE AND ACKNOWLEDGEMENT

I would like to express my heartfelt and deepest gratitude to my supervisor, Prof. Eda Tahir Turanlı, for her exceptional mentorship, scientific vision, and constant encouragement throughout this study. Her guidance not only shaped the scientific direction of this work but also inspired me to think critically and persistently in every step of research. I am also sincerely thankful to my co-supervisor, Prof. Yasemin Alanay, for her valuable clinical insight, thoughtful perspectives, and continuous support during the progress of this study.

I am grateful to the Board of Trustees of Acıbadem Mehmet Ali Aydınlar University for their generous support and for providing the infrastructure and academic environment that made this research possible.

My appreciation goes to my colleagues at the HEREAT Lab for their support during the experimental stages. I would like to especially thank Zeynep Tonbul for being by my side during long experiment days, Alper Bülbül for his help with data analyses, and Dr. Dilay Hazal Ayhan for her kind friendship and both scientific and emotional support that made this process lighter and more meaningful.

I am deeply thankful to my beloved husband Koray, whose patience, love, and unwavering belief in me have been my greatest strength throughout this challenging journey. His presence turned even the most difficult moments into calm and courage. I also owe my warmest thanks to my dear parents, Nesrin and Ali Fuat Güven, for their endless love and support, for always standing behind me with faith and kindness, and for reminding me where my roots and motivation truly belong. I am also grateful to my cat Kınalı, whose presence has always made me happy and kept me motivated.

This work was supported by the Scientific and Technological Research Council of Türkiye (TÜBİTAK) under the 1002-A Program (Project No. 222S011), and by the Acıbadem Mehmet Ali Aydınlar University Scientific Research Projects Commission (Project No. ABAPKO 2170).

TABLE OF CONTENTS

ABBREVIATIONS AND SYMBOLS

CCN6	Cellular Communication Network Factor 6
CHOP	C/EBP Homologous Protein
CRP	C-Reactive Protein
CTCK	Cysteine Knot-Containing Domain
ECM	Extracellular Matrix
ESR	Erythrocyte Sedimentation Rate
IGFBP	Insulin-like Growth Factor Binding Protein
JIA	Juvenile idiopathic arthritis
MMP	Matrix Metalloproteinase
OMIM	Online Mendelian Inheritance in Man
PPD	Progressive pseudorheumatoid dysplasia
sXBP1	Spliced X-box Binding Protein 1
TGF-β	Transforming Growth Factor Beta
TSP-1	Thrombospondin Type 1 Repeat
uXBP1	Unspliced X-box Binding Protein 1
WISP3	Wnt1-inducible-signaling pathway protein 3
Wnt	Wingless/Integrated

LIST OF FIGURES

LIST OF TABLES

ABSTRACT

Functional Investigations of Mutations in *CCN6*, Progressive Pseudorheumatoid Dysplasia Gene, in Chondrocyte Cell Lines

Progressive pseudorheumatoid dysplasia (PPD) is a rare cartilage disorder caused by variants in *CCN6* encoding WISP3; however, the role of WISP3 in PPD remains unclear. In this study, variants within the IGFBP domain of WISP3 (p.Cys52*, p.Tyr109*, p.Gly83Glu, and p.Cys114Trp) were overexpressed in primary human chondrocytes (402-05A) to examine cellular homeostasis, extracellular matrix (ECM) regulation, transcriptomic profiles, and protein interactions. The results showed that WISP3 variants influence chondrocyte functions differently. p.Cys52* failed to produce a stable protein and lost function through rapid degradation. p.Gly83Glu showed a modest effect in PPD, with its impact on WISP3 supported by FoldX analysis (+2.73 kcal/mol). p.Cys114Trp exhibited destabilization due to disruption of the Cys92 disulfide bond (+43.33 kcal/mol) and triggered a strong cellular response. In ECM homeostasis, adhesion and wound-healing assays showed reduced collagen binding and reduced suppression of migration compared with overexpression. Zymography suggested that the variants may reduce ECM regenerative capacity. Under ER stress, *s/uXBP1* increased 4.77-fold ($p<0.001$) in p.Cys114Trp and 3.37-fold ($p=0.0022$) in p.Gly83Glu, indicating an adaptive response, whereas p.Tyr109* showed a 2.65-fold ($p=0.0497$) increase in *CHOP* and a 2.63-fold ($p=0.0396$) elevation in the *CHOP/sXBP1* ratio, reflecting apoptotic stress. Transcriptomic data showed that the wild-type upregulated cytoskeleton-related genes, while p.Cys114Trp activated stress and cell-death pathways. Proteomic analyses revealed loss of 61 partners in p.Tyr109* and gain of new partners in p.Cys114Trp. The interaction of WISP3 with CKAP4 suggested a regulatory role in Wnt signaling. Overall, *CCN6* variants elicit distinct cellular responses that may influence WISP3 function and disease progression.

Keywords: Cellular communication network factor 6 (*CCN6*), WNT1-inducible-signaling pathway protein 3 (WISP3), Progressive pseudorheumatoid dysplasia (PPD), Endoplasmic reticulum stress, Proteomics

ÖZET

Kondrosit Hücre Hatlarında Progressif Psödoromatoid Displazi Geni Olan *CCN6*'daki Varyantların Fonksiyonel Analizi

Progressif psödoromatoid displazi (PPD), nadir bir kıkırdak hastalığı olup, WISP3 proteinini kodlayan *CCN6*'deki varyantlardan kaynaklanmaktadır; ancak WISP3'ün PPD'deki rolü henüz tam anlaşılamamıştır. Çalışmada, WISP3'ün IGFBP bölgesindeki varyantlar (p.Cys52*, p.Tyr109*, p.Gly83Glu, p.Cys114Trp) primer insan kondrosit hücrelerinde (402-05A) aşırı eksprese edilerek hücre homeostazı, hücre dışı matriks (ECM) regülasyonu, transkriptom profili ve protein etkileşimleri araştırılmıştır. Bulgular, WISP3 varyantlarının kondrosit fonksiyonlarını farklı düzeylerde etkilediğini göstermiştir. p.Cys52*, stabil protein üretememiş ve degradasyonla işlev kaybetmiştir. p.Gly83Glu'nun PPD'deki etkisi sınırlı kalmış ve WISP3 üzerindeki etkisi FoldX ile de gösterilmiştir (+2.73kcal/mol). p.Cys114Trp ise Cys92 disülfit bağının bozulmasıyla destabilizasyon göstermiş (+43.33kcal/mol) ve güçlü bir hücresel yanıt oluşturmuştur. ECM homeostazında, tutunma ve yara kapanma analizlerinde varyantların kolajene tutunma kapasitesi ve hücre göçünü baskılaması, aşırı ekspresyona kıyasla azalmıştır. Zimografi analizi, varyantların ECM'in rejeneratif kapasitesini azaltabileceğini göstermiştir. Endoplazmik retikulum stresinde ise *s/uXBP*, p.Cys114Trp'de 4,77 kat ($p<0.001$) ve p.Gly83Glu'da 3,37 kat ($p=0.0022$) artarak adaptif, p.Tyr109* ise *CHOP* 2,65 kat ($p=0.0497$) ve *CHOP/sXBP1* 2,63 kat ($p=0.0396$) artarak apoptotik stres yanıtını oluşturmuştur. Yabanıl tip, transkriptom düzeyinde hücre iskeletinin organizasyonuyla ilişkili gen seviyelerini artırırken, p.Cys114Trp stres ve hücre ölümüyle ilişkili yolakları aktive etmiştir. Proteomik analizlerde, p.Tyr109* 61 etkileşim partnerini kaybederken, p.Cys114Trp, yeni partner kazanımı sergilemiştir. Ayrıca WISP3'ün CKAP4 ile etkileşiminin Wnt yolağında düzenleyici bir rol oynayabileceğini düşündürmüştür. Sonuç olarak, *CCN6*'deki varyantların farklı hücresel yanıtlar oluşturduğu, bunun hem WISP3'ün fonksiyonunu hem de hastalığın seyrini etkileyebileceği öngörülmektedir.

Anahtar Sözcükler: Hücresel iletişim ağı faktörü 6 (*CCN6*), WNT1 ile uyarılabilir sinyal yolağı proteini 3 (WISP3), Progressif psödoromatoid displazi (PPD), ER stresi, Protein-protein etkileşimi

1 INTRODUCTION AND AIM

Progressive pseudorheumatoid dysplasia (PPD, OMIM: 208230) is a rare, autosomal recessive skeletal disorder characterized by progressive joint stiffness, pain, and deformities, primarily affecting articular cartilage (1). It is caused by biallelic variants in *Cellular Communication Network Factor 6* (*CCN6)* (2). The *CCN6* gene, located on chromosome 6q21, encodes WNT1-inducible signaling pathway protein 3 (WISP3), a 354-amino-acid matricellular protein predominantly expressed in chondrocytes and essential for maintaining cartilage integrity (3). Pathogenic variants in *CCN6* lead to the loss or functional alteration of WISP3, thereby impairing its regulatory role in cartilage homeostasis.

Clinically, PPD is often misdiagnosed in early stages as juvenile idiopathic arthritis or other inflammatory arthropathies, due to overlapping features such as joint swelling and restricted movement, but lacking signs of systemic inflammation (4,5). While plain radiography can reveal characteristic features such as epiphyseal enlargement and joint space narrowing, these findings alone are insufficient to distinguish PPD from other skeletal dysplasias (4). Therefore, the most accurate diagnosis is achieved by combining radiographic assessment with molecular genetic analysis, most commonly next-generation sequencing or targeted gene sequencing (6).

CCN6 belongs to the CCN family of matricellular proteins, which are involved in various biological processes including cell adhesion, migration, proliferation, and differentiation (7). It interacts with extracellular matrix (ECM) components and signaling molecules, modulating key pathways including Wnt, BMP, and IGF (8–10). Dysregulation of these pathways can impair chondrocyte function, disrupt ECM composition, and promote premature cartilage degeneration (11). Among these, the Wnt pathway is particularly critical for skeletal development, regulating chondrocyte proliferation, differentiation, and matrix production; its aberrant activation or suppression compromises cartilage integrity and bone formation, contributing to disorders such as PPD (12).

WISP3 plays a central role in maintaining cartilage homeostasis by promoting type II collagen and aggrecan synthesis, while also supporting intracellular signaling mechanisms essential for chondrocyte health (13). Deficiency or dysfunction of this protein has been linked to mitochondrial impairment and increased reactive oxygen species (ROS) generation, suggesting a connection between extracellular matrix regulation and cellular stress responses (14,15).

The estimated prevalence of PPD is approximately 1 in 1,000,000 individuals (3,16,17). In populations with a high rate of consanguinity, such as Türkiye, PPD appears to be more common, although its exact prevalence remains unknown. Approximately half of all reported PPD alleles in Turkish families correspond to the c.156C>A (p.Cys52*) nonsense variant. In these families, all individuals carrying the c.156C>A (p.Cys52*) allele were also found to carry the c.248G>A (p.Gly83Glu) variant, both located in exon 2, suggesting a possible founder effect (3,17). Additional pathogenic variants, including c.327C>A (p.Tyr109*) and c.342T>G (p.Cys114Trp), have been reported, though their cellular and molecular consequences are not fully understood (3).

This study aims to investigate four *CCN6* variants: p.Cys52*, p.Tyr109*, p.Gly83Glu, and p.Cys114Trp, located within the IGFBP domain, using human chondrocyte cell culture models. Their effects on extracellular matrix (ECM) dynamics, endoplasmic reticulum stress, mitochondrial redox balance, gene expression profiles, and protein–protein interaction networks were assessed. By comparing nonsense and missense variants, their impact on WISP3 stability, subcellular localization, and interaction partners was evaluated, alongside their variant-specific influence on ECM remodeling and cellular stress pathways. Transcriptomic and proteomic datasets were obtained together to identify converging and divergent mechanisms contributing to PPD pathogenesis.

As one of the first multidimensional functional assessments of (p.Cys52*, p.Gly83Glu, p.Tyr109*, p.Cys114Trp) *CCN6* variants in human chondrocytes, this study provides a comprehensive framework for understanding genotype–phenotype

correlations, providing molecular insights into PPD, and identifying potential molecular targets for the development of future therapeutic strategies.

2 BACKGROUND

2.1 Genetics of Skeletal Dysplasias

Skeletal dysplasias, also termed osteochondrodysplasias, comprise a large and heterogeneous group of heritable disorders affecting bone and cartilage growth, matrix composition, and development (18). Although each individual condition is rare, their collective prevalence is estimated at approximately 1 in 5,000 live births (19). The phenotypic spectrum is broad, ranging from perinatally lethal forms to non-lethal types that manifest in infancy or childhood with disproportionate short stature, linear growth failure, joint deformities, and locomotor impairment. Importantly, disease manifestations may evolve throughout life, with some forms leading to premature osteoarthritis, skeletal deformities, or functional disability.

More than 450 distinct entities are currently recognized under the classification of the International Skeletal Dysplasia Society (ISDS), and this number continues to expand with advances in molecular genetics (20). Classification relies heavily on radiographic patterns, grouped broadly into epiphyseal, metaphyseal, altered-density, and miscellaneous categories (18). A systematic radiologic work-up typically begins with a complete skeletal survey, including both axial and appendicular views (21). Early childhood imaging, prior to epiphyseal fusion, is particularly informative.

Skeletal dysplasias exemplify both locus and allelic heterogeneity: clinically similar phenotypes can arise from variants in different genes, and distinct variants within a single gene may yield divergent phenotypes. For example, variants in *FGFR3* lead to a spectrum of disorders including hypochondroplasia, achondroplasia, and the perinatally lethal thanatophoric dysplasia, whereas different *COL2A1* variants range from lethal achondrogenesis type II to milder Stickler syndrome. Inheritance patterns include autosomal dominant, autosomal recessive, and X-linked forms (22–24).

At the molecular level, skeletal dysplasias often result from disruptions in signaling pathways fundamental to cartilage and bone biology, including Wnt, TGF-β/BMP, FGFR, and Hedgehog. Dysregulation of these pathways impairs chondrocyte

proliferation, differentiation, extracellular matrix organization, and endochondral ossification, ultimately leading to growth disturbances and skeletal deformities (25–27). Consistent with this, variants in genes encoding components of these pathways can also give rise to skeletal dysplasia. Intracellular control systems, including endoplasmic reticulum (ER) folding capacity, ER-associated degradation, and the unfolded protein response, are frequently engaged by dysplasia-associated variants and can secondarily compromise chondrocyte survival and the integrity of growth plate structure (28). Given that cartilage provides the template for endochondral bone formation, chondrocyte dysfunction is a critical pathogenic mechanism in many subtypes, including those linked to the CCN family of matricellular proteins (29).

Despite the utility of radiological features, significant overlap between subtypes often complicates differential diagnosis. Therefore, molecular testing has become indispensable for accurate classification and for correlating genotypes with phenotypes. The increasing application of next-generation sequencing has accelerated the discovery of novel disease-causing variants and facilitated genotype–phenotype correlations, thereby strengthening the understanding of these relationships.

Beyond their clinical significance, skeletal dysplasias provide valuable models for studying the molecular regulation of cartilage and bone development. Insights gained from these disorders contribute to a broader understanding of skeletal homeostasis and the consequences of dysregulated signaling throughout growth and maintenance.

2.2 Progressive Pseudorheumatoid Dysplasia

Progressive pseudorheumatoid dysplasia (PPD) is a rare skeletal dysplasia primarily affecting articular cartilage, with onset in childhood and lifelong progression. Affected individuals are typically normal at birth and during early development; clinical manifestations usually emerge between the ages of 3 and 8 years, most often presenting as bony-appearing swelling and restricted mobility of the small joints of the hands(30). Over time, larger joints, including the wrists, elbows,

knees, hips, and ankles, also become involved. Pain is often mild during early disease stages but increases with age as secondary degenerative changes develop (31).

The main diagnostic challenge lies in differentiation from juvenile idiopathic arthritis (JIA). In contrast to JIA, patients with PPD typically demonstrate normal C-reactive protein (CRP) and erythrocyte sedimentation rate (ESR) levels, negative tests for rheumatoid factor, anti-double stranded DNA, and antinuclear antibodies, and show limited response to immunosuppressive therapies (32,33). These features support the need for molecular confirmation by sequencing *CCN6*, which is essential for distinguishing PPD from JIA and preventing misdiagnosis.

Despite the absence of inflammatory markers, PPD is characterized by a progressive course that ultimately leads to substantial joint deformity and functional limitation. Radiological findings generally reflect structural alterations of cartilage and bone rather than synovial inflammation, and degenerative changes tend to accumulate with age (3). This clinical profile indicates that PPD represents a primary disorder of cartilage maintenance rather than an immune-mediated arthropathy (34) . Accordingly, understanding how *CCN6* dysfunction affects chondrocyte behavior is critical for elucidating the molecular basis of disease progression.

2.2.1 Classical genetics of progressive pseudorheumatoid dysplasia

Classical genetic studies of progressive pseudorheumatoid dysplasia (PPD) have primarily focused on defining the mode of inheritance, familial segregation patterns, and population-level characteristics of the disease through pedigree analyses and epidemiological observations. These approaches have been fundamental in establishing PPD as a rare monogenic disorder inherited in an autosomal recessive manner (16). Consistent with classical genetic observations, pedigree analyses across multiple independent studies demonstrate that PPD follows an autosomal recessive mode of inheritance, characterized by unaffected carrier parents, recurrence among siblings, and enrichment in consanguineous families. The cases examined in the present study are concordant with this established pattern (35–37).

Consanguinity and the occurrence of multiple affected siblings within the same family are frequently reported, with both sexes affected equally (17). The condition is rare across most populations, with a prevalence of approximately 1 in 1,000,000 (38). However, its geographic distribution is uneven: higher frequencies of familial clustering and founder variants have been described in regions such as the Middle East, North Africa, Turkey, and South Asia, where consanguinity rates are relatively elevated (3,39). This geographic heterogeneity has been attributed, at least in part, to founder effects documented in specific populations. Notably, Delague et al. described a founder variant in Middle Eastern families of Lebanese, Syrian, and Palestinian origin, in which affected individuals were homozygous for the c.156C>A (p.Cys52*) variant. In several of these families, this variant was consistently observed in linkage with c.248G>A (p.Gly83Glu), providing strong evidence for inheritance from a common ancestor (17). Supporting this notion, subsequent reviews have reported an increased frequency of PPD in endogamous populations, highlighting the contribution of population-specific genetic enrichment to disease prevalence (17,40).

2.2.2 Molecular genetics of progressive pseudorheumatoid dysplasia

Progressive pseudorheumatoid dysplasia (PPD) was first described in 1982 by Ruth Wynne-Davies and colleagues, who recognized it as a distinct skeletal dysplasia based on characteristic clinical and radiological features (41). In 1999, an international research group led by Matthew L. Warman mapped the disease locus to chromosome 6q21 and demonstrated that biallelic pathogenic variants in Cellular Communication Network Factor 6 (*CCN6*) are responsible for PPD (42). This discovery marked a turning point, transforming PPD from a clinically defined syndrome into a disorder with an established molecular basis that can be definitively diagnosed through genetic testing.

This gene encodes WISP3 (WNT1-inducible signaling pathway protein 3), a cysteine-rich secreted matricellular protein and a member of the CCN protein family (43). *CCN6* is located on chromosome 6q21, with precise genomic coordinates 6:112,054,104–112,069,686 on the forward strand of the GRCh38/hg38 reference

assembly (44). Among several annotated transcript isoforms, the most commonly referenced protein-coding transcript of CCN6 (CCN6-203; ENST00000368666.7) comprises five coding exons and gives rise to a transcript of approximately 1,385 base pairs in length (Figure 1). The structural organization of *CCN6* supports the synthesis of WISP3, which exerts extracellular regulatory functions in cartilage homeostasis.

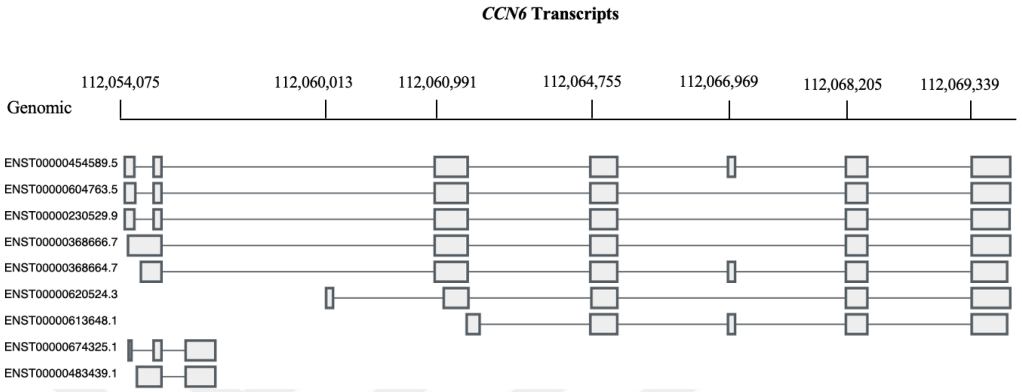

Figure 1. Schematic representation of *CCN6* transcript structures based on GTEx annotation. Exons are shown as boxes and introns as connecting lines, with genomic coordinates indicated along the top. The data used for the analyses described in this thesis were obtained from the GTEx Portal on 2 November 2025 (45).

A broad spectrum of pathogenic variants in *CCN6* has been identified across different populations (Table 1) (3,31,40). These include nonsense variations, which prematurely terminate protein synthesis and generate truncated proteins; frameshift variations, which disrupt the reading frame and result in aberrant translation products; missense variations, most commonly affecting conserved cysteine residues essential for correct disulfide-bond formation and protein folding; splicing variations, which interfere with proper RNA processing; and exon-level deletions or insertions, including exon 1 deletions, which abolish the production of a functional protein (3,40,46). Although the spectrum of variants is diverse, they converge on a common outcome: disruption of WISP3 function leading to a largely uniform clinical phenotype.

Recurrent variants have been described with notable population-specific distributions. The p.Cys52* nonsense variation is the most frequent pathogenic allele in families from the Mediterranean basin, including Türkiye, and has also been

reported in Italy, France, Lebanon, Syria, Germany, and India. The p.Cys61Phe missense variant has been observed in Polish cohorts, whereas p.Cys337Tyr is among the most common alleles in Indian patients. Additional recurrent changes include p.Cys114Trp in Chinese families and p.Tyr109* in Turkish families. Representative frameshift variants comprise p.Pro62Leufs*4 and p.Glu243Lysfs*34, both reported in Turkish patients, while rare large insertion–deletion events such as c.621_622delAinsT (p.Lys207Asnfs*25) and exon 1 deletions in Iranian kindreds further expand the variation spectrum (3,40,46). Collectively, these findings indicate that while the variant spectrum encompasses diverse variation classes, the clinical phenotype remains largely uniform, underscoring the requirement for intact and correctly folded WISP3 protein in cartilage homeostasis.

Table 1. Pathogenic *CCN6* (WISP3) variants reported in PPD across different populations

Variant	Variant Type	Population	HGMD Accession	dbSNP ID	Allele Frequency	Reference
c.43_44delGC (p.Ala15Thrfs*17)	Frameshift	USA	CD991937	–	-	Hurvitz et al., 1999
c.48+2dupT (IVS2+2T)	Splicing	Multi-ethnic	CI994276	rs797044439	0.000001240	Garcia-Segarra et al., 2012
c.156C>A (p.Cys52*)	Nonsense	Türkiye, Iran, India, France, Italy, Lebanon, Syria and Germany	CM991252	rs121908901	0.00002354	Sailani et al., 2018; Garcia-Segarra et al., 2012
c.182G>T (p.Cys61Phe)	Missense	Poland	CM126432	–	-	Garcia-Segarra et al., 2012
c.233G>A (p.Cys78Tyr)	Missense	India	CM129533	–	-	Bhavani et al., 2015
c.246delA (p.Glu84Lysfs*21)	Frameshift	Saudi Arabia, Jordan	CD991938	rs797044438	N/A	Hurvitz et al., 1999
c.248G>A (p.Gly83Glu)	Missense	Türkiye, Syria, Lebanon, China, India	CM129541	rs147337485	0.00135700	Garcia-Segarra et al., 2012
c.327C>A (p.Tyr109*)	Nonsense	Türkiye	CM126423	rs145747429	N/A	Garcia-Segarra et al., 2012
c.342T>G (p.Cys114Trp)	Missense	China, Other Asian	CM118811	rs1776514016	N/A	Yan et al., 2016
c.1013A>T (p.Gln338Leu)	Missense	Japan	CM078552	rs587640965	0.00002231	Nakamura et al., 2007
c.677G>T (p.Gly226Val)	Missense	UK	CM126434	–		Garcia-Segarra et al., 2012
c.868_869delAG (p.Ser290Leufs*12)	Frameshift	Italy, Belgium	CD159638	–		Garcia-Segarra et al., 2012
c.1010G>A (p.Cys337Tyr)	Missense	India	CM126436	rs781986930	0.00001673	Dalal et al., 2012

Functionally, the loss of WISP3 leads to reduced synthesis of type II collagen and aggrecan in chondrocytes, disruption of matrix integrity, and impaired ECM–cell interactions (13). This provides a biological rationale for the progressive weakening of articular cartilage in the absence of systemic inflammation. The demonstration that WISP3 is expressed in articular chondrocytes further supports the biological rationale for why its deficiency predominantly affects the skeletal system, and particularly the joints (13).

In molecular diagnostics, sequencing of the *CCN6* represents the gold standard. Currently, either Sanger sequencing or next-generation sequencing–based skeletal dysplasia panels are employed. When single-allelic variants are detected, exon-level deletion/duplication analysis and segregation studies in family members are required to establish a definitive diagnosis. Early genetic confirmation is essential to avoid diagnostic uncertainty, guide appropriate clinical management and ensures accurate genetic counseling for affected families.

2.3 Cellular Communication Network Factors (CCN)

The CCN protein family consists of six cysteine-rich, secreted matricellular proteins: cysteine-rich angiogenic inducer 61 (CYR61/CCN1), connective tissue growth factor (CTGF/CCN2), nephroblastoma overexpressed (NOV/CCN3), and the WNT1-inducible signaling pathway proteins WISP1 (CCN4), WISP2 (CCN5), and WISP3 (CCN6) (43). The acronym “CCN” was originally derived from the initial letters of the first three identified members—CYR61, CTGF, and NOV (47). Three additional homologous cysteine-rich, Wnt-inducible proteins (CCN4, CCN5, CCN6) were subsequently recognized, and together with CCN1–3 they are now referred to as the CCN family. More recently, the nomenclature has also been interpreted as standing for “Cellular Communication Network,” highlighting the intercellular signaling roles of different CCN family members and the importance of their precise regulation (48). Phylogenetic analysis further illustrates the evolutionary relationships among CCN family members, highlighting both their shared ancestry and divergence within the family (Figure 2) (49).

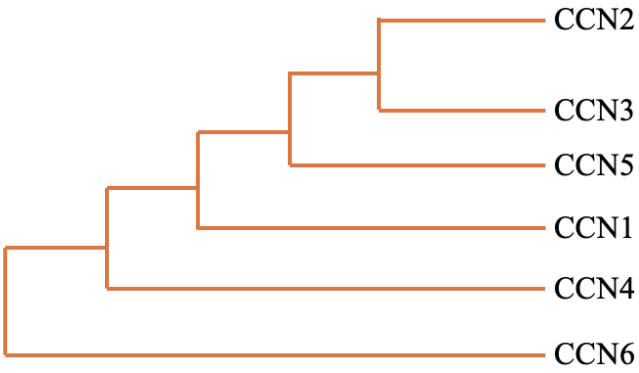

Figure 2. Phylogenetic dendrogram illustrating the evolutionary relationships among the six CCN proteins

These proteins interact with the ECM and play key regulatory roles in diverse biological processes, including cell adhesion, migration, proliferation, differentiation, angiogenesis, chondrogenesis, wound healing, fibrosis, and tumorigenesis (48,50,51). The functions of CCN proteins are complex, as they can exert either stimulatory or inhibitory effects depending on the cellular context. For instance, CCN1 and CCN2 typically promote cell proliferation, whereas CCN3 and CCN5 have been proposed to act as a growth inhibitor (52–54). This functional diversity arises from their modular architecture and the ability to engage in multiple molecular interactions with regulatory proteins and ligands.

Defining feature of CCN proteins is their conserved mosaic organization composed of four modular domains. Generally, CCN protein contains an N-terminal signal peptide followed by (i) an insulin-like growth factor binding protein (IGFBP)-like module, (ii) a von Willebrand factor type C (vWC), (iii) a thrombospondin type 1 (TSP-1), and (iv) a cysteine knot–containing C-terminal (CTCK) domain (Figure 3). These domains share structural similarities with functional regions of other regulatory proteins. CCN5 (WISP2) represents an exception, as it lacks the CT domain, while CCN6 (WISP3) uniquely lacks the vWC domain (8,10)**.** This modular design enables CCN proteins to bind integrins, heparan sulfate proteoglycans (HSPGs), growth factors such as bone morphogenetic proteins (BMPs) and transforming growth factor-beta (TGF-β), as well as ECM components such as fibronectin (55–57).

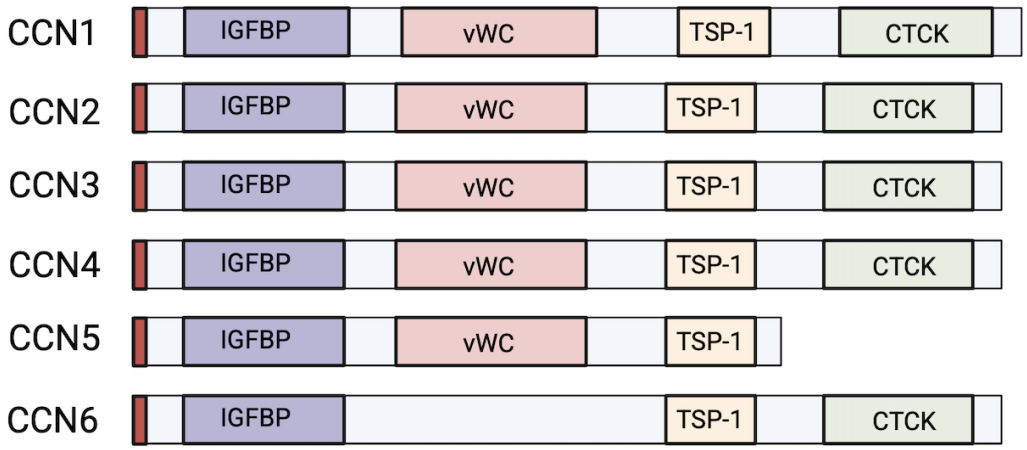

Figure 3. Domain composition of CCN family proteins (CCN1–CCN6). Created in BioRender.com.

Members of the CCN family are critically involved in skeletal development and cartilage–bone homeostasis, but their roles extend far beyond the musculoskeletal system. Depending on the tissue context and expression pattern, CCN proteins have been associated with a wide range of pathological conditions, including fibrotic disorders and various cancers. Accordingly, transcript- and protein-level expression analyses reveal that CCN6 is differentially expressed across a wide range of human tissues, indicating that its biological activity is not restricted to cartilage but extends to diverse tissue contexts (Figure 4).

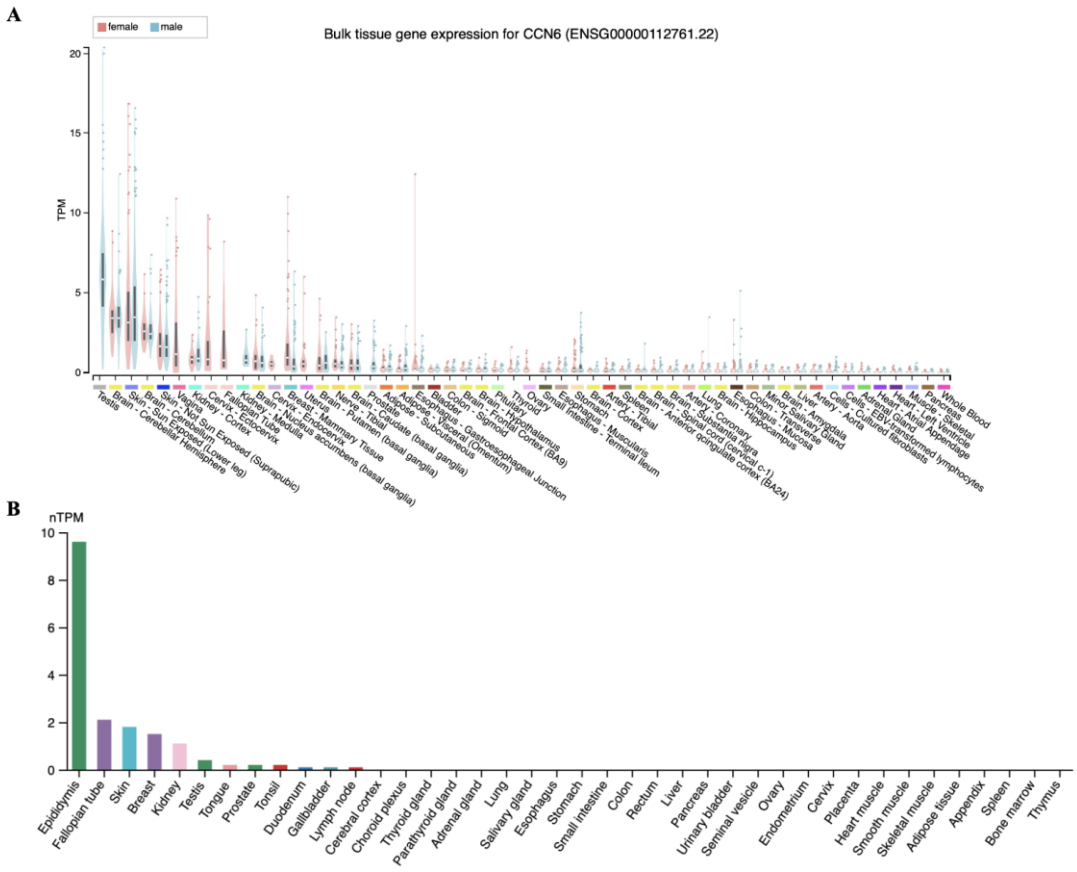

Figure 4. Tissue-specific expression of *CCN6* at the transcript and protein levels. (A) *CCN6* transcript expression across human tissues based on bulk RNA-sequencing data from the GTEx Portal (TPM) ; GTEx Analysis Release V10, dbGaP accession phs000424.v10.p2; last accessed 5 November 2025) (45). (B) WISP3 protein expression across human tissues based on data from the Human Protein Atlas (nTPM; last accessed 5 November 2025) (58).

Importantly, the biological effects of each family member are not uniform but vary according to developmental stage, cellular environment, and the presence of genetic variants. This context-dependence underscores the complexity of CCN protein functions and explains why alterations in their expression or sequence can lead to diverse disease outcomes.

2.3.1 WNT-1 inducible signaling pathway protein 3

WNT-1 inducible signaling pathway protein 3 (WISP3) is a cysteine-rich matrix protein encoded by the *CCN6*. WISP3 consists of approximately 354 amino acids, with

a molecular weight of ~ 39 kDa. At its N-terminus, WISP3 contains a signal peptide spanning residues 1–23. This segment directs the protein to the endoplasmic reticulum, facilitates processing through the secretory pathway, and is proteolytically removed to yield a functional protein (59). In addition to targeting secretion, the signal peptide ensures proper folding, disulfide bond formation, and preparation for extracellular interactions (60). WISP3 is not confined to the ECM; localization studies have also identified it in the cytoplasm and mitochondria of chondrocytes (14,61). This dual localization suggests that WISP3 may act at both the extracellular level, by supporting ECM integrity, and intracellularly, by contributing to metabolic balance.

The protein contains three well-defined functional domains. The IGFBP-like domain (44–117 aa) has the potential to bind IGF1, although this interaction is inefficient when the domain acts alone; effective binding requires the full-length protein and contributions from other domains (62). The TSP domain (208–253 aa) can associate with sulfated glycosaminoglycans and serves as an interaction site for integrins and heparan sulfate proteoglycans, while peptide fragments derived from this region have been shown to inhibit endothelial cell proliferation and migration (55,56). The CTCK domain (268–342 aa) contains a cysteine knot motif that supports structural stabilization through disulfide bonds and may participate in interactions with receptors such as integrins, HSPGs, Notch1, and LRP6 (48,56,62) (Figure 5).

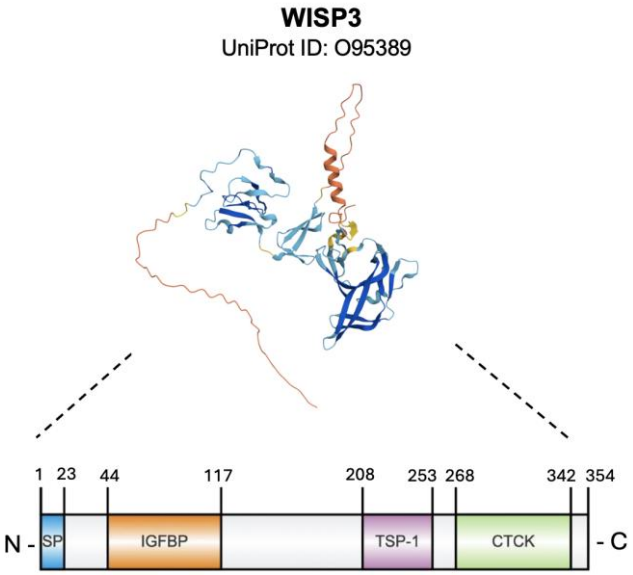

Figure 5. Structural representation of WISP3. The upper panel shows the predicted three-dimensional structure of human WISP3 (UniProt ID: O95389). The lower schematic illustrates the domain organization of WISP3 (58)

Expression of WISP3 is particularly enriched in cartilage tissue (63). It plays a role in cartilage homeostasis during both embryonic and postnatal stages, while additional studies have also reported its expression in the liver, breast tissue, and certain tumors (50,64,65). This distribution indicates that although WISP3 is most prominent in cartilage, it is also expressed in other tissues.

Functionally, disease-associated variants in *CCN6* impair WISP3 expression, folding, secretion, and/or binding interactions, thereby partially or completely compromising protein function. In PPD, incomplete WISP3 activity leads to reduced type II collagen and aggrecan synthesis, loss of ECM integrity, and disordered cell–matrix interactions. As a result, chondrocytes become more susceptible to mechanical loading, and intracellular homeostasis is disrupted, leading to progressive degenerative changes in cartilage.

Beyond skeletal dysplasia, WISP3 has also been linked to oncologic processes. Some reports suggest that reduced WISP3 expression may exert tumor-suppressive effects in breast and other solid tumors by constraining proliferation (2). Conversely, in certain contexts overexpression has been associated with tumor progression (66).

These opposing observations underscore the context-dependent nature of WISP3 function, shaped by cell type, microenvironment, and interaction partners.

2.4 Cartilage Tissue and Extracellular Matrix

Cartilage is a mesenchyme-derived connective tissue that is both aneural and avascular, and its highly hydrated ECM enables it to bear and distribute mechanical loads (67). Histologically, cartilage is classified into three types: hyaline cartilage, elastic cartilage, and fibrocartilage. The most common form, hyaline cartilage, is composed of a dense network of collagen fibrils interwoven with proteoglycan aggregates rich in aggrecan (68). Elastic cartilage preserves the general architecture of hyaline cartilage but gains elasticity and shape memory due to a dense elastin fiber network (69). In fibrocartilage, chondrocytes are located between thick bundles of collagen, predominantly type I with variable amounts of type II; this structure provides resistance to tensile and compressive forces in regions such as the intervertebral discs and menisci (70). These structural differences allow each subtype to meet distinct mechanical requirements, while all share common ECM and cellular features.

Articular cartilage, a specialized subtype of hyaline cartilage, covers the terminal surfaces of synovial joints. It exhibits a highly organized zonal architecture, consisting of superficial, middle, deep, and calcified zones separated by the tidemark, each characterized by distinct chondrocyte morphology and extracellular matrix composition (Figure 6) (71). Its collagen- and proteoglycan-rich matrix facilitates low-friction movement and serves a load-bearing function (72). This function critically depends on the integrity of the collagen network and aggrecan content; disruption of either rapidly compromises joint biomechanics and accelerates degenerative processes. Similarly, defects in molecular pathways that regulate matrix synthesis, organization, and degradation can predispose to cartilage diseases in both childhood and adulthood.

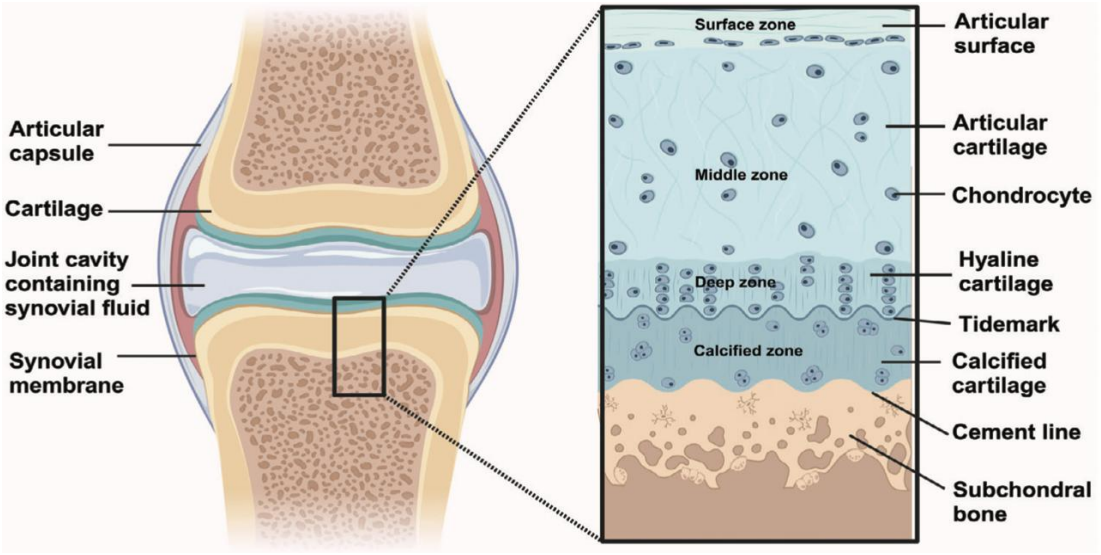

Figure 6. Articular joint anatomy and zonal organization of articular cartilage (71).

The extracellular matrix (ECM) is the principal determinant of cartilage integrity and function. It consists of collagen and elastin fibers, as well as linker proteins such as fibronectin and laminin, and proteoglycans bearing glycosaminoglycan chains (73). In adult cartilage, the capacity for remodeling is limited, and damage to the collagen network is largely irreversible. Loss of aggrecan or disruption of the collagen framework increases permeability, decreases stiffness, and elevates friction; these changes impair load distribution and accelerate structural failure. Preservation of matrix composition therefore relies on a balance between chondrocyte-driven synthesis and degradation, and disturbance of this balance contributes to both degenerative joint diseases and inherited skeletal dysplasias.

Chondrocyte function is context dependent. These cells synthesize and maintain the ECM, thereby sustaining the mechanical properties of the tissue (74). Loss of homeostatic control shifts the balance from matrix synthesis to degradation. Early aggrecan depletion and disruption of the collagen network increase permeability, reduce fluid pressurization, and raise friction, thereby weakening load-bearing capacity and accelerating structural collapse. Oxidative and inflammatory signals further stimulate catabolic enzymes while suppressing anabolic programs, leading to progressive ECM degradation and disruption of zonal architecture. In growth plates,

impaired proliferation, matrix secretion, and terminal hypertrophy hinder longitudinal bone growth and result in skeletal deformities.

2.5 Pathways and Cellular Processes Involving WISP3

2.5.1 Wnt/β-Catenin signaling in chondrocytes

The Wnt signaling pathway is an evolutionarily conserved cascade that regulates fundamental biological processes such as embryonic development, cell proliferation, differentiation, migration, and tissue homeostasis (75). The precise regulation of this pathway is critical for skeletal development and the maintenance of articular cartilage integrity. Dysregulation of Wnt signaling plays a central role in the pathogenesis of degenerative cartilage disorders, most notably osteoarthritis (OA) (76). Within this signaling network, regulatory proteins such as WISP3 serve as key factors in preserving cartilage homeostasis.

Wnt signaling is generally divided into two major branches based on intracellular mechanisms: canonical (β-catenin–dependent) and non-canonical (β-catenin–independent) pathways (77). In the canonical pathway, β-catenin is continuously phosphorylated by a destruction complex consisting of APC, Axin, GSK-3β, and CK1α in the absence of Wnt ligands, leading to its proteasomal degradation (78). When Wnt ligands bind to Frizzled (FZD) receptors and LRP5/6 co-receptors, activation of Dishevelled (DVL) inhibits the destruction complex, allowing β-catenin to accumulate in the cytoplasm and translocate into the nucleus (79) (Figure 7). Nuclear β-catenin then interacts with TCF/LEF transcription factors to induce the expression of target genes, including c-Myc and Cyclin D1, which regulate proliferation and differentiation (79).

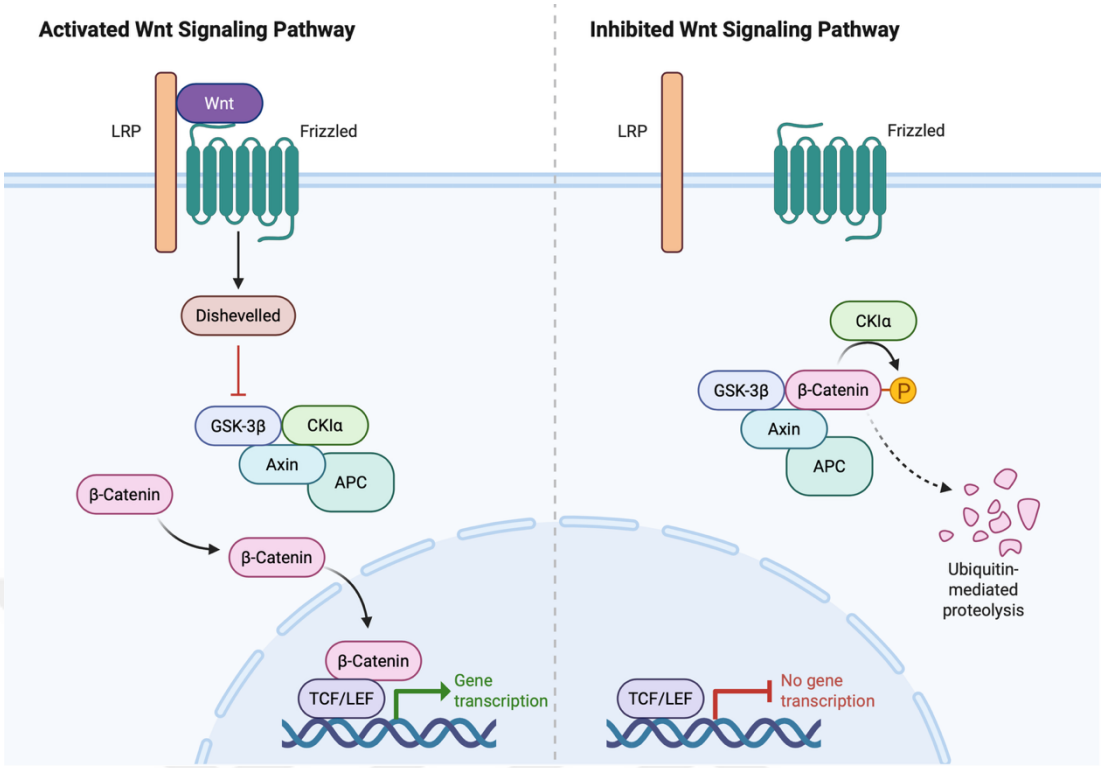

Figure 7. Overview of canonical Wnt/β-catenin signaling. Activation and inhibition states of the pathway are shown. Created in BioRender.com (80).

The non-canonical, β-catenin–independent pathways control cell polarity and migration (77). Among these, the Wnt/planar cell polarity (PCP) pathway regulates cytoskeletal reorganization and contributes to the columnar organization of growth plate chondrocytes (Figure 8). Ligand binding to FZD and co-receptors such as ROR1/2 or RYK leads to DVL-mediated activation of small GTPases, including Rho and Rac, which subsequently stimulate kinases such as JNK. Another branch, the Wnt/Ca^{2+} pathway, modulates intracellular calcium levels via FZD receptor–mediated activation of G-proteins and phospholipase C (12). This process enhances Ca^{+2} release and activates calcium-sensitive proteins including PKC, CaMKII, and NFAT, thereby influencing cell adhesion and directed migration (75,77,78).

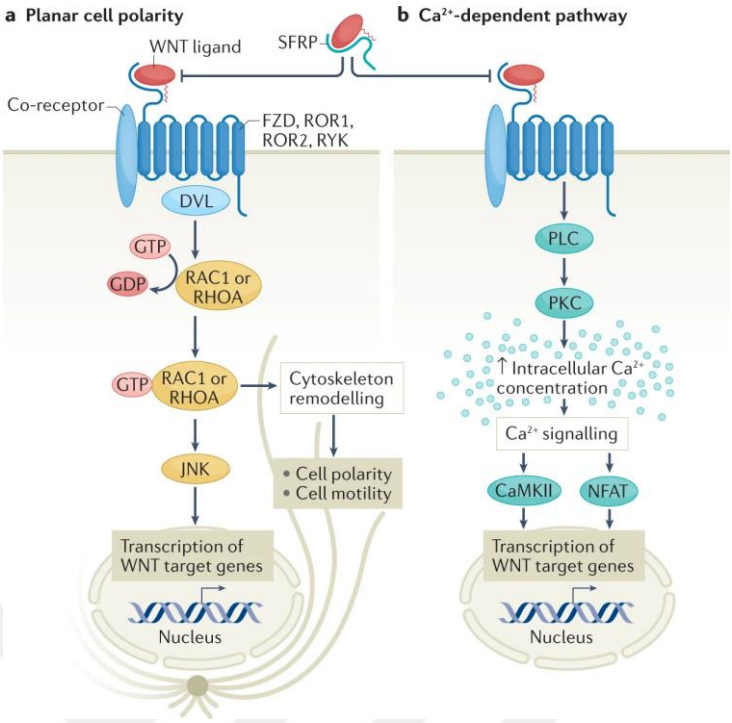

Figure 8. Non-canonical WNT signaling pathways. The planar cell polarity pathway (A) and the Ca^{2+}-dependent pathway (B) are shown.

In cartilage, the effects of Wnt/β-catenin signaling are context dependent. During embryonic development, this pathway is indispensable for joint formation, cartilage template patterning, and endochondral ossification. In contrast, in adult articular cartilage, canonical Wnt activity must remain low to preserve tissue integrity. Pathological overactivation induced by aging, mechanical stress, or inflammation contributes to disease pathogenesis by triggering detrimental changes in chondrocytes. These include hypertrophic differentiation characterized by collagen expression, which is associated with *SOX9* suppression and *RUNX2* activation; matrix degradation mediated by increased production of MMP-13 and ADAMTS-5; and phenotypic shift toward a fibroblast-like morphology, with reduced type II collagen synthesis and increased collagen expression (76,81).

Within this framework, WISP3 acts as an important negative regulator of the Wnt/β-catenin pathway in cartilage. Secreted as a matricellular protein by chondrocytes, WISP3 interacts with Frizzled and LRP6 receptors, thereby preventing

ligand binding or disrupting receptor complex formation to suppress downstream signaling (82).

2.5.2 TGF-β and BMP signaling pathways

The structural integrity and physiological function of articular cartilage rely on homeostasis, a dynamic balance between ECM synthesis (anabolism) and degradation (catabolism) orchestrated by chondrocytes (83). Among the signaling pathways that govern this delicate equilibrium, members of the Transforming Growth Factor-Beta (TGF-β) superfamily play a central role. Within this family, TGF-βs and Bone Morphogenetic Proteins (BMPs) exert fundamental, yet often opposing, influences during cartilage development and in the maintenance of tissue integrity throughout life. Disruptions in these pathways are thought to contribute directly to the pathogenesis of skeletal dysplasias (84).

Both TGF-β and BMP signals stimulate the anabolic activity of chondrocytes, which are indispensable for cartilage function. Collagen provides tensile strength, whereas aggrecan, through its water-binding capacity, confers resistance to compressive loads. In this way, these pathways support the biomechanical properties that enable cartilage to bear weight and facilitate smooth, low-friction movement within the joint (83).

Despite these shared anabolic effects, their roles diverge in the regulation of chondrocyte phenotype. TGF-β signaling, primarily through the SMAD2/3 axis, maintains the stable phenotype of articular chondrocytes and suppresses terminal differentiation into hypertrophic cells (Figure 9). Hypertrophy, a process that drives matrix mineralization and degradation, is kept in check by TGF-β through inhibition of RUNX2, the key transcription factor promoting this transition. In contrast, BMP signaling acts via SMAD1/5/8 to accelerate chondrocyte differentiation and maturation (83). While this activity is essential in the growth plate, excessive BMP activation in articular cartilage is detrimental. BMP, often acting in concert with RUNX2, promotes chondrocyte hypertrophy and induces expression of catabolic

enzymes such as MMP-13, thereby contributing to degenerative changes associated with osteoarthritis (85).

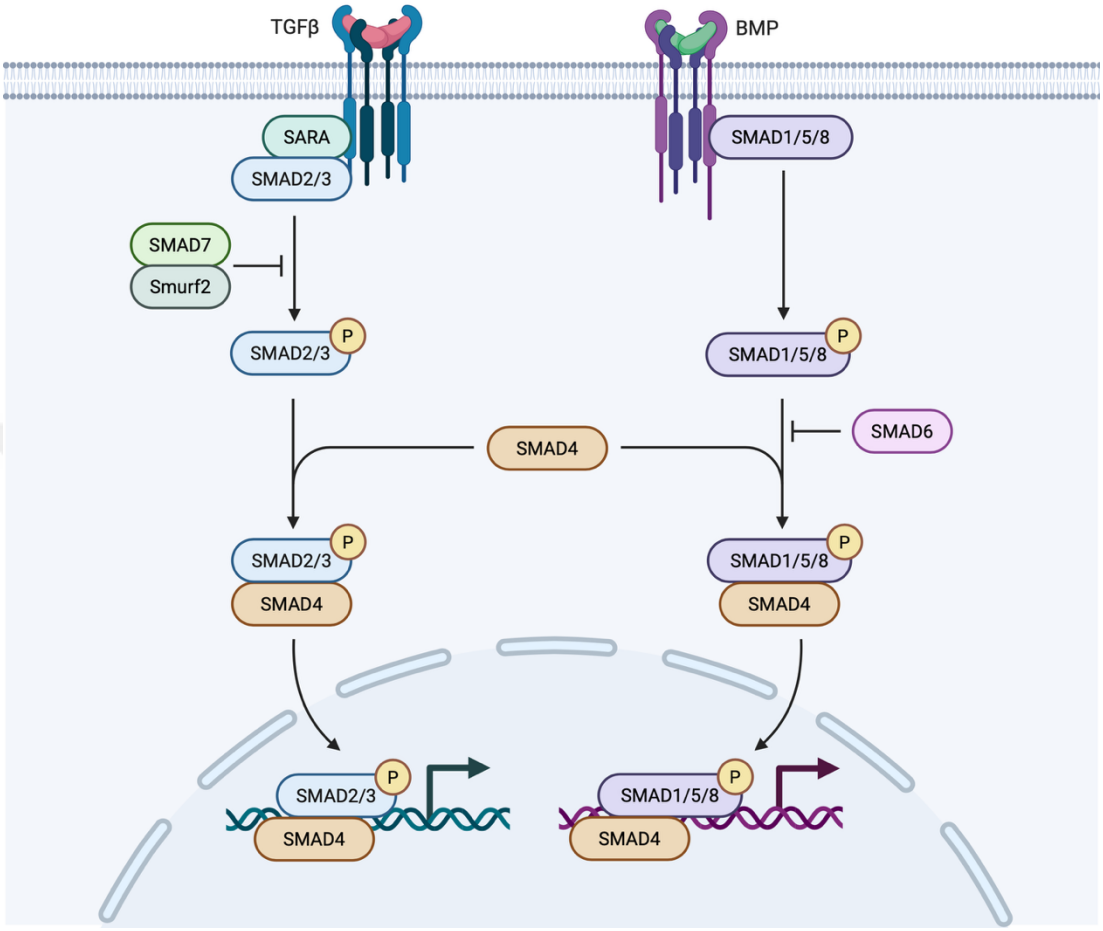

Figure 9. Overview of TGF-β and BMP signaling pathways and their shared SMAD-mediated transcriptional regulation. Created in BioRender.

The opposing effects of TGF-β and BMP are balanced by a complex regulatory network. At the extracellular level, antagonists such as Noggin and Gremlin bind BMP ligands and prevent receptor activation, thereby limiting pro-hypertrophic signaling (86). Intracellularly, negative feedback loops provide additional control. Inhibitory SMADs (SMAD6 and SMAD7), whose expression increases upon pathway activation, interfere with R-SMAD phosphorylation and nuclear translocation, effectively attenuating the signal. SMAD6 preferentially dampens BMP/SMAD1/5/9 activity, whereas SMAD7 more strongly suppresses TGF-β/SMAD2/3 signaling. Furthermore, E3 ubiquitin ligases such as Smurf1 regulate pathway duration by targeting receptors

or SMAD proteins for proteasomal degradation (83). Articular cartilage integrity depends on the balance between the TGF-β and BMP signaling. Loss of modulators such as WISP3, distrupts the equilibrium promoting cartilage degeneration and chondrocyte instability PPD.

2.5.3 Endoplasmic reticulum stress and the unfolded protein response

The endoplasmic reticulum (ER) is a critical organelle for the synthesis, modification, and folding of secretory and membrane proteins (87). Protein folding is a highly error-prone process, and the maintenance of a healthy proteome relies on complex quality control mechanisms operating within the ER. Various cellular stress factors, including hypoxia, nutrient deprivation, oxidative stress, and genetic variations, can lead to the accumulation of unfolded or misfolded proteins in the ER lumen. This condition, referred to as ER stress, activates the unfolded protein response (UPR), a signaling pathway that enables cells to sense stress and restore protein-folding capacity (88).

The UPR is a signaling network that reprograms transcription, mRNA translation, and protein modifications to alleviate the burden of unfolded proteins in the ER and to restore proteostasis (89). In mammalian cells, the UPR is mediated by three main ER transmembrane receptors: inositol-requiring enzyme 1 (IRE1α), PKR-like ER kinase (PERK), and Activating Transcription Factor 6 (ATF6) (88). ATF6 is a type II transmembrane protein that, in its inactive state, is bound to the molecular chaperone BiP in the ER lumen. Upon ER stress, binding immunoglobulin protein (BiP) dissociates to bind unfolded proteins, thereby releasing ATF6, which is subsequently transported to the Golgi apparatus. There, it undergoes sequential cleavage by site-1 protease (S1P) and site-2 protease (S2P), liberating its cytoplasmic N-terminal fragment, ATF6(N) (90). This active fragment then translocates to the nucleus, where it activates the transcription of UPR target genes involved in ER chaperone production, ER/Golgi biogenesis, and ER-associated degradation (ERAD) pathways (Figure 10). These pathways act in a coordinated manner to enhance the protein-folding capacity of the ER, limit the influx of newly synthesized proteins, and facilitate the clearance of accumulated proteins (91).

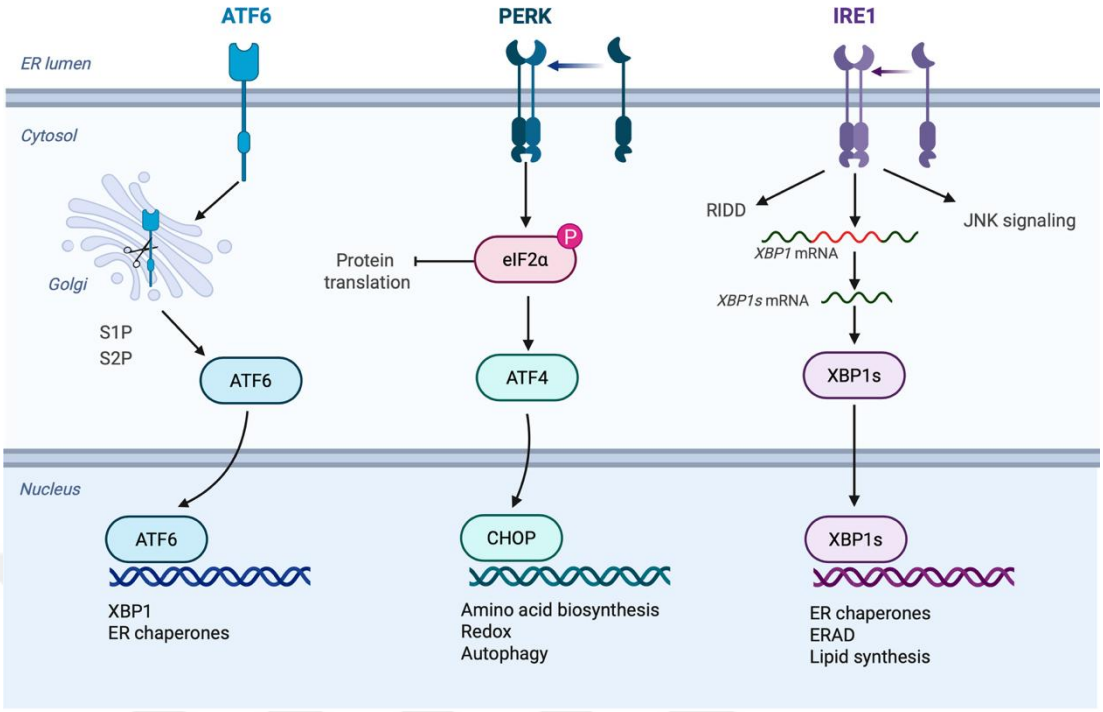

Figure 10. Unfolded protein response (UPR) signaling mediated by ATF6, PERK, and IRE1. Created in BioRender.

The UPR has two principal outcomes: adaptation or apoptosis. When ER stress is manageable, the UPR activates adaptive mechanisms. For example, the IRE1α pathway catalyzes the unconventional splicing of X-box binding protein 1 (XBP1) mRNA. This process generates the spliced form of XBP1 (XBP1s), a potent transcription factor that enhances the expression of genes involved in protein folding, ER-associated degradation (ERAD), and secretion (92). Therefore, the s/uXBP1 (spliced/unspliced XBP1) ratio is considered an indicator of the adaptive branch of the UPR.

However, when ER stress becomes chronic or severe, UPR signaling shifts from an adaptive response to a pro-apoptotic program. A central mediator of this process is DDIT3 (DNA Damage Inducible Transcript 3) also known as CHOP (C/EBP Homologous Protein, CHOP). DDIT3 is strongly induced by the PERK–eIF2α–ATF4 pathway and serves as a key regulator of ER stress–mediated apoptosis (88). It promotes cell death by suppressing the expression of anti-apoptotic BCL-2 family members, enhancing the transcription of pro-apoptotic BH3-only proteins such as

BCL2L11 (BIM), and inducing death receptor 5 (TNFRSF10B, DR5). Therefore, DDIT3 expression is considered a critical marker of the terminal or pro-apoptotic branch of the UPR (89).

Chondrocytes, as secretory cells, are particularly susceptible to ER stress, which plays a central role in the pathogenesis of various cartilage-related disorders such as chondrodysplasias and osteoarthritis (OA) (93). Indeed, protein-folding defects caused by variations in matrix proteins represent a key mechanism leading to ER stress in many genetic skeletal diseases. Similarly, ER stress is increasingly recognized as an important factor in the pathogenesis of degenerative cartilage diseases. In these pathological conditions, elevated ER stress markers have been reported in degenerated cartilage, triggering chondrocyte apoptosis and cartilage degradation.

2.5.4 Oxidative stress and reactive oxygen species (ROS) signaling

Mitochondria are central regulators of cellular metabolism and play a key role in energy production, signaling, and apoptosis (94). During ATP synthesis, they naturally generate reactive oxygen species (ROS) as byproducts (95). At physiological levels, ROS contribute to intracellular signaling and support processes such as chondrocyte differentiation (96). However, excessive ROS production disrupts cellular homeostasis and induces oxidative stress. In several pathological conditions, the accumulation of misfolded proteins triggers endoplasmic reticulum (ER) stress, imposing a high metabolic demand on mitochondria and impairing their function. Dysfunctional mitochondria exhibit increased electron leakage, leading to the overproduction of mitochondrial ROS (mtROS), such as superoxide (97).

Elevated mtROS levels are highly detrimental to chondrocytes and activate a cascade of catabolic processes. Initially, mtROS damage mitochondrial DNA, proteins, and membranes, initiating a self-perpetuating cycle in which damaged mitochondria generate additional ROS (94,98). This further compromises energy production and overall cellular function. Furthermore, excessive mtROS upregulate catabolic enzymes that degrade the cartilage matrix while suppressing the synthesis of key structural macromolecules, including proteoglycans. This imbalance weakens the

biomechanical resilience of cartilage and promotes progressive tissue breakdown. Chronic oxidative stress ultimately drives chondrocytes into premature senescence or apoptosis, reducing the tissue's capacity for repair and renewal (94).

Healthy cells possess mitochondrial quality control mechanisms to counteract such damage. The most critical of these is mitophagy, which selectively removes damaged mitochondria that produce excessive ROS. In addition, mitochondrial fission and fusion dynamics isolate dysfunctional regions and redistribute healthy components, thereby maintaining the overall integrity of the mitochondrial network. However, under conditions of chronic cellular stress caused by genetic defects, these quality control systems may become insufficient. As a result, persistent mitochondrial dysfunction and excessive ROS generation create a pathological environment that accelerates cartilage degeneration and contributes to disease progression (94).

2.6 Molecular Methods for Functional Genetics

Functional genetics focuses on understanding how genes and disease-associated variants influence cellular processes through controlled genetic manipulation. Common molecular approaches include variant-specific gene expression, gene silencing, and comparative analyses between wild-type and altered constructs. These strategies allow direct assessment of changes in protein abundance, intracellular distribution, cellular stress responses, signaling activity, and global gene expression patterns. When combined with quantitative molecular and cellular assays, such methods support the interpretation of genetic variation in human disease by linking specific genotypes to measurable cellular phenotypes.

Cell culture models offer a unique and practical opportunity to study human disease mechanisms, particularly when isolation and long-term maintenance of the relevant primary tissue are technically difficult. For disorders affecting cartilage, access to patient-derived material is limited, and experimental manipulation *in vivo* is often constrained by species-specific differences. Under these conditions, cell culture–based systems provide one of the most suitable platforms for functional investigation, as they allow direct examination of gene-specific effects in a controlled human cellular

environment (99). This advantage is especially relevant for proteins such as WISP3, for which clear functional counterparts are not uniformly conserved across experimental animal models (82,100). Cell culture platforms enable the use of targeted genetic strategies, including gene editing or overexpression-based approaches, to model disease-associated variants and assess their cellular effects. Moreover, as WISP3 is an extracellular matrix–associated protein with both intracellular and intercellular roles, its impact cannot be captured through a single experimental readout. A broader evaluation across multiple cellular processes is therefore required to understand how *CCN6* variants influence chondrocyte behavior and cartilage homeostasis. Within this framework, a set of key cellular and molecular techniques was applied to investigate these effects in detail.

2.6.1 Site directed mutagenesis

Site-directed mutagenesis (SDM) is one of the powerful and widely used techniques in molecular biology, enabling targeted alterations in nucleic acid sequences (101). It allows modifications ranging from single-nucleotide substitutions to larger insertions or deletions, making it an essential tool for exploring gene function at the molecular level. Through such precise editing, SDM has become indispensable for investigating the structural and functional properties of proteins and for understanding the molecular mechanisms underlying genetic variation (102).

Among the available strategies, PCR-based SDM is the most frequently adopted due to its reliability and efficiency. In this approach, the desired mutation is introduced through specially designed overlapping primers(103) These primers are typically 25–45 bases in length, with the mutation placed at the center and flanked by at least 10–15 bases of correct (wild-type) sequence on both sides (103). The GC content is usually maintained between 40–60%, and one or more G/C residues at the 3′ end are preferred to ensure stable binding. This design forces the incorporation of the intended nucleotide change during amplification, ensuring that the mutation is symmetrically incorporated into both DNA strands (104).

Using a high-fidelity DNA polymerase, the entire plasmid is amplified, generating newly synthesized DNA strands that carry the mutation. Following PCR, the reaction mixture is treated with DpnI, an enzyme that selectively digests the parental template DNA due to its bacterial methylation pattern. In contrast, the in vitro–synthesized, unmethylated mutant plasmid remains intact. This step enriches the proportion of mutant plasmids in the sample. The products are then directly transformed into competent *E. coli* cells, where endogenous repair mechanisms seal any remaining nicks, yielding high-quality mutant plasmids suitable for downstream applications (102).

For this study, site-directed mutagenesis was employed to generate defined *CCN6* variant constructs for overexpression-based functional analyses. This approach enabled precise introduction of disease-associated sequence changes into the WISP3 coding region, ensuring that each construct differed only at the intended nucleotide position. Such precision is particularly important in overexpression experiments, where accurate interpretation of cellular phenotypes requires minimizing unintended sequence alterations. Coupling SDM with transient overexpression in chondrocyte cell lines allowed individual *CCN6* variants to be modeled under controlled conditions and facilitated direct comparison of wild-type and variant WISP3 proteins within the same cellular background.

2.6.2 FoldX-Based stability analysis

Computational approaches are increasingly used to evaluate how amino acid substitutions influence protein stability and structure, particularly in studies addressing disease-associated variation. FoldX is a widely applied structure-based tool that estimates the energetic impact of single-residue changes using an empirical force field incorporating key physical interactions such as hydrogen bonding, electrostatics, van der Waals forces, solvation effects, and entropic contribution (105). By predicting changes in folding free energy, FoldX enables rapid *in silico* screening of multiple variants and provides mechanistic insight into whether a given substitution is likely to destabilize or stabilize the native protein structure (106). The primary output of FoldX

analyses is the mutational free energy change (ΔΔG), which reflects the difference in stability between the wild-type and the variant protein. Positive ΔΔG values are generally indicative of destabilizing effects, whereas negative values suggest increased structural stability (105). Importantly, ΔΔG represents a robust comparative measure that is less sensitive to environmental conditions such as temperature or pH than absolute folding free energy values, as many background energetic contributions cancel out when closely related structures are compared. In addition to global stability estimates (3,105), FoldX also provides residue-level energetic information, allowing evaluation of how specific interactions or local structural networks may be affected by sequence variation.

FoldX was applied to assess the potential structural impact of disease-associated missense variants in the WISP3 protein associated with PPD. As missense variants linked to this disorder may induce subtle yet functionally relevant alterations in protein stability, *in silico* evaluation provided an important initial framework for variant interpretation prior to experimental analyses. FoldX predictions were used to estimate whether individual *CCN6* variants were likely to compromise structural integrity, thereby informing hypotheses regarding altered protein behavior in chondrocyte-based cellular models. Integration of FoldX-based stability assessments with downstream functional assays enabled a more comprehensive evaluation of how variant-induced structural changes may contribute to disease-relevant cellular phenotypes.

2.6.3 Flow cytometry

Flow cytometry was selected in this study as a quantitative single-cell approach that enables rapid and sensitive assessment of cellular and organelle-specific parameters in live cells. By measuring light scattering and fluorescence signals emitted by targeted probes, this technique allows evaluation of cell size, internal complexity, and defined molecular features within heterogeneous cell populations (107). Its suitability for live-cell analysis makes flow cytometry particularly advantageous for investigating dynamic cellular processes that may be altered by genetic variation.

This capability is especially relevant for mitochondrial assessment, where flow cytometry is widely used to quantify mitochondrial mass and reactive oxygen species (ROS) production at the single-cell level. Given that WISP3 is not only an extracellular matrix–associated protein but has also been observed within intracellular compartments, *CCN6* variants may influence mitochondrial function and redox balance (14,108). To examine this aspect, mitochondria-targeted fluorescent probes were employed to distinguish changes in mitochondrial content from oxidative stress–related alterations. MitoTracker Green was used as an indicator of mitochondrial mass, while MitoSOX Red enabled selective detection of mitochondrial superoxide generation (109,110).

By allowing discrimination of viable cells with intact mitochondrial staining from background signals, flow cytometry provided a robust framework to assess variant-associated differences in mitochondrial homeostasis. These features collectively justified its use as a central analytical platform to explore how *CCN6* variants modulate mitochondrial physiology and cellular stress responses in the present work.

2.6.4 Omic technologies

Omic technologies comprise high-throughput approaches that enable global analysis of biological molecules, including nucleic acids, proteins, and metabolites. By allowing simultaneous assessment of thousands of molecular features, these platforms provide a systems-level view of cellular processes and support the investigation of complex biological networks. Advances in sequencing, mass spectrometry, and computational analysis have established multi-omics integration as a key strategy for elucidating disease mechanisms and identifying potential biomarkers (111).

2.6.4.1 Transcriptomics

The transcriptome encompasses the complete set of RNA molecules expressed by a cell under defined biological conditions and provides a direct readout of gene activity. Transcriptome-wide analysis using RNA sequencing has become the

preferred approach for gene expression profiling due to its sensitivity, broad dynamic range, and ability to detect both coding and non-coding transcripts without prior annotation (112).

Bulk RNA-Seq captures average expression patterns across cell populations and enables systematic comparison between experimental groups through standardized laboratory and computational workflows, followed by differential gene expression and functional enrichment analyses (114,115). Raw sequencing reads are first subjected to quality control, during which adapter sequences and low-quality bases are removed using standard preprocessing tools. Cleaned reads are then aligned to a reference genome or transcriptome with splicing-aware aligners capable of accurately mapping exon–intron junctions (115).

To enable reliable comparison across samples, read counts are normalized using methods that account for sequencing depth and transcript length, such as TPM or model-based approaches implemented in DESeq2 and edgeR (113,115,116). Differential gene expression analysis is subsequently performed to identify genes exhibiting statistically significant expression changes between experimental groups. Finally, functional enrichment analyses using Gene Ontology and KEGG are applied to interpret differentially expressed genes in terms of affected biological processes and signaling pathways, providing insight into transcriptional regulation at the genome-wide level (115).

Within the scope of this study, RNA-Seq was employed to investigate how *CCN6* variants associated with PPD influence global gene expression profiles in chondrocytes, the primary cell type affected in the disease. Given that the downstream molecular pathways regulated by *CCN6* remain incompletely characterized, transcriptome profiling provided an unbiased approach to capture variant-associated transcriptional alterations at the cellular level. By analyzing gene expression directly in chondrocyte-based disease models, this strategy enabled identification of biological processes and signaling pathways influenced by *CCN6* variants, thereby offering insight into cellular mechanisms contributing to disease pathogenesis.

2.6.4.2 Proteomics

The proteome represents the complete set of proteins expressed by a cell under defined biological conditions and reflects dynamic regulatory processes such as post-translational modifications and protein–protein interactions. Because proteins act as the primary functional mediators of cellular processes, proteomic analyses provide critical insight into mechanisms that cannot be inferred solely from genomic or transcriptomic data. Advances in mass spectrometry–based proteomics, particularly LC–MS/MS, have enabled large-scale, unbiased identification and quantification of proteins across complex biological samples, establishing proteomics as a core approach in molecular, cellular, and translational research (117). LC–MS/MS offers key advantages over traditional biochemical approaches, including a broad dynamic range for protein abundance, unbiased detection without prior knowledge of targets, and sufficient sensitivity to analyze complex biological samples (118). Ongoing advances in chromatography, such as nano-flow and micro-flow LC, mass analyzers including Orbitrap and TOF systems, and multiplexing strategies such as SILAC, TMT, and iTRAQ have further improved the depth, throughput, and reproducibility of proteome-wide analyses (119).

Beyond protein quantification, proteomics plays a central role in mapping protein–protein interactions (PPIs), which together form the cellular interactome. PPIs regulate essential biological processes ranging from transcriptional control to metabolic regulation and structural organization, and disruption of these networks is a common feature of many diseases, including cancer, neurodegeneration, and skeletal dysplasias (120,121). LC–MS/MS–based proteomic workflows integrate experimental and computational steps, encompassing peptide generation, mass spectrometric identification, quantitative analysis, and downstream interpretation through interactome reconstruction and functional enrichment using resources such as Gene Ontology and KEGG (117). These strategies allow researchers not only to quantify proteome-wide changes but also to contextualize them within regulatory networks and biological pathways.

Accordingly, LC–MS/MS–based proteomics was employed to characterize protein–protein interactions of both wild-type WISP3 and disease-associated *CCN6* variants, with particular emphasis on comparing nonsense and missense forms. This strategy enabled direct evaluation of how different variant classes reshape interaction networks and provided insight into the cellular roles of WISP3. Integration of interactome profiling with functional and transcriptomic analyses supported identification of molecular pathways influenced by *CCN6* variants and contributed to a more comprehensive understanding of WISP3-associated cellular mechanisms in PPD.

3 MATERIALS AND METHODS

3.1 Materials and Equipments

All reagents, kits, and consumables used in this study are listed in Table 2, with corresponding manufacturers and catalog numbers provided for reproducibility.

Table 2. List of reagents, kits, and chemicals used in the study with manufacturers and catalog numbers.

Chemicals	Manufacturer	Catalog Number
WISP3 cDNA ORF Clone, Human, N-HA tag	Sino Biological	HG15729-NY
DpnI	New England Biolabs	R0176
Q5 High-Fidelity DNA Polymerase	New England Biolabs	M0491
Deoxynucleotide (dNTP) Solution Mix	New England Biolabs	N0447S
Dimethyl sulfoxide	Merck	116743
Agarose	Sigma-Aldrich	A9539
DNA Stain	Serva	39803
DNA Ladder	Thermo Fisher Scientific	SM1303
DNA Loading Dye	Thermo Fisher Scientific	R1161
50x TAE Buffer	PanReac AppliChem	A4686
High Pure Plasmid Isolation Kit	Roche	11754777001 03143414001
LB Broth	BioShop Canada	LBL407
LB Agar	BioShop Canada	LBA408
Kanamycin	CalbioChem	420311
DPBS (with phenol red)	Thermo Fisher Scientific	14190144
DMEM (with phenol red)	Thermo Fisher Scientific	11965092
DMEM (without phenol red)	Thermo Fisher Scientific	31053028
0.25% Trpsin-EDTA	Thermo Fisher Scientific	25200056
Opti-MEM	Thermo Fisher Scientific	31985070
Penicillin-Streptomycin	Thermo Fisher Scientific	15140122
Goat Serum	Capricorn Scientific	GOA-1B
Fetal Bovine Serum (FBS)	Capricorn Scientific	FBS-16B
LipoFectMax 3000	ABP Biosiences	FP318

Table 2. List of reagents, kits, and chemicals used in the study with manufacturers and catalog numbers (Continued).

Chemicals	Manufacturer	Catalog Number
Paraformaldehyde	Thermo Fisher Scientific	169650010
Gelatin	Sigma-Aldrich	G2500
TRIzol Reagent	Thermo Fisher Scientific	15596026
Chloroform	Tekkim	TK.090260.01000
Ethanol	Isolab	920.026
2-propanol	Isolab	961.023
DEPC-treated Water	Thermo Fisher Scientific	R0601
Calcium chloride dihydrate	Merck	102382
Glycerol	Thermo Fisher Scientific	15514011
Bovine Serum Albumin (BSA)	Thermo Fisher Scientific	BSA-1U
Pierce BCA Protein Assay Kit	Thermo Fisher Scientific	23227
Radio-Immunoprecipitation Assay Buffer (RIPA)	Thermo Fisher Scientific	89901
Protease inhibitor cocktail	Boster Bio	AR1182
EDTA		
Ammonium persulphate (APS)	AFG Scientific	299828
N,N,N′,N′-Tetramethylethylenediamine (TEMED)	Sigma-Aldrich	T22500
Tris	BioShop Canada	TRS001.1
Glycine	neoFroxx	LC-10273.3
Sodium chloride	Sigma-Aldrich	S9888
Hydrochloric acid	Sigma-Aldrich	258148
Sodium hydroxide	Isolab	9691121000
Methanol	Isolab	920.026.2500
PVDF membrane (0.22 µM)	Thermo Fisher Scientific	88520
Acrylamide/Bis Solution, 37.5:1 (40 % w/v)	Serva	10681
Acrylamide/Bis Solution, 29:1 (30 % w/v)	Serva	10687
Sodium dodecyl sulfate	Serva	20760
Clarity Western ECL Substrate	Bio-Rad	1705061
β-Tubulin Rabbit monoclonal antibody	Abclonal	A12289
HA tag Polyclonal antibody	Proteintech	51064-2-AP

Table 2. List of reagents, kits, and chemicals used in the study with manufacturers and catalog numbers (Continued).

Chemicals	Manufacturer	Catalog Number
HRP-conjugated goat anti-rabbit IgG (H+L)	Abclonal	AS014
SensiFAST™ cDNA Synthesis Kit	Meridian Bioscience	BIO-65053
MTT Reagent	Invitrogen	M6494
Protein ladder	Genedirex	PM007-0500
DMSO	Sigma-Aldrich	116743
Human Type I Collagen	Stemcell	07005
Phosphate buffered saline tablets	Sigma-Aldrich	P4417
Hanks' Balanced Salt Solution (HBSS)	Capricorn	HBSS-1A
MitoSOX Red	ABP Biosciences	C259
MitoTracker Green	Cell Signaling Technologies	9074
Charged Microscope Slide	McKesson	177-1358W
Fluorescence Mounting Medium	Dako	S3023
HA Tag Monoclonal antibody	Proteintech	66006-2-Ig
TOM20 Polyclonal antibody	Proteintech	11802-1-AP
Anti-rabbit IgG (H+L), F(ab')2 Fragment (Alexa Fluor® 488 Conjugate)	Cell Signaling Technologies	4412
CoraLite594-conjugated Goat Anti-Mouse IgG(H+L)	Proteintech	SA00013-3
RNeasy Mini Kit	Qiagen	74104
Stranded Total RNA Prep, Ligation with Ribo-Zero Plus	Illumina	20040529
Pierce Direct Magnetic IP/Co-IP Kit	Thermo Fisher Scientific	88828
UPX Protein Extraction Kit	Abcam	ab270054
MilliporeSigma™ Microcon-30 kDa Centrifugal Filter Unit with Ultracel-30 Membrane	Merck	MRCFOR030
Trypsin (Mass Spectrometry Grade)	Thermo Fisher Scientific	90057
Pierce Quantitative Colorimetric Peptide Assay	Thermo Fisher Scientific	23275

The instruments used in this study are listed in Table 3.

Table 3. Instruments and equipment used in this study along with their manufacturers.

Instrument	**Brand**
Biosafety Cabinet Level II	Thermo Fisher Scientific
CO_2 Incubator	Thermo Fisher Scientific
Bacterial Shaker	Thermo Fisher Scientific
Spectrophotometer	Thermo Fisher Scientific
Refrigerated Benchtop Centrifuge	Beckman Coulter
- 20° Freezer	Kirsch
- 80° Freezer	Arctiko
Imaging System	Bio-Rad
Spectrophotometer	BMG Labtech
Orbital Shaker	Stuart
Minisipin	DLab
Micropipette	Thermo Fisher Scientific
Inverted microscope with camera	Zeiss
+4° Refrigerator	Kirsch
Thermal cycler	Bio-Rad
Mini centrifuge	Beckman Coulter
Vertical electrophoresis system	Bio-Rad
Wet transfer blotting system	Bio-Rad
Ultrapure water system	Millipore
Confocal microscope system	Zeiss
Fluorescence imaging system	Thermo Fisher Scientific
Flow Cytometry System	BD Biosciences
NovaSeq 6000 platform	Illumina
Tube rotator	Biosan
Water bath	Thermo Fisher Scientific
Mass spectrometer	Waters
Heat block	Thermo Fisher Scientific
Magnetic stirrer	Biosan
Microwave	Arçelik
Horizontal gel electrophoresis system	Bio-Rad
Power supply for electrophoresis	Bio-Rad

3.1.1 Buffers and Solutions

All buffers and solutions were prepared using double-distilled water (ddH_2O) and analytical-grade reagents unless otherwise specified.

Kanamycin (50 mg/mL): 0.5 g kanamycin was dissolved in 5 mL ddH_2O, sterilized through a 0.22 μm PVDF filter, and stored at −20 °C.

10× Running Buffer: 30 g Tris base, 144 g glycine, and 10 g SDS were dissolved in ddH_2O to a final volume of 1 L. The buffer was stored at room temperature.

10× Transfer Buffer: 30.3 g Tris base and 144.4 g glycine were dissolved in ddH_2O to a final volume of 1 L and stored at room temperature.

1× Transfer Buffer: Prepared by mixing 200 mL methanol, 700 mL ddH_2O, and 100 mL 10× transfer buffer. Stored at +4 °C.

10× TBS (Tris-Buffered Saline): 24.2 g Tris base and 80 g NaCl were dissolved in ddH_2O to a final volume of 1 L. The pH was adjusted to 7.6 with HCl and stored at room temperature.

1× TBS-T (Tris-Buffered Saline with 0.05% Tween-20): 100 mL of 10× TBS stock solution was diluted with 900 mL double-distilled water to obtain 1× working concentration. Subsequently, 0.5 mL of Tween-20 was added to achieve a final concentration of 0.05% (v/v). The solution was mixed thoroughly to ensure homogeneity and stored at room temperature.

Cell Lysis Buffer: 50 mM Tris-HCl (pH 7.4), 1% Triton X-100, 150 mM NaCl, and 5 mM EDTA were mixed in ddH_2O. Immediately before use, 1× protease inhibitor cocktail was added. The buffer was kept on ice during use.

10% Ammonium Persulfate (APS): 1 g APS was dissolved in 10 mL ddH_2O, filtered through a 0.22 μm filter, and stored at −20 °C.

1.5 M Tris-HCl (pH 8.8): 18.15 g Tris base was dissolved in 80 mL ddH_2O. The pH was adjusted to 8.8 using 6 N HCl and brought to a final volume of 100 mL with ddH_2O. Stored at +4 °C.

0.5 M Tris-HCl (pH 6.8): 6 g Tris base was dissolved in 80 mL ddH_2O, pH adjusted to 6.8 with 6 N HCl, and the final volume was brought to 100 mL with ddH_2O. Stored at +4 °C.

5× Laemmli Buffer: 0.125 M Tris-HCl (pH 6.8), 4% SDS, 5% β-mercaptoethanol, 20% glycerol, and 0.01% bromophenol blue were dissolved in 20 mL ddH_2O and stored at −20 °C.

0.5 M EDTA (pH 8.0): 18.61 g EDTA was dissolved in 80 mL ddH_2O with magnetic stirring. The pH was adjusted to 8.0 using NaOH pellets, and the volume was brought to 100 mL with ddH_2O. Sterilized by autoclaving.

10% SDS Solution: 10 g SDS was dissolved in 80 mL ddH_2O with gentle heating and stirring. The volume was adjusted to 100 mL with ddH_2O after complete dissolution. Stored at room temperature.

5% Blocking Solution: 2.5 g bovine serum albumin (BSA) was dissolved in 50 mL Tris-buffered saline (TBS; 20 mM Tris-HCl, 150 mM NaCl, pH 7.6) with gentle stirring until fully solubilized. The solution was aliquoted and stored at −20 °C.

LB Broth (1 L): 25 g of LB Broth powder was dissolved in 1 L of double-distilled water (ddH_2O) using a magnetic stirrer. The medium was autoclaved at 121 °C for 20 min and stored at room temperature.

LB Agar (1 L): 40 g of LB Agar powder was dissolved in 1 L ddH_2O with stirring and gently heated until completely dissolved. The solution was autoclaved at 121 °C for 20 min. After autoclaving, the medium was cooled to approximately 55 °C in a water bath. Immediately before solidification, kanamycin was added to a final concentration of 50 µg/mL from a sterile stock solution (50 mg/mL) and mixed gently to ensure uniform distribution. The antibiotic-supplemented medium was then poured into sterile Petri dishes under aseptic conditions and allowed to solidify at room temperature. Plates were stored at +4 °C

4 mg/ml Gelatin Solution: 200 mg gelatin powder was added to 50 mL of double-distilled water (ddH_2O) and heated to 65 °C on a magnetic stirrer until completely dissolved. The solution was filtered through a 0.22 µm membrane filter to ensure sterility and clarity. The prepared stock was stored at +4 °C.

0.1% (w/v) Gelatin Solution (1 mg/mL): 100 mg gelatin powder was added to 50 mL of double-distilled water (ddH_2O) and warmed to 60–65 °C on a magnetic stirrer until fully dissolved. The solution was cooled to room temperature and the volume was adjusted to 100 mL with ddH_2O. To ensure sterility and clarity, the solution was passed through a 0.22 µm membrane filter. The prepared solution was aliquoted and stored at +4 °C; warm gently before use to re-dissolve any precipitate.

5X Non-reducing Sample Buffer: 10 g SDS, 50 mL glycerol (100%), 0.025 g bromophenol blue, and 4.91 g Tris base were combined in double-distilled water (ddH_2O) to a final volume of 250 mL. The pH was adjusted to 6.8 with HCl. The buffer was mixed until fully dissolved and stored at room temperature.

Incubation Buffer (pH 7.5): 2.5 mL Triton X-100 (100%), 12.5 mL Tris-HCl (1 M, pH 7.5), 625 µL $CaCl_2$ (2 M), and 2.5 µL $ZnCl_2$ (0.1 M) were combined and mixed thoroughly. The final volume was adjusted to 250 mL with double-distilled water (ddH_2O). The buffer was stored at +4 °C.

Staining Solution: 40 mL methanol, 10 mL glacial acetic acid, and 50 mL double-distilled water (ddH_2O) were mixed thoroughly. Subsequently, 0.5 g Coomassie Brilliant Blue G-250 was added and stirred gently until completely dissolved. The prepared solution was stored at room temperature.

Destaining Solution: The destaining solution was prepared by mixing 100 mL of methanol, 25 mL of glacial acetic acid, and 125 mL of double-distilled water to yield final concentrations of 40% methanol and 10% acetic acid. Stored at room temperature.

Washing Buffer: 6.25 mL Triton X-100 (100%), 12.5 mL Tris-HCl (1 M, pH 7.5), 625 µL $CaCl_2$ (2 M), and 2.5 µL $ZnCl_2$ (0.1 M) were combined and mixed gently. The final volume was adjusted to 250 mL with double-distilled water (ddH_2O). The buffer was stored at room temperature.

4% Paraformaldehyte: 10 g paraformaldehyde powder was added to 200 mL of 1× PBS and heated to approximately 60 °C with gentle stirring until partially dissolved. The pH was gradually increased by adding 1 N NaOH dropwise until the solution became clear. After complete dissolution, the mixture was cooled to room temperature, filtered, and adjusted to a final volume of 250 mL with 1× PBS. The pH was fine-tuned to approximately 6.9 using dilute HCl. The solution was aliquoted and stored at +4 °C.

3.2 Methods

3.2.1 Studied genetic variants

Four previously reported *CCN6* variants located within exon 2 of the *CCN6* gene were selected for functional characterization. These include two nonsense variants (p.Cys52* and p.Tyr109*) and two missense variants (p.Gly83Glu and p.Cys114Trp), all mapped to the IGFBP domain of WISP3 (Figure 11). Genetic information for each variant, including their cDNA and protein-level changes, dbSNP identifiers, and CADD (Combined Annotation Dependent Depletion) scores, is summarized in Table 4. Allele frequency data were retrieved from the Genome Aggregation Database (gnomAD v2.1.1). Together, these variants provide a representative spectrum of truncating and missense alterations, enabling a comparative assessment of their molecular and cellular consequences.

Table 4. Summary of *CCN6* variants analyzed in this study

Location	Coding Sequence	Protein Sequence	dbSNP ID	CADD Score	Allele Frequency
Exon 2 NM_003880.4 IGFBP Domain	c.156C>A	p.Cys52*	rs121908901	36	3×10^{-5}
	c.248G>A	p.Gly83Glu	rs147337485	26.1	2.4×10^{-3}
	c.327C>A	p.Tyr109*	rs145747429	35	N/A
	c.342T>G	p.Cys114Trp	rs1776514016	23	N/A

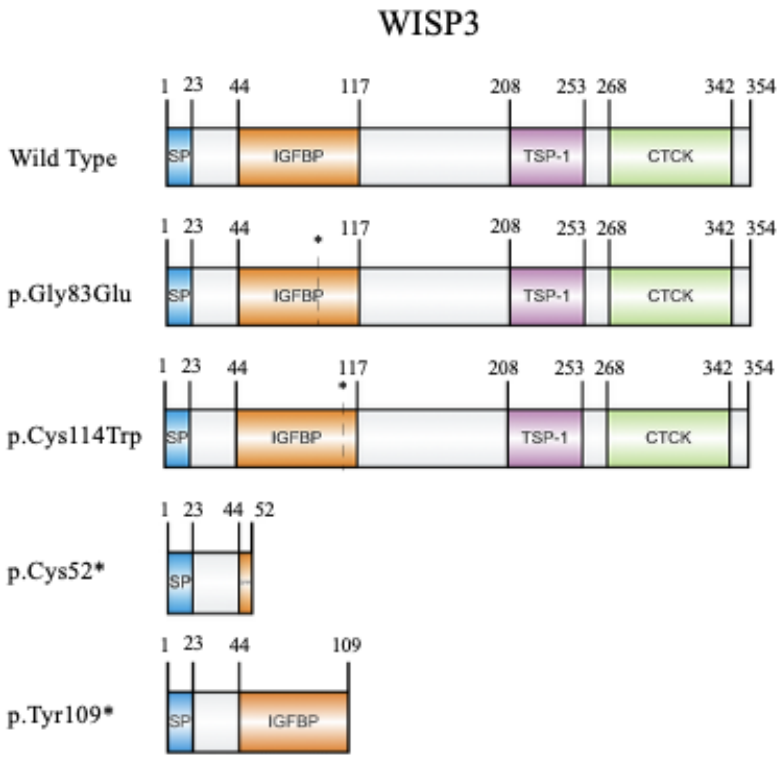

Figure 11. Domain structure of WISP3 and positions of analyzed WISP3 variants. Schematic representation of WISP3 showing its domain structure and the relative positions of four *CCN6* variants selected for functional characterization. WISP3 consists of an N-terminal signal peptide (SP), an insulin-like growth factor binding protein (IGFBP) domain, a thrombospondin type 1 repeat (TSP-1), and a C-terminal cystine knot (CTCK) domain. Missense variants p.Gly83Glu and p.Cys114Trp are located within the IGFBP domain and result in single amino acid substitutions, while nonsense variants p.Cys52* and p.Tyr109* introduce premature stop codons, leading to truncated proteins lacking one or more downstream domains. Amino acid positions are based on the UniProt entry O95389 (58).

3.2.2 Protein structure and stability

The three-dimensional model of human WISP3 (Cellular communication factor type 6 /WNT1-inducible signaling pathway protein 3, AF-O95389-F1-v4) predicted by AlphaFold was adopted as the reference structure for all *in silico* analyses. The model was examined to delineate domain boundaries and to identify high-confidence regions with elevated pLDDT scores corresponding to the variant positions analyzed in this study. All variants were located within the N-terminal insulin-like growth factor–binding (IGFBP) domain of WISP3; therefore, this domain was extracted from the full-length structure for detailed evaluation.

The isolated domain was structurally refined using the repairPDB command of the FoldX program, which corrects unfavorable torsion angles, van der Waals clashes, and overall energy strain (122). The repaired model was subsequently analyzed using the BuildModel function of FoldX to estimate the effects of each variant on protein stability. Variants yielding a calculated change in Gibbs free energy (ΔΔG, kcal/mol) greater than +0.5 kcal/mol were considered highly destabilizing. Structural visualization, editing, and image rendering of the WISP3 model were performed using VMD software (123).

3.2.3 Preparation of chemically competent *E. coli* cells

Chemically competent *Escherichia coli* (*E. coli)* cells were prepared using a modified calcium chloride method. A single colony of *E. coli* DH5α strain was inoculated into 5 mL of LB medium and incubated overnight at 37 °C with shaking at 250 rpm. The following morning, the overnight culture was diluted 1:100 into LB medium and incubated at 37 °C with shaking at 250 rpm until the optical density at 600 nm (OD_{600}) reached approximately 0.5. The culture was then transferred into 50 mL centrifuge tubes and incubated on ice for 20 min, ensuring that the cells were kept cold for all subsequent steps. Cells were harvested by centrifugation at 4500 rpm for 5 min at 4 °C, and the supernatant was carefully discarded. Each pellet was gently resuspended in 20 mL of ice-cold 100 mM $CaCl_2$ and incubated on ice for 1 h. Cells were again pelleted by centrifugation at 4500 rpm for 5 min at 4 °C, and the supernatant

was discarded. At the final step, pellet was resuspended in 2 mL of ice-cold 85 mM $CaCl_2$ containing 15% glycerol, aliquoted into pre-chilled sterile microcentrifuge tubes, and stored at −80 °C until use. All plasticware used during the procedure was pre-cooled, and all solutions and materials were maintained on ice to preserve cell competency.

3.2.4 Transformation and plasmid isolation

Transformation was performed using chemically competent *E. coli* DH5α cells. Aliquots of 50 µL competent cells were thawed on ice, and 100 ng of plasmid DNA was added to each tube. The mixture was incubated on ice for 30 min, followed by heat shock at 42 °C for 30 s. Cells were immediately returned to ice for 2 min to allow recovery. The transformation mixture was transferred to a 50 mL centrifuge tube, and LB medium was added to a final volume of 1 mL. Cultures were incubated at 37 °C with shaking at 250 rpm. Subsequently, 1.5 mL of the culture was transferred to a clear 1.5 mL microcentrifuge tube and centrifuged at 5000 rpm for 5 min. The supernatant was discarded, and the pellet was resuspended in 100 µL of LB medium. The suspension was spread onto LB agar plates containing 50 µg/mL kanamycin and incubated overnight at 37 °C. Positive colonies were selected for further analysis and grown in 5 mL of LB broth containing 50 µg/mL kanamycin at 37 °C for 10 h. After 10 h, overnight cultures were prepared by diluting the starter culture 1:500 into fresh LB broth with 50 µg/mL kanamycin. The following day, cells were harvested by centrifugation at 5000 ×g for 5 min, and the resulting pellets were either stored at −80 °C for later use or processed immediately for plasmid extraction using the Roche Genopure Plasmid Midi or Mini Kit, according to the manufacturer's instructions. Plasmid DNA concentration and purity were determined using a NanoDrop spectrophotometer, evaluating the A_{260}/A_{280} and A_{260}/A_{230} absorbance ratios to assess protein and solvent contamination, respectively. The integrity of the plasmids was verified by electrophoresis on 0.8% agarose gels, and preparations were stored at −20 °C until use.

3.2.5 Construction of *CCN6* variant expression vectors

3.2.5.1 Site directed mutagenesis

Site-directed mutagenesis (SDM) was performed to generate *CCN6* variant constructs for functional analyses. The plasmid template contained the full-length human WISP3 cDNA open reading frame (ORF) (NCBI Gene ID: 8838) with an N-terminal HA tag, a signal peptide sequence, and a bacterial kanamycin resistance cassette. The signal peptide directs the WISP3 protein, an extracellular matricellular protein, to the secretory pathway. The kanamycin resistance marker enabled bacterial selection during plasmid propagation, while the HA epitope was used for WISP3 detection in Western blotting and immunocytochemistry experiments. The plasmid map of the construct used in this study is shown in Figure 12.

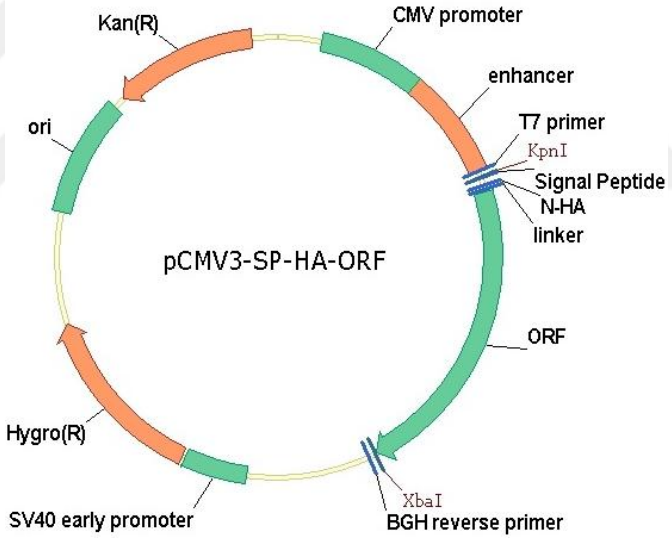

Figure 12. Plasmid map of pCMV3-SP-HA-ORF containing full lenght human WISP3 cDNA open reading frame (ORF).

Site-directed mutagenesis polymerase chain reactions (PCR) were performed using Q5 High-Fidelity DNA Polymerase according to the manufacturer's protocol. The DNA template was the methylated wild-type *CCN6* ORF plasmid isolated after transformation. Four *CCN6* variants were generated: c.156C>A, c.248G>A, c.327C>A, and c.342T>G. Variant-specific forward and reverse primers were

designed using the PrimerX online tool (http://www.bioinformatics.org/primerx). Primer design criteria included a length of 27–35 nucleotides and positioning of the intended nucleotide substitution at the center of the sequence. The SDM primers listed in Table 5 were synthesized with 5′ phosphorylation and were HPLC-purified (Oligomer, Türkiye).

Table 5. Primer Sequences Used for Site-Directed Mutagenesis

Nucleotide Change	Amino Acid Change	Primer Sequence	Primer Length	GC Content
c.156C>A	p.Cys52*	F : 5' GTTTTGTCACTGGCCCTG**A**AAATGCCCTCAGCAGAAG 3’ R : 5' CTTCTGCTGAGGGCATTT**T**CAGGGCCAGTGACAAAAC 3'	37	51.35 %
c.248G>A	p.Gly83Glu	F : 5' CTGTGCCAAGCAACCAG**A**GGAAATCTGCAATGAAG 3’ R : 5' CTTCATTGCAGATTTCC**T**CTGGTTGCTTGGCACAG 3'	35	48.57 %
c.327C>A	p.Tyr109*	F : 5' GACAGGCCTAGGTA**A**GAGACTGGAGTGTG 3’ R : 5' CACACTCCAGTCTC**T**TACCTAGGCCTGTC 3'	29	55.17 %
c.342T>G	p.Cys114Trp	F : 5' GAGACTGGAGTGTG**G**GCATACCTTGTAGC 3’ R : 5' GCTACAAGGTATGC**C**CACACTCCAGTCTC 3'	29	55.17 %

The composition of the SDM PCR reactions is summarized in Table 6. DMSO was included in the reaction mixture to lower the annealing temperature, thereby enhancing primer–template hybridization efficiency.

Table 6. Composition of the SDM PCR reaction

Component	Volumes for a 12.5 µL reaction	Final Concentration
Q5 5X Reaction Buffer	2.5 µL	1X
10 mM dNTP	0.25 µL	200 µM
10 µM Forward Primer	0.625 µL	0.5 µM
10 µM Reverse Primer	0.625 µL	0.5 µM
DNA Template (25 ng)	1 µL	20 ng
Q5 High-Fidelity DNA Polymerase	0.1 µL	0.02 U/µL
DMSO	0.625 µL	-
ddH_2O	6.775 µL	-

The thermal cycling parameters used for the SDM PCR reactions are shown in Table 7. Variant-specific annealing temperatures were optimized for each primer pair to ensure efficient amplification.

Table 7. Thermal cycling conditions for SDM PCR

PCR Steps	Temperature	Time (hh:mm:ss)
Initial Denaturation	98°C	00:00:30
Denaturation*	98°C	00:00:10
Annealing*	64°C (c.156C>A) 68°C (c.248G>A) 68°C (c.327C>A) 66°C (c.342T>G)	00:00:30
Extension*	72°C	00:03:00
Final Extension	72°C	00:02:00
Hold	4°C	∞

*Steps were repeated for 30 cycles.

3.2.5.2 DpnI digestion

Following PCR amplification, the PCR products were treated with DpnI endonuclease to selectively digest methylated parental plasmid DNA, leaving only the newly generated base-substituted plasmid DNA. The components of the DpnI digestion reaction are listed in Table 8.

Table 8. Volumes required for the DpnI digestion reaction

Component	Volumes for a 12.5 µL reaction	Final Concentration
10X rCutSmart Buffer	1.25 µL	1X
DpnI	0.25 µL	20 units
Plasmid DNA	-	1 µg
ddH_2O	Brought to a final volume of 12.5 µL	-

The DpnI digestion was carried out under the conditions recommended by the manufacturer, with the enzyme activation time optimized (124) (Table 9). Following enzyme inactivation, the samples were transformed into chemically competent *E. coli* DH5α stain.

Table 9. DpnI digestion incubation condition

Steps	Temperature	Time (hh:mm:ss)
DpnI activation	37°C	02:00:00
DpnI inactivation	80°C	00:20:00
Hold	4°C	∞

Following miniprep, PCR amplification was performed for Sanger sequencing (Macrogen, Europe) using the T7 promoter forward primer (5′–TAATACGACTCACTATAGGG–3′) and BGH terminator reverse primer (5′–TAGAAGGCACAGTCGAGG–3′) to verify the presence of the intended single nucleotide substitutions. The entire open reading frame (ORF) was sequenced to

confirm sequence integrity. The PCR reaction components were identical to those listed in Table 6, and the thermal cycling conditions are provided in Table 10.

Table 10. Thermal cycling conditions for Sanger Sequencing PCR

PCR Steps	Temperature	Time (hh:mm:ss)
Initial Denaturation	98°C	00:00:30
Denaturation*	98°C	00:00:10
Annealing*	56°C	00:00:30
Extension*	72°C	00:00:30
Final Extension	72°C	00:02:00
Hold	4°C	∞

*Steps were repeated for 30 cycles.

3.2.6 Cell culture

Human chondrocytes (402-05A, Cell Applications, Inc., USA) were maintained in high-glucose Dulbecco's Modified Eagle Medium (DMEM) supplemented with 10% fetal bovine serum (FBS) and 1% penicillin–streptomycin at 37 °C in a humidified incubator containing 5% CO_2. Cells were routinely passaged at 70–80% confluence using 0.25% Trypsin-EDTA.

For transfection studies, 2.5×10^5 cells were seeded into each well of a 12-well tissue culture plate in 1 ml of complete growth medium and allowed to attach overnight at 37 °C in a humidified incubator containing 5% CO_2. On the following day, cells were washed once with Dulbecco’s phosphate-buffered saline (DPBS) and transfected with 1 µg of plasmid DNA using LipofectMax 3000 Reagent (ABP Biosciences, USA).

For each sample, 3 µl of LipofectMax 3000 Reagent was diluted in 50 µl of Opti-MEM I Reduced Serum Medium and incubated at room temperature. Separately, 1 µg of plasmid DNA was diluted in 50 µl of Opti-MEM I, followed by the addition of 2 µl of Enhancer Reagent. The diluted DNA/Enhancer mixture was then combined with the diluted LipofectMax 3000 Reagent, mixed gently, briefly spun down, and incubated

for 15 minutes at room temperature to allow complex formation. Complexes were added to 500 µl of DMEM containing 10% FBS, then added dropwise to the cells, and the plate was gently rocked to ensure even distribution. After 4 hours of incubation, the transfection volume was brought to a final volume of 1 ml by adding 500 µl of fresh 10% FBS-DMEM (61). At 24 hours post-transfection, cells were washed with DPBS and the medium was replaced with 1 ml of fresh 10% FBS-DMEM. Unless otherwise specified, analyses were performed 48 hours after transfection.

3.2.7 Western blot

Following transfection, cells were detached by trypsinization and collected by centrifugation at 300 × *g* for 5 min. The resulting pellets were washed once with Dulbecco's phosphate-buffered saline (DPBS) and lysed in radioimmunoprecipitation assay (RIPA) buffer supplemented with 1% protease inhibitor cocktail (PIC). Cell lysis was performed on ice for 20 min with brief vortexing every 5 min to ensure efficient extraction. Lysates were cleared by centrifugation at 13,000 rpm for 15 min at 4 °C, and the supernatants containing total proteins were collected.

Protein concentrations were determined using the bicinchoninic acid (BCA) method in accordance with the manufacturer's instructions. Equal amounts of total protein (30 µg per sample) were resolved on 4–12–15% SDS–polyacrylamide gels and transferred onto 0.22 µm polyvinylidene difluoride (PVDF) membranes using the wet transfer method.

Membranes were blocked for 1 h at room temperature in Tris-buffered saline containing 0.05% Tween-20 (TBS-T) and 5% bovine serum albumin (BSA). Without additional washing, the membranes were immediately incubated overnight at 4 °C with primary antibodies diluted in the same blocking buffer: anti-HA (1:4000) and anti-β-Tubulin (1:2000). The next day, membranes were washed three times for 10 min each in 0.05% TBS-T and incubated for 1 h at room temperature with horseradish peroxidase (HRP)-conjugated anti-rabbit IgG(H+L) secondary antibody (1:5000).

After secondary incubation, membranes were washed three additional times for 10 min each in 0.05% TBS-T. Immunoreactive bands were visualized using an enhanced chemiluminescence (ECL) detection system according to the manufacturer's protocol**,** and images were acquired with the ChemiDoc imaging platform. The same membranes were subsequently reprobed for housekeeping protein detection to confirm equal loading. All Western blot analyses were carried out in three biological replicates.

3.2.8 Total RNA isolation and quantitative real-time PCR (qRT-PCR)

Forty-eight hours after transfection, cells were trypsinized and pelleted at 300 × *g* for 5 min. The pellets were washed once with Dulbecco's phosphate-buffered saline (DPBS), and total RNA was isolated using a modified TRIzol-based protocol. 500 µL of TRIzol reagent were added directly onto each cell pellet, and the lysate was pipetted up and down several times until complete homogenization was achieved. Samples were incubated for 5 min at room temperature to ensure complete dissociation of nucleoprotein complexes.

Phase separation was induced by adding 100 µL of ice-cold chloroform, followed by vigorous mixing for 10 seconds. After a 3 min incubation, the samples were centrifuged at 12,000 × *g* for 20 min at 4 °C. The clear upper aqueous phase was carefully transferred to a new tube, mixed with 250 µL of ice-cold isopropanol, and incubated for 20 min at room temperature on a rotator to ensure gentle and uniform mixing during RNA precipitation. The samples were centrifuged again at 12,000 × *g* for 15 min at 4 °C. The resulting RNA pellets were washed twice with 500 µL of ice-cold 75% ethanol prepared with RNase-free water, briefly vortexed, and centrifuged at 7,500 × g for 5 min at 4 °C after each wash. The supernatant was discarded, and the pellets were air-dried until no residual ethanol remained. RNA was dissolved in DEPC-treated water and incubated at 60 °C to ensure complete solubilization. RNA concentration and purity were assessed spectrophotometrically.

For complementary DNA (cDNA) synthesis, 500 ng of total RNA were reverse-transcribed using the SensiFAST cDNA Synthesis Kit (Meridian Bioscience)

according to the manufacturer's instructions. The reaction composition and reagent volumes are summarized in Table 11.

Table 11. Components used for complementary DNA (cDNA) synthesis

Component	Volumes for a 10 µL reaction	Final Concentration
cDNA	-	500 ng
5x TransAmp Buffer	2 µL	1X
Reverse Transcriptase	0.5 µL	-
DEPC-treated ddH_2O	Up to 10 µL	-

All cDNA samples obtained from reverse transcription were subsequently stored at −20 °C until use. The thermal cycling parameters applied for cDNA synthesis are summarized in Table 12.

Table 12. Thermal cycling conditions for cDNA synthesis

Steps	Temperature	Time (hh:mm:ss)
Primer annealing	25°C	00:10:00
Reverse transcription	42°C	00:15:00
Inactivation	85°C	00:05:00
Hold	4°C	∞

Real-time PCR reactions were performed on a LightCycler 96 System (Roche) using the SensiFAST SYBR No-ROX Kit (Meridian Bioscience). The primer sequences for each target gene are listed in Table 13.

Table 13. Gene names and primer sequences used for qPCR analysis

Gene	Forward and Reverse Primer (5′ → 3′)
CCN6	Fw: ACTGTAGCCTGGAACCATTACT Rv: TGGTCACCCTGTTAGATATTCCC
CHOP	Fw: GGAAACAGAGTGGTCATTCCC Rv: CTGCTTGAGCCGTTCATTCTC
sXBP1	Fw: GCTGAGTCCGCAGCAGGT Rw: CTGGGTCCAAGTTGTCCAGAAT
uXBP1	Fw: CAGACTACGTGCACCTCTGC Rv: CTGGGTCCAAGTTGTCCAGAAT
ACTB	Fw: CACCATTGGCAATGAGCGGTTC Rv: AGGTCTTTGCGGATGTCCACGT

All quantitative PCR reactions were prepared in a final volume of 10 µL. Each reaction contained cDNA template, gene-specific primers, and master mix components as summarized in Table 14. Reaction mixtures were briefly centrifuged at 100 × g for 1 min to ensure proper mixing and removal of air bubbles. All samples were run in triplicate to ensure reproducibility.

Table 14. Reaction composition and reagent volumes used for qPCR

Component	Volumes for a 10 µL reaction	Final Concentration
Template cDNA	2 µL	50 ng
Forward primer (10 µM)	0.4 µL	400 nM
Reverse primer (10 µM)	0.4 µL	400 nM
DEPC-treated ddH_2O	2.2 µL	-
2× SensiFAST SYBR Master Mix	5 µL	1X

Following reaction setup, amplification was carried out using the thermal profile described in Table 15**.** A melt-curve analysis step was included to verify the specificity of amplification products and to exclude primer-dimer formation.

Table 15. Thermal cycling conditions for qPCR

Steps	Temperature	Time (hh:mm:ss)	Cycle Number
Preincubation	95 °C	00:02:00	1
Denaturation	95 °C	00:00:05	40
Annealing	60 °C	00:00:10	
Extension	72 °C	00:00:15	
Melting Curve	95 °C	00:00:15	1
	60 °C	00:00:15	
	95 °C	00:00:15	
Cooling	4 °C	00:00:30	1
Hold	4 °C	∞	-

All quantification cycle (Cq) values were automatically determined by the LightCycler 96 software. The relative expression levels of target genes were calculated using the $2^{-\Delta\Delta Ct}$ method, with *ACTB* serving as the internal reference gene for normalization (125). Data from three independent biological replicates were analyzed, and each sample was measured in technical triplicate to ensure reliability.

3.2.9 MTT (3-(4,5-dimethylthiazol-2-yl)-2,5-diphenyl tetrazolium bromide) assay

Human chondrocytes (5×10^4 cells/well) were seeded into 96-well plates and incubated for 24 h prior to transfection. Forty-eight hours after transfection, the culture medium was gently removed, and cells were washed once with Dulbecco's Phosphate-Buffered Saline (DPBS). The MTT reagent was freshly prepared in PBS at a stock concentration of 5 mg/mL. For each well, a working solution was prepared by mixing 10 µL of the MTT stock solution with 90 µL of phenol red-free

DMEM supplemented with 10% fetal bovine serum (FBS), resulting in a final MTT concentration of 0.5 mg/mL. A total of 100 µL of this mixture was added to each well.

Plates were incubated for 4h at 37 °C in a 5% CO_2 humidified incubator under dark conditions to allow the formation of formazan crystals. Following incubation, the MTT-containing medium was carefully removed, and 100 µL of dimethyl sulfoxide (DMSO) was added to dissolve the crystals. The plates were then placed on an orbital shaker at low speed for 15 min in the dark to ensure complete solubilization.

Absorbance was measured at 570 nm using a SPECTROstar Nano microplate reader. Each condition was tested in eight biological replicates, and each sample was measured in duplicate. Raw absorbance values were used for comparative analysis among experimental groups.

3.2.10 Attachment assay

Forty-eight hours after transfection, cell adhesion was evaluated using collagen type I–coated 96-well plates. Human type I collagen was first dissolved in 0.01 N HCl to prepare a 3 mg/mL stock solution and subsequently diluted to a working concentration of 50 µg/mL in fresh 0.01 N HCl. Each well was coated with 50 µL of the collagen solution and incubated for 60 minutes at room temperature. After incubation, wells were washed twice with phosphate-buffered saline (PBS) and blocked with 1% (w/v) bovine serum albumin (BSA) in PBS for 60 minutes at 37 °C.

During the blocking step, transfected chondrocytes were detached by trypsinization, counted, and resuspended in serum-free, phenol red-free DMEM. Cells were seeded at a density of 1×10^4 cells per well in 50 µL of medium, with three biological replicates prepared for each condition. The final well volume was adjusted to 50 µL, and plates were incubated for 30 minutes at 37 °C in a 5% CO_2 humidified incubator to allow cell attachment.

After incubation, non-adherent cells were removed by gentle PBS washing twice. Adherent cells were fixed with 4% paraformaldehyde (PFA) for 15 minutes at room temperature, followed by one additional PBS wash. Wells were then stained with crystal violet for 20 minutes, rinsed thoroughly with tap water until excess dye was removed, and allowed to air dry for approximately 30 minutes.

Following drying, 50 µL of ddH_2O was added to each well for microscopic imaging of attached cells. After imaging, the wells were emptied, and 50 µL of 2% sodium dodecyl sulfate (SDS) was added to solubilize the bound dye. Plates were incubated for 30 minutes at room temperature, and absorbance was subsequently measured at 550 nm using a SPECTROstar Nano microplate reader (126).

3.2.11 Wound healing

Twenty-four hours after transfection, chondrocytes were seeded into 24-well plates at a density of 1×10^5 cells per well and incubated overnight to allow cell attachment. The following day, confluent monolayers were gently washed with DPBS, and the medium was replaced with phenol red-free DMEM supplemented with 10% FBS. Initial phase-contrast images were acquired at 0 hours using a Zeiss Axiocam microscope system.

A linear wound was then introduced across the cell monolayer using a sterile 1000 µL pipette tip. Detached cells were carefully removed by washing with DPBS, and fresh phenol red-free 10% FBS-DMEM was added. Plates were incubated for 24 hours at 37 °C in a 5% CO_2 humidified incubator to allow wound closure.

Images were captured at defined time points, and wound healing efficiency was quantified using ImageJ software (v1.54p, NIH, Bethesda, MD, USA) based on the percentage reduction in wound area at 24 hours relative to the initial wound width, calculated as described below (127).

$$\text{Wound closure (\%)} = 100 - [(\text{initial wound area} - 24\text{ h wound area}) / \text{initial wound area} \times 100]$$

3.2.12 Gelatin zymography

Gelatinase activity was evaluated by gelatin zymography using SDS–PAGE gels. Twenty-four hours after transfection, the medium was replaced with phenol red-free, serum-free DMEM. At 72 hours post-transfection, cell culture supernatants were collected and centrifuged at 500 × g for 3 minutes to remove cellular debris. Protein concentrations were determined by the BCA Protein Assay, and equal protein amounts (10 µg per sample) were used for electrophoresis.

In parallel, gelatin-containing polyacrylamide gels were prepared according to the compositions listed in Table 16. Prior to sample loading, wells were thoroughly rinsed using a syringe to eliminate any residual gelatin. Samples were diluted with deionized water to equal volumes, mixed with 5× non-reducing Laemmli loading buffer (0.01% bromophenol blue, 4% SDS, 125 mM Tris-HCl, pH 6.8, 20% glycerol), and incubated at room temperature for 20 minutes. Electrophoresis was carried out at 90 V on ice until the dye front reached the bottom of the gel.

Table 16. Composition of 4% stacking and 12.5% resolving polyacrylamide gels used for gelatin zymography

4% Stacking Gel		**12.5% Resolving Gel**	
Component	**Volume**	**Component**	**Volume**
0.5M Tris-HCl pH 6.8	1.25 ml	1.5M Tris-HCl pH 8.8	2 ml
30% Acrylamide	0.670 ml	30% Acrylamide	3.33 ml
ddH_2O	3.075 ml	ddH_2O	0.667 ml
10% SDS	50 µl	10% SDS	80 µl
10% APS	50 µl	10% APS	80 µl
TEMED	10 µl	TEMED	10 µl
-	-	4 mg/ml gelatin	2 ml

Following electrophoresis, gels were washed three times for 20 minutes each in washing buffer (2.5% Triton X-100, 50 mM Tris-HCl, pH 7.5, 5 µM $CaCl_2$, 1

μM $ZnCl_2$) to remove SDS and allow enzyme renaturation, followed by an additional 10-minute rinse with double-distilled water. Gels were then incubated overnight at 37 °C in incubation buffer (50 mM Tris-HCl, pH 7.5, 1% Triton X-100, 5 mM $CaCl_2$, and 1 μM $ZnCl_2$).

The next day, gels were stained for 1 hour at room temperature with Coomassie Brilliant Blue G-250 staining solution under gentle agitation and rinsed thoroughly with water to remove excess dye. Gels were subsequently treated with destaining solution (40% methanol, 10% glacial acetic acid) until clear lytic bands became visible (128). Band intensities were quantified using ImageJ software (v1.54p, NIH, Bethesda, MD, USA).

3.2.13 Flow cytometry

Forty-eight hours after transfection, the culture medium was removed, and cells were washed twice with pre-warmed DPBS. For mitochondrial staining, three parallel conditions were prepared: MitoSOX Red only, MitoTracker Green FM only, and combined co-staining. MitoSOX Red (5 mM stock) was used at a final concentration of 2.5 μM, and MitoTracker Green FM (50 μM stock) at 250 nM. Dyes were diluted in phenol red– and serum-free DMEM, and 250 μL of staining solution was added per well. Cells were incubated at 37 °C with 5% CO_2 for 25 min.

After incubation, cells were gently washed twice with HBSS, detached with 0.25% trypsin-EDTA for 5 min, and neutralized with DPBS at 37 °C. The cell suspension was centrifuged at 400 × g for 6 min, the supernatant discarded, and the pellet resuspended in HBSS for a second wash under the same conditions. Finally, cells were resuspended in 300 μL PBS for flow cytometric analysis.

A total of 20,000 events per sample were acquired using a BD FACSCanto II flow cytometer, detecting fluorescence in the FITC and PE channels for MitoTracker Green and MitoSOX Red, respectively. Compensation was performed using single-stained controls. Data were analyzed using FlowJo software (v10.10.0). The experiment was conducted in two biological replicates.

3.2.14 Confocal microscopy

3.2.14.1 Cell seeding and preparation of coverslips

Twenty-four hours after transfection, cells were seeded onto 12 mm glass coverslips placed in 24-well plates. Coverslips were sterilized by immersion in 70% ethanol twice for 5 min, followed by one rinse in sterile water, and UV exposure for 15 min. Each well was coated with 400 µL of 0.1% (w/v) gelatin and incubated at 37 °C for 30 min. During this period, cells were detached with 0.25% trypsin-EDTA, counted, and seeded at a density of 60,000 cells per well in DMEM supplemented with 10% FBS. Cells were allowed to attach and recover overnight in a humidified incubator at 37 °C with 5% CO_2.

3.2.14.2 Mitochondrial staining (MitoSOX and MitoTracker imaging)

The following day, the medium was aspirated, and cells were washed twice with pre-warmed HBSS. For mitochondrial staining, cells were incubated with 2.5 µM MitoSOX Red and 250 nM MitoTracker Green FM, diluted in phenol red– and serum-free DMEM to a final volume of 250 µL per well. Incubation was carried out at 37 °C with 5% CO_2 for 25 min. After staining, cells were gently washed twice with warm HBSS and immediately mounted for confocal imaging. Images were acquired the same day under identical microscope settings. Quantitative analyses were based on ≥25 cells per replicate across three independent experiments.

3.2.14.3 WISP3 and TOM20 co-localization analysis

For immunofluorescence imaging of WISP3 and the mitochondrial marker TOM20, cells were fixed directly in 24-well plates with 4% paraformaldehyde (PFA) for 20 min at 37 °C and then washed three times with DPBS on an orbital shaker for 5 min each. Cells were permeabilized with 0.1% Triton X-100 in PBS for 30 min at room temperature, followed by three DPBS washes on an orbital shaker for 5 min each. Blocking was performed with 5% normal goat serum in PBS for 30 min at room temperature.

After blocking, coverslips were carefully transferred onto Parafilm placed at the bottom of a 35 mm Petri dish with the cell surface facing upward, allowing antibody droplets to maintain a domed shape during incubation. Primary antibodies anti-HA (1:1200) and anti-TOM20 (1:400) were diluted in the blocking solution to a total volume of 80 µL per coverslip, and incubation was performed overnight at +4 °C. To prevent drying, a moistened Kimwipe was placed inside the Petri dish, and the lid was covered with a paper towel moistened with water.

The next day, coverslips were washed three times with PBST (PBS containing 0.05% Tween-20) on an orbital shaker for 5 min each. Secondary antibodies (Alexa Fluor 488– and CoraLite 594–conjugated) were applied at dilutions of 1:1000 and 1:400, respectively, and incubated for 2 h at room temperature in the dark. Nuclei were counterstained with 300 nM DAPI, and coverslips were subsequently mounted onto glass slides for imaging.

Confocal images were obtained using a Zeiss LSM 700 microscope. Maximum intensity projections of z-stacks were analyzed in ImageJ (v1.54p, NIH, USA) using the BIOP JaCoP plugin (v1.2.0) (129). Co-localization between HA-tagged WISP3 and TOM20 was quantified by calculating Pearson correlation and Manders' M2 coefficients. Each channel was thresholded using the Otsu algorithm prior to analysis. All images were acquired under identical microscope settings, and quantification was performed on ≥25 cells per replicate across three independent experiments.

3.2.15 RNA-Seq quantification, differential gene expression, and enrichment analysis

Total RNA was isolated from *CCN6*-overexpressing (OE) cells and from cells expressing the pathogenic variants p.Cys52* and p.Cys114Trp using the RNeasy Mini Kit according to the manufacturer's instructions. Each condition comprised two biological replicates. Ribosomal RNA–depleted, strand-specific libraries were prepared with the Illumina Stranded Total RNA Prep, Ligation with Ribo-Zero Plus

Kit, and sequencing was performed on an Illumina NovaSeq 6000 platform (2 × 100 bp paired-end mode), generating approximately 25 million read pairs per sample.

3.2.15.1 Bioinformatic and statistical analyses

Raw reads were subjected to quality assessment to examine base-call accuracy, per-cycle GC distribution, and adapter or low-complexity contamination. When necessary, residual adapters and low-quality trailing bases were trimmed prior to alignment. Splice-aware alignments were generated against the *Homo sapiens* reference genome (GRCh38) using HISAT2 (v2.2.1) under default parameters. Gene models from the GENCODE v48 comprehensive annotation set was used to guide read mapping and quantification. Gene-level counts were obtained with featureCounts (v2.0.8) in paired-end mode, restricting quantification to primary alignments and applying the strandness consistent with library chemistry.

For normalization and exploratory analyses, library sizes were scaled using the trimmed mean of M-values (TMM) method, and counts were transformed to $\log_2$-counts per million ($\log_2$-CPM) with a small prior count to stabilize variance across genes. The resulting matrix was employed for principal component analysis (PCA) and pairwise Pearson correlation analyses in R (stats package v4.2.2) to assess replicate concordance and overall sample relationships.

Genes were retained for statistical testing if they exhibited ≥1 count per million (≈10 reads) in at least two samples of the smallest genotype group and were detected in ≥70 % of samples in each condition. Differential gene expression was evaluated using the edgeR quasi-likelihood (QL) framework (v4.0.16). A design matrix encoding genotype/condition was fitted; common and trended dispersions were estimated, and tagwise QL dispersions were computed to model gene-specific variability across replicates. Quasi-likelihood F-tests were used to contrast each variant group (p.Cys52*, p.Cys114Trp) independently against the wild-type OE reference condition. Resulting *p*-values were adjusted for multiple testing using

the Benjamini–Hochberg procedure to control the false discovery rate (FDR), and genes were considered significant at FDR < 0.05.

Significant genes and genome-wide ranked statistics were subjected to functional enrichment analysis using the clusterProfiler package's *fgsea* module (v4.6.2) against the MSigDB Gene Ontology Biological Process collections (v2025.1.Hs). Enrichment was performed in a pre-ranked manner using signed statistics derived from the differential expression tests, applying FDR correction to pathway-level results. To capture ER-stress–related biology, expression profiles of predefined ER-associated genes (both up- and down-regulated sets) were Z-score normalized by gene across all six samples and visualized with pheatmap (v1.0.12), enabling comparison of coordinated transcriptional trends between conditions.

All data visualization was carried out in R (v4.2.2) using ggplot2 (v3.5.2) and clusterProfiler plotting utilities. Volcano plots ($\log_2$ fold-change vs $-\log_{10}$ adjusted *p*-value) summarized gene-level differences, dot plots highlighted top enriched biological processes with gene-ratio and FDR annotations, and upset plots illustrated intersections among significant gene sets across variant contrasts. Default parameters were used unless otherwise specified. The complete computational workflow, including alignment, quantification, filtering, modeling, and enrichment, was executed under reproducible conditions, and the corresponding code and parameter files are available upon request.

3.2.16 Protein interaction profiling by Co-Immunoprecipitation and LC–MS/MS

3.2.16.1 Co-Immunoprecipitation (Co-IP) procedure

Human chondrocytes were transfected with plasmids encoding HA-tagged wild-type WISP3 (OE), p.Tyr109*, or p.Cys114Trp variants, each represented by two biological replicates. Forty-eight hours after transfection, cells were trypsinized, collected, and washed once with DPBS. Approximately 3×10^6 cells were used per

condition. The cell pellet was lysed using Pierce IP Lysis/Wash Buffer, as described in the Western blot protocol, and incubated on ice to ensure complete cell disruption. Lysates were clarified by centrifugation, and protein concentration was determined.

For immunoprecipitation, 5 µg of mouse monoclonal anti-HA antibody was added to 1 mg of total protein lysate, and the antibody was covalently coupled to magnetic beads via NHS-activated chemistry using the Pierce Direct Magnetic IP/Co-IP Kit (Thermo Fisher Scientific, Waltham, MA, USA). The mixture was incubated at room temperature under gentle rotation to allow antigen–antibody binding. Subsequent washing, magnetic separation, and elution steps were performed according to the manufacturer's instructions using the supplied buffers. Elution was carried out with the provided elution buffer supplemented with 10% neutralization buffer, and eluates were collected for downstream LC–MS/MS analysis.

3.2.16.2 Peptide preparation and LC–MS/MS analysis

Protein extraction was carried out by homogenizing each sample in the buffer provided with the UPX Protein Extraction Kit, following the supplier's protocol. The resulting lysates were heated to 95 °C for 5 min to denature all proteins completely. Each homogenate was subsequently loaded onto 30 kDa molecular weight cut-off FASP filters. To promote efficient unfolding, the membranes were rinsed with 8 M urea before further treatment.

For the alkylation step, 400 mM iodoacetamide (IAA) was added directly to the filters, and the membranes were incubated in the dark at room temperature for 20 min. Excess reagents were eliminated by washing the filters three times with 8 M urea and then three additional times with 50 mM ammonium bicarbonate (ABC).

Protein digestion was performed on the filters using 1 µg of sequencing-grade trypsin, followed by overnight incubation at 37 °C. After enzymatic cleavage, peptides were eluted by sequential rinsing—two times with 50 mM ABC and once with 500 mM sodium chloride (NaCl). The combined eluates were collected, and peptide

concentrations were determined using the Pierce Quantitative Colorimetric Peptide Assay according to the manufacturer's instructions.

Peptide mixtures were analyzed on an ACQUITY UPLC M-Class chromatography system coupled to a Xevo G2-XS Q-Tof mass spectrometer (Waters Corporation, Milford, MA, USA). Samples were first concentrated on a Symmetry C18 trap column (5 µm, 180 µm i.d. × 20 mm) at 3 µL/min for 2 min using 5% of mobile phase B (acetonitrile + 0.1% formic acid). Analytical separation was achieved on a CSH C18 column (1.7 µm, 75 µm i.d. × 250 mm) maintained at 45 °C, operated at a flow rate of 0.3 µL/min. The mobile phase gradient started at 5% B, increased linearly to 45% over 90 min, reached 85% between 90–91 min, held until 99 min, and returned to 5% B for re-equilibration until 120 min. Mobile phase A consisted of water with 0.1% formic acid.

Mass spectrometric acquisition was conducted in positive electrospray ionization (ESI) mode under data-independent acquisition (DIA) and sensitivity settings. Spectra were recorded over an m/z range of 50–2000 with 0.5 s scan time and a ramped collision energy of 14–40 V for high-energy events. The cone voltage was calibrated according to the manufacturer's specifications. Real-time mass correction was performed via Lockspray using [Glu1]-Fibrinopeptide B (m/z 785.8426) as the reference compound, acquired every 60 s and averaged across three scans within ±0.5 Da.

Raw data were analyzed in Progenesis QI for Proteomics (v4.1) using the reviewed UniProtKB database (release 18 June 2025, version 2025_03). Minimum intensity thresholds were 150 counts for low-energy and 50 counts for elevated-energy signals. Peptide and protein identifications required at least three fragment ion matches per peptide, seven per protein, and one unique peptide per protein. One missed cleavage site was permitted. Carbamidomethylation of cysteine was defined as a fixed modification, whereas oxidation of methionine and deamidation of asparagine/glutamine were treated as variable modifications.

3.2.16.3 Bioinformatic processing and quantitative analysis

Label-free quantitative (LFQ) proteomics datasets generated from two independent biological replicates per condition—wild-type WISP3/*CCN6* overexpression (WT/OE) and two pathogenic variants (p.Tyr109* and p.Cys114Trp)—were processed in R using DEP v1.28.0, which wraps the limma empirical-Bayes framework for differential analysis. Raw protein intensity tables were imported with associated sample annotations (condition and replicate). Intensities were first cleaned by removing contaminants/decoys and proteins lacking quantitative values in all samples. To stabilize variance and approximate normality, intensities were offset with a small pseudocount where required and transformed to log2 scale. Between-sample systematic effects were mitigated by mean-centering normalization across samples (global centering of $\log_2$ intensities per run), after which replicate concordance was examined by principal component analysis and pairwise correlations on the normalized matrix.

To ensure comparability across conditions, proteins entirely missing in any one condition (i.e., absent in all replicates of that condition) were excluded from hypothesis testing. Remaining missing values—assumed to arise predominantly from low-abundance, left-censored signals—were imputed using DEP's MinProb routine, which stochastically samples from a left-shifted Gaussian distribution relative to the observed intensity distribution to model values below the detection threshold (DEP defaults were used unless otherwise noted). Post-imputation distributions were inspected to confirm the expected left shift and to avoid artificial compression of fold changes.

Differential protein abundance was assessed with limma linear models, specifying a design matrix with condition as a fixed effect and treating WT/OE as the reference. Empirical-Bayes moderation of standard errors was applied to improve variance estimation given the small replicate number. Two primary contrasts were tested independently: p.Tyr109* vs WT/OE and p.Cys114Trp vs WT/OE. To maximize sensitivity in discovery analyses, no a priori fold-change threshold was imposed at the testing stage.

Visualization and reporting were performed in ggplot2 (v3.5.2). Volcano plots (log2 fold change vs −log10 adjusted P-value) summarized contrast-specific results; significant proteins were annotated to highlight effect sizes and statistical support. Additional QC visualizations included sample-level intensity boxplots before/after normalization and replicate correlation heatmaps to document data quality.

Protein interaction networks were constructed from interactor lists identified by co-immunoprecipitation mass spectrometry performed on WT/OE WISP3 and each variant (p.Tyr109*, p.Cys114Trp). Interactors unique to each condition and those shared across any combination were compiled into an edge list with the "bait" node (WT/OE, p.Tyr109*, or p.Cys114Trp) connected to its prey proteins. Networks were assembled with tidygraph v1.3.1 and rendered using ggraph v2.2.1. Edge colors encoded overlap class (condition-specific vs shared between two or all three conditions). Protein nodes were annotated with curated functional categories (e.g., ER protein processing, cytoskeleton organization, ubiquitin–proteasome), and multi-category membership was visualized as node-embedded pie charts via ggforce v0.5.0. Node size reflected degree (connectivity), and layouts were computed with the Fruchterman–Reingold force-directed algorithm to balance readability and preservation of network topology. To improve legibility, text labels were placed with repulsion, and variant/bait nodes were emphasized as labeled tiles.

All analyses were run in R v4.2.2. Package versions are reported above to facilitate reproducibility; default settings were applied unless explicitly specified. Complete code and parameter files (import, filtering, normalization, imputation, modeling, multiple-testing correction, and graph construction) are available upon request to enable independent replication.

3.2.17 Statistical analysis

Group comparisons were assessed using one-way analysis of variance (ANOVA). When homogeneity of variances was met, standard fixed-effects ANOVA was applied; otherwise, Welch-corrected ANOVA was used. A significance level of $\alpha = 0.05$ was

adopted. When the omnibus test indicated a significant effect, Tukey's honestly significant difference (HSD) post hoc test was performed to obtain multiplicity-adjusted p-values with 95% confidence. For two-group comparisons where applicable, two-tailed Student's t-tests were conducted under equal- or unequal-variance assumptions as appropriate.

Outlier detection was performed using the interquartile range (IQR) method, excluding values below Q1 − 1.5×IQR or above Q3 + 1.5×IQR. All statistical analyses were carried out in Python 3.12 using NumPy (v1.26) and SciPy (v1.13) libraries (130). Relative transcript abundance was determined using the $2^{-\Delta\Delta Ct}$ method, and fold-change values representing relative *CCN6* transcript levels are presented with corresponding 95% confidence intervals (CI).

ANOVA was performed on fold-change data, and significant group differences were further evaluated using Tukey's HSD test. Data visualization was performed in Matplotlib (v3.9) and Seaborn (v0.14) as box-and-whisker or bar plots with jittered individual data points. Statistical significance was indicated as follows: $p < 0.05$ (*), $p < 0.01$ (**), $p < 0.001$ (***), $p < 0.0001$ (****), and "ns" for non-significant differences ($p \geq 0.05$).

4 RESULTS

4.1 Structural Stability Assessment of WISP3 IGFBP Domain Alterations

This study aimed to assess the functional impact of selected *CCN6* variants that are either the most frequently detected in the Turkish population or have not yet been functionally examined with regard to the pathogenesis of Progressive Pseudorheumatoid Dysplasia (PPD). Among these, c.248G>A (p.Gly83Glu), c.327C>A (p.Tyr109*), and c.342T>G (p.Cys114Trp) have not been functionally characterized previously, whereas c.156C>A (p.Cys52*) has been reported before, yet only limited functional data are available. To gain molecular insight into how these single-nucleotide substitutions might alter WISP3 conformation and thermodynamic stability, in-silico structural modeling and energy-based analyses were conducted.

The AlphaFold-predicted WISP3 structure (AF-O95389-F1-v4) served as the reference model for computational assessment (Figure 13). This model consists of three conserved domains: the insulin-like growth factor binding protein (IGFBP) N-terminal domain, the thrombospondin type-1 repeat (TSP-1), and the C-terminal cystine knot (CTCK). Among these, the IGFBP domain exhibited the highest confidence based on predicted local distance difference test (pLDDT) scores, providing a reliable structural basis for the subsequent energy estimation.

Because the nonsense variants p.Cys52* and p.Tyr109* generate premature stop codons that truncate the polypeptide chain making full-length folding and stability calculations unreliable, only the two missense variants, p.Gly83Glu and p.Cys114Trp, were subjected to FoldX-based stability prediction. Both substitutions reside within the IGFBP N-terminal domain (residues 44–117, UniProt O95389), which was extracted from the complete AlphaFold model for energy analysis (Figure 13).

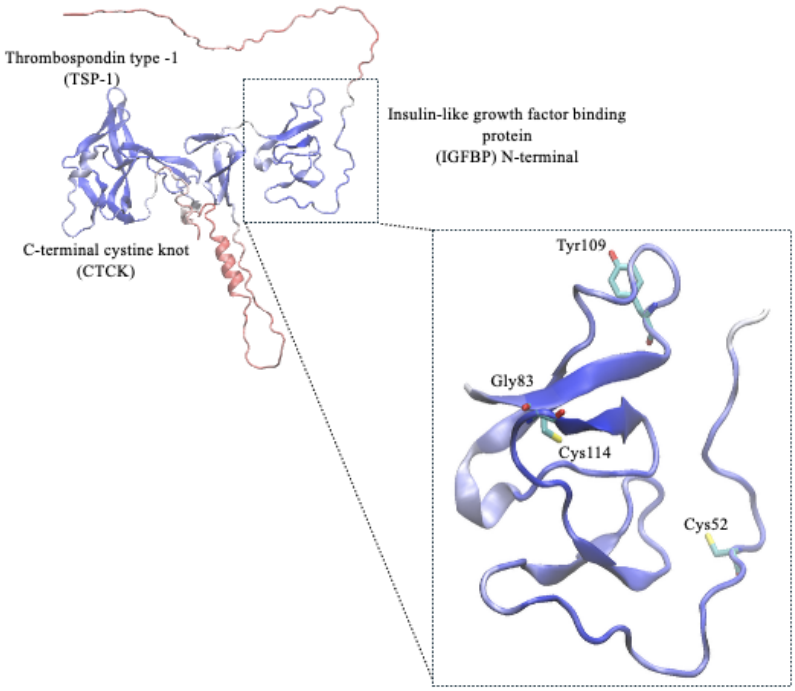

Figure 13. WISP3 domain structure and variant positions within the IGFBP N-terminal region. Schematic representation of the WISP3 AlphaFold model (AF-O95389-F1-v4) highlighting the IGFBP, TSP-1, and CTCK domains. The IGFBP N-terminal domain, containing the analyzed *CCN6* variants, is enlarged to show the positions of key residues affected by p.Gly83Glu and p.Cys114Trp substitutions.

Predicted free-energy change (ΔΔG) analysis revealed distinct outcomes for the two missense variants (Table 17). In this analysis, higher ΔΔG values correspond to reduced protein stability. The p.Gly83Glu substitution caused a mild structural alterations, whereas p.Cys114Trp displayed a pronounced destabilizing effect. This strong destabilization is consistent with the predicted disruption of the disulfide bridge between Cys114 and Cys92, a linkage essential for maintaining IGFBP domain integrity. Collectively, these results indicate that while p.Gly83Glu exerts a minor influence on local folding, p.Cys114Trp substantially compromises WISP3 stability, potentially affecting its biological function and contributing to disease mechanisms implicated in PPD pathogenesis.

Table 17. FoldX-based calculation of free energy change (ΔΔG).

Variant	ΔΔG Prediction for Protein Stability (kcal/mol)
p.Gly83Glu	+2.73
p.Cys114Trp	+43.33

4.2 Sequence Validation of *CCN6* Expression Constructs

Four *CCN6* variants — c.156C>A (p.Cys52*), c.248G>A (p.Gly83Glu), c.327C>A (p.Tyr109*), and c.342T>G (p.Cys114Trp) — were generated through site-directed mutagenesis using Q5 High-Fidelity DNA Polymerase. The mutagenesis template consisted of a full-length, HA-tagged *WISP3* expression plasmid of 7082 bp, containing the complete *CCN6* open reading frame (ORF).

Following amplification, methylated parental DNA was selectively removed by DpnI digestion, and the resulting plasmids were transformed into *E. coli* DH5α cells. Isolated plasmids were subsequently validated by Sanger sequencing. For this purpose, a ~1245 bp region spanning the entire *CCN6* ORF, including all four variant loci, was amplified to verify both the presence of the desired substitutions and the absence of any additional sequence alterations.

Sequence chromatograms were analyzed using CodonCode Aligner, with each variant sequence aligned against its corresponding wild-type reference plasmid. Clean single-base substitutions were observed at the targeted positions, with no background noise or secondary peaks in adjacent regions. Full-length ORF alignments confirmed that only the intended nucleotide change was introduced, and no non-specific modifications were present elsewhere within the coding sequence (Figure 14).

Together, these results confirmed the accuracy of the site-directed mutagenesis workflow and established that all variant plasmids were precisely generated and sequence-verified, ensuring their suitability for downstream expression and functional analyses.

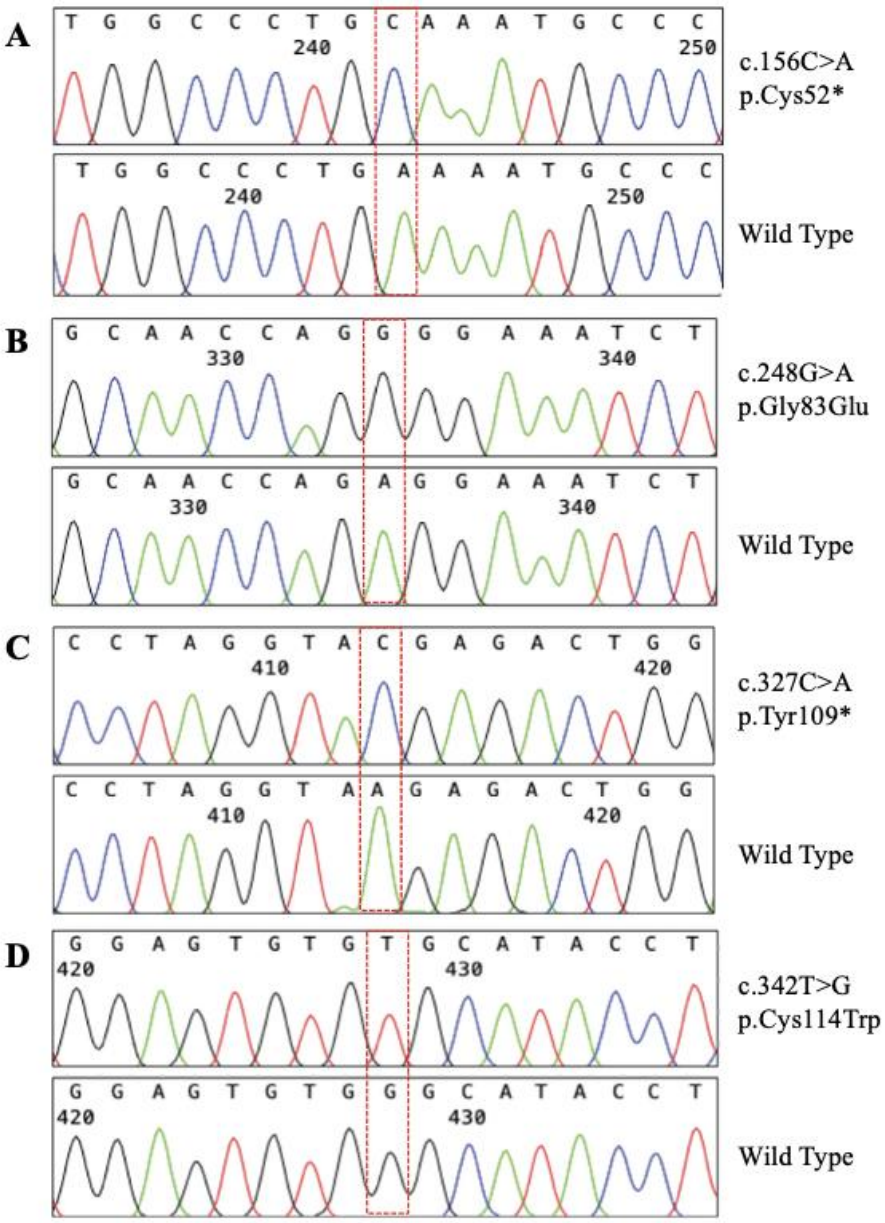

Figure 14. Sanger Sequencing confirmation of *CCN6* variants. Representative chromatograms showing variant (top) and wild-type (bottom) sequences aligned in CodonCode Aligner. Dashed lines mark the verified base substitutions. (A) c.156C>A (p.Cys52*), (B) c.248G>A (p.Gly83Glu), (C) c.327C>A (p.Tyr109*), and (D) c.342T>G (p.Cys114Trp). Each chromatogram displays a distinct single peak at the target site, confirming successful incorporation of the intended base change without additional sequence alterations across the ORF.

4.3 Expression Profiling and Verification of WISP3 Constructs

Following sequence verification, the four PPD-associated *CCN6* variants (p.Cys52*, p.Tyr109*, p.Gly83Glu, and p.Cys114Trp) and the wild-type *WISP3* construct were transiently transfected into human chondrocytes using a lipid-based transfection method. Cells transfected with an empty pcDNA3.1 vector were used as a negative control to establish baseline *CCN6* expression and to serve as a reference for transfection-induced cellular responses. All groups were maintained under identical experimental conditions to ensure comparability among replicates.

To evaluate the transcriptional activity of the expressed plasmids, *CCN6* mRNA levels were quantified by real-time PCR (qPCR) using gene-specific primers. Expression values were normalized to *ACTB* as an internal reference. All transfected groups showed a significant increase in *CCN6* mRNA expression compared to the empty vector control (Figure 15). This confirmed efficient transfection and transcriptional activation, indicating that the sequence variations did not interfere with mRNA synthesis or stability.

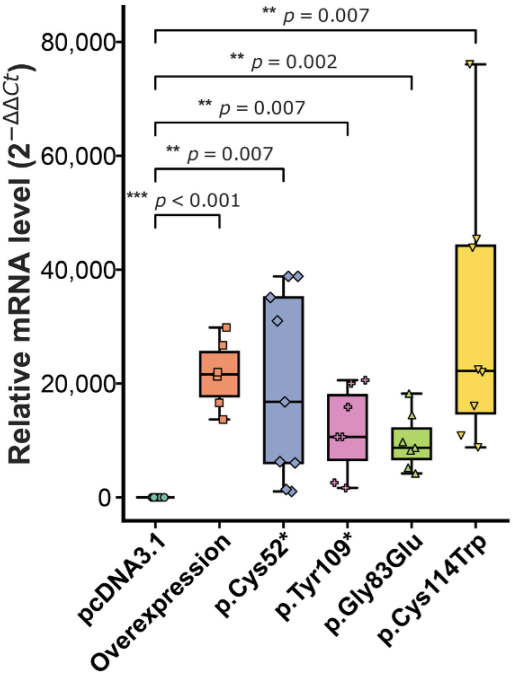

Figure 15. Validation of *CCN6* mRNA expression in human chondrocytes. Human chondrocytes were transfected with plasmids encoding pcDNA3.1, wild-type *CCN6* or *CCN6* variants. Relative *CCN6* mRNA levels were quantified by qPCR and normalized to *ACTB*. Data represent four biological replicates with two technical replicates each (n = 8).

Protein expression was subsequently analyzed by Western blotting using an anti-HA antibody recognizing the N-terminal HA tag present in all constructs. A distinct band corresponding to the full-length WISP3 protein (~41 kDa) was detected in cells expressing the wild-type, p.Gly83Glu, and p.Cys114Trp constructs. The p.Tyr109* variant produced a truncated band of approximately 14 kDa, consistent with premature translation termination within exon 2. In contrast, no HA-reactive signal was detected in cells transfected with the p.Cys52* construct, despite preserved mRNA expression, suggesting either translational inefficiency or rapid degradation of the truncated peptide (Figure 16).

Together, these findings confirmed that all plasmid constructs were transcriptionally active following transfection into human chondrocytes. However, variant-dependent differences in protein detectability revealed distinct post-

transcriptional outcomes, implying that the structural nature and position of the *CCN6* variants differentially affect WISP3 stability and expression *in vitro.*

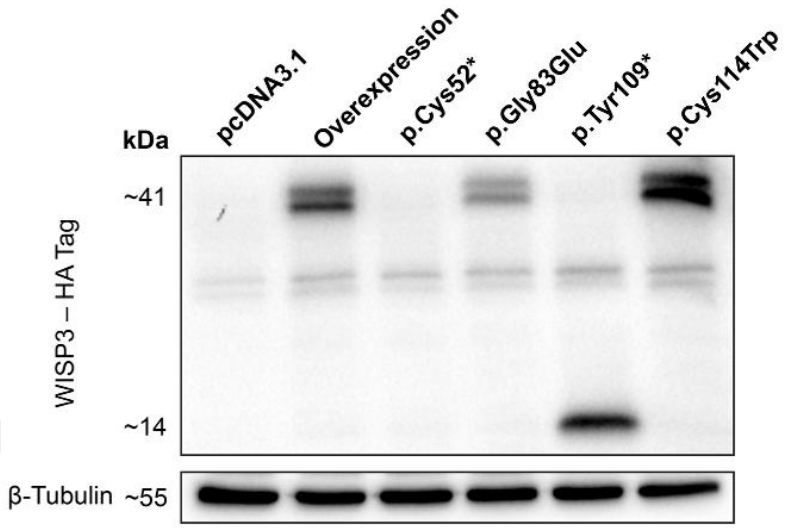

Figure 16. Validation of WISP3 protein expression in human chondrocytes. Western blot analysis of pcDNA3.1, wild-type WISP3 and *CCN6* variants using an anti-HA antibody. β-Tubulin served as a loading control (*n*=3).

4.4 Cell Migration Analyses in WISP3 Variant–Expressing Chondrocytes

The effect of WISP3 variants on chondrocyte motility was assessed using a wound-healing (scratch) assay. Human chondrocytes were transfected with plasmids encoding wild-type WISP3 or the WISP3 variants p.Cys52*, p.Tyr109*, p.Gly83Glu, and p.Cys114Trp, while cells transfected with the empty pcDNA3.1 vector served as the control. After reaching confluence, a uniform scratch was created across the monolayer, and wound closure was monitored by phase-contrast microscopy at 0 h and 24 h (Figure 17A). The open wound area at 24 h was quantified using ImageJ; smaller residual areas indicated greater migratory capacity.

Quantitative analysis revealed variant-dependent alterations in migration. The control group exhibited the most extensive wound closure (mean open wound area = 45.65%), reflecting high basal motility. Cells overexpressing wild-type WISP3 displayed a markedly reduced migration rate (64.51%), confirming its inhibitory role in cell movement. Among the variant-expressing groups, p.Tyr109* promoted a

relatively higher migration (49.91%), whereas p.Cys52* (54.57%) and p.Gly83Glu (54.89%) showed moderate inhibition. The p.Cys114Trp variant closely resembled the wild-type pattern, with a residual wound area of 64.28% (Figure 17B). These results demonstrate that *CCN6* variants modulate chondrocyte migration in a variant-specific manner, suggesting differential effects of *WISP3* alterations on cytoskeletal organization and motility regulation.

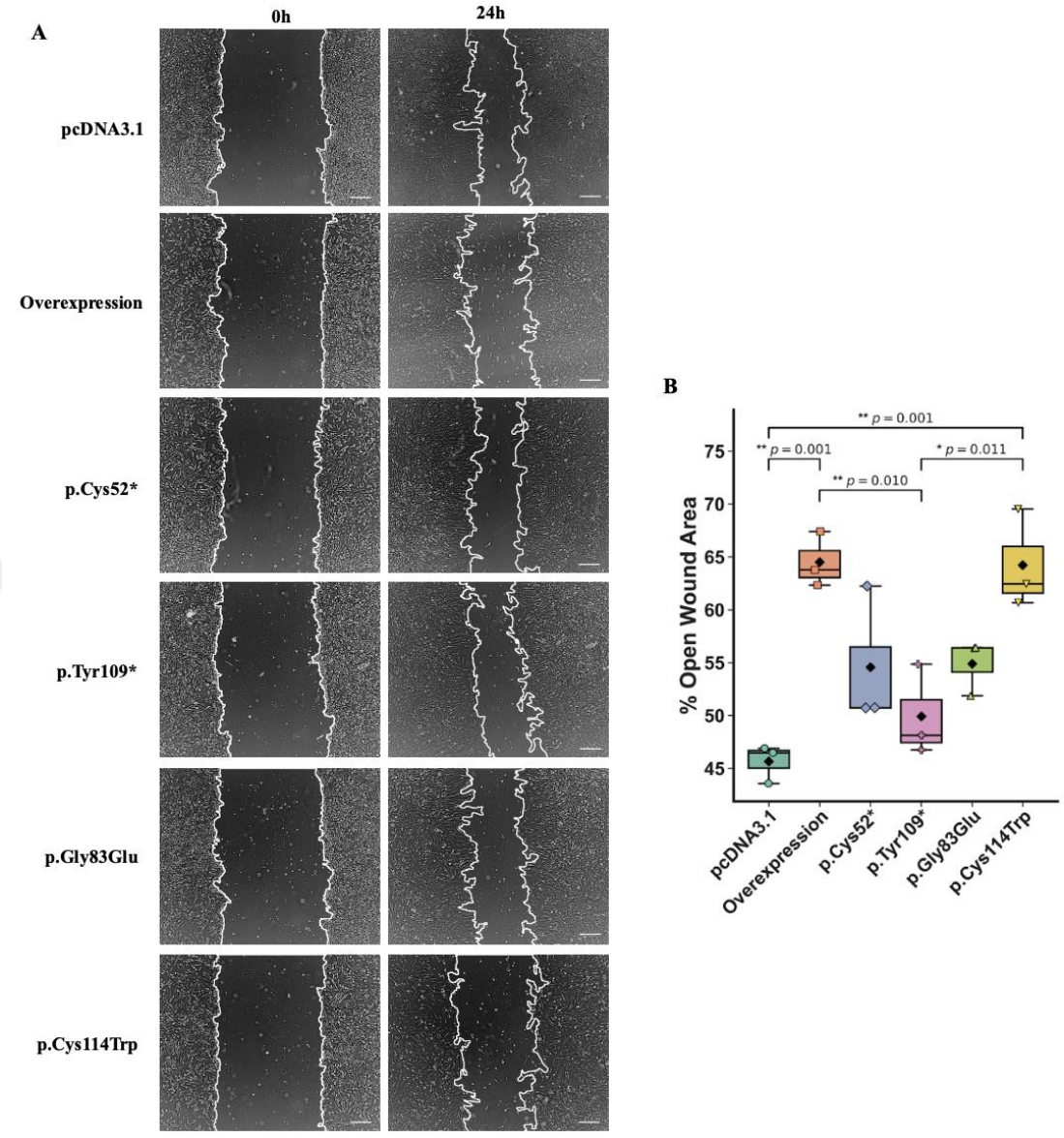

Figure 17. Wound-healing assay of chondrocytes expressing WISP3 variants. (A) Representative phase-contrast images showing wound closure at 0 h and 24 h post-scratch in chondrocytes transfected with wild-type WISP3, *CCN6* variants (p.Cys52*, p.Tyr109*, p.Gly83Glu, p.Cys114Trp), or empty vector control. (B) Quantification of open wound area (%) at 24 h. Data represent three independent biological replicates ($n = 3$). Statistical comparisons were performed using one-way ANOVA followed by Tukey's post hoc test (**$p < 0.01$, ***$p < 0.001$). Images were acquired at 4× magnification; scale bars = 250 µm.

4.5 Cell Viability Assessment by MTT Assay

The effect of *CCN6* variants on chondrocyte viability was evaluated to determine their impact on cellular metabolic activity. Viability was measured 48 hours after transfection using the MTT assay. Absorbance at 570 nm was measured, and results represent the median of three independent biological replicates ($n = 3$). The control group exhibited the highest metabolic activity (median = 0.868), whereas cells overexpressing wild-type *WISP3* showed the lowest viability (median = 0.667). Among the variant groups, p.Cys52* (median = 0.674) and p.Cys114Trp (median = 0.676) demonstrated decreased activity, while p.Tyr109* (median = 0.702) and p.Gly83Glu (median = 0.726) exhibited comparatively higher values. These results indicate that *CCN6* variants differentially affect chondrocyte metabolism, with wild-type overexpression exerting a suppressive effect on cellular viability (Figure 18A).

To examine whether the observed reduction in metabolic activity was dependent on gene dosage, chondrocytes were transfected with increasing amounts of wild-type *CCN6* plasmid (100–1000 ng). Cell viability at each dose was compared to that of cells transfected with 1000 ng pcDNA3.1 control plasmid. A dose-dependent decrease in measured viability was detected (Figure 18B), consistent with a reduction in cell number. This implies that excessive WISP3 expression may negatively affect cell survival or proliferation capacity. Although population-level metrics classify *CCN6* as non-dosage-sensitive (pLI = 0.0; HI = 30; HI% = 48.76; LOEUF = 1.055), these findings indicate that chondrocytes may exhibit a dose-sensitive response to *CCN6* expression levels.

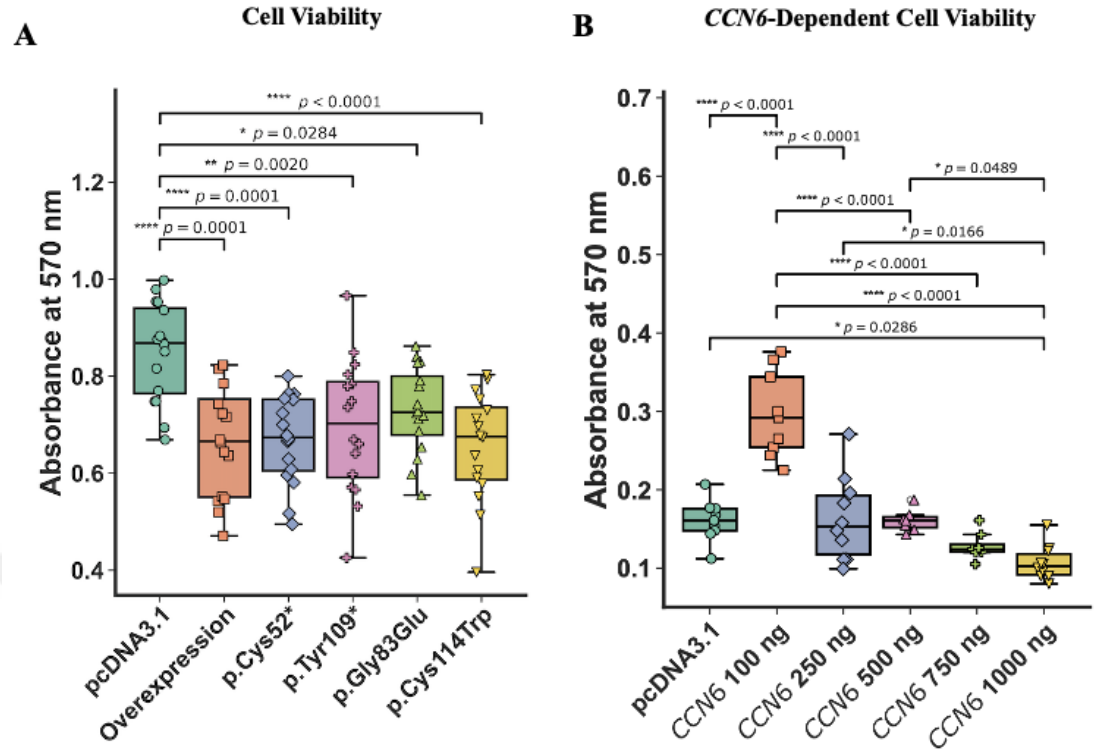

Figure 18. Cell viability of *CCN6*-expressed cells and dose-dependent responses. (A) MTT-based evaluation of chondrocyte viability following wild-type and variant *CCN6* expression (n = 16). (B) Effect of increasing amounts of wild-type *CCN6* plasmid (100–1000 ng) on cell viability relative to 1000 ng pcDNA3.1 control (n = 10). Statistical analysis was performed using one-way ANOVA with Tukey's post hoc test (*p< 0.05, **p< 0.01, ***p < 0.001, ****p < 0.0001).

4.6 Chondrocyte–Matrix Adhesion Analysis

WISP3 functions as a key regulator of ECM organization in chondrocytes (131). The effects of WISP3 alterations on cell–matrix interactions were examined using an adhesion assay performed on type I collagen–coated wells. This assay reflects the adhesive behavior of chondrocytes, a property essential for maintaining cartilage structure and stability. Cells were seeded onto collagen-coated surfaces and incubated under standard conditions. Non-adherent cells were removed by gentle washing, and the remaining attached cells were fixed and stained with crystal violet. The retained dye was solubilized in SDS and quantified spectrophotometrically, with all values normalized to the empty vector control, defined as 1.00.

Overexpression of wild-type WISP3 markedly increased chondrocyte adhesion to the collagen substrate, yielding an average relative value of 1.28 across biological replicates. In contrast, the truncating alterations p.Cys52* and p.Tyr109* resulted in adhesion levels comparable to the control (0.99 and 1.00, respectively), suggesting a loss of function. The missense alterations p.Gly83Glu and p.Cys114Trp produced moderate increases in attachment, with mean values of 1.14 and 1.11, respectively (Figure 19). Collectively, these findings indicate that WISP3 supports chondrocyte–ECM adhesion and that this function is variably impaired depending on the type of sequence alteration.

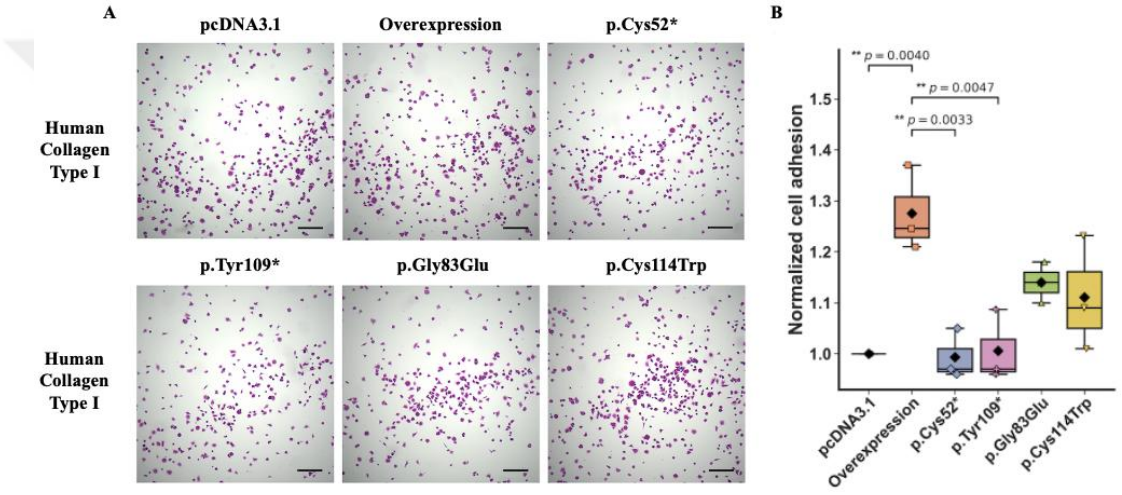

Figure 19. WISP3 variants influence adhesion and ECM interactions. (A) Representative images from the adhesion assay performed on type I collagen–coated wells, acquired using an inverted microscope at 4× magnification. Cells were fixed and stained with crystal violet after seeding (scale bar = 250 µm). (B) Quantification of adherent cells by spectrophotometric measurement of crystal violet retention, normalized to the control (n = 3).

4.7 Gelatin Zymography for MMP-13 Activity Assessment

Matrix metalloproteinases (MMPs) constitute a family of zinc-dependent endopeptidases that regulate ECM renewal and degradation, ensuring cartilage integrity through continuous tissue remodeling. Among them, gelatinases such as MMP-2, MMP-9, and MMP-13 play distinct roles in cartilage physiology. MMP-13 is the major collagenase responsible for cleaving type II collagen, the principal structural component of articular cartilage, and is strongly implicated in chondrocyte-mediated

matrix turnover. Imbalanced MMP activity is associated with pathological cartilage loss observed in degenerative and genetic chondrodysplasias, underscoring its importance in maintaining ECM homeostasis. Given that WISP3 has been proposed to regulate matrix composition and cellular signaling within cartilage tissue, MMP activity was examined to determine whether alterations in WISP3 expression influence matrix remodeling.

Zymographic analysis showed a distinct reduction in gelatinolytic bands in WISP3-overexpressing cells compared to control, indicating a repressive role of WISP3 in matrix degradation. Densitometric quantification revealed that overexpression reduced MMP-13 activity to a median of 70.3% relative to control (set as 100%). Among sequence-altered constructs, p.Cys52* retained the highest residual activity (87.2%), while p.Tyr109* displayed a lower level (62.6%). Both missense changes, p.Gly83Glu and p.Cys114Trp, produced comparable decreases (65.9%), suggesting that specific sequence alterations impair WISP3-dependent regulation of ECM remodeling (Figure 20).

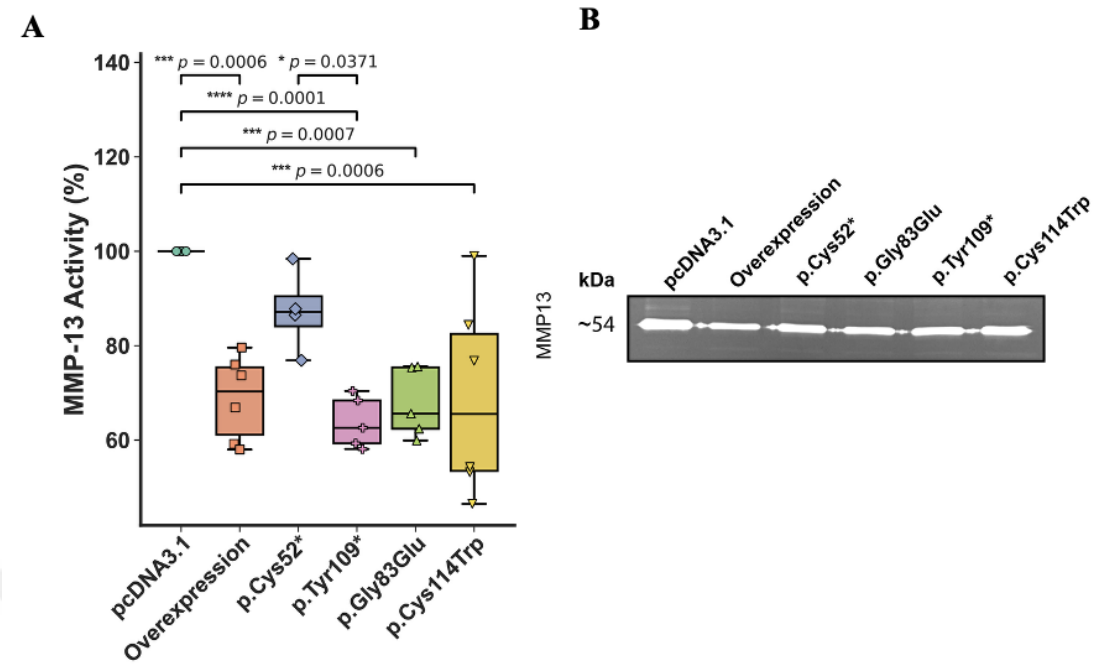

Figure 20. WISP3-associated modulation of MMP activity and ECM remodeling. (A) Quantification of MMP-13 activity measured by gelatin zymography and expressed as percentage relative to the control (n = 6). (B) Representative gelatin zymogram showing MMP-13 activity in conditioned media collected 72 h post-transfection from cells expressing wild-type or variant WISP3 constructs.

4.8 Mitochondrial ROS Quantification by Flow Cytometry and Confocal Microscopy

Disruption of mitochondrial function is a major contributor to oxidative stress and impaired chondrocyte viability. Given that loss of WISP3 activity has been associated with increased intracellular ROS and altered stress signaling, we evaluated whether disease-associated *CCN6* variants disturb mitochondrial homeostasis, which plays a central role in sustaining chondrocyte function and cartilage stability (14).

Live-cell flow cytometry was used to quantify mitochondrial reactive oxygen species (ROS) and total mitochondrial mass using MitoSOX Red and MitoTracker Green FM, respectively. Both dyes require active mitochondria; therefore, fixation was not applied, and concentrations were selected within non-toxic ranges to avoid artificial signals. Forty-eight hours after transfection, cells were stained under three parallel conditions: MitoSOX-only and MitoTracker-only samples were used to

confirm dye specificity and to perform fluorescence compensation, while co-stained samples were used for quantitative analyses. Fluorescence was detected in the PE (MitoSOX) and FITC (MitoTracker) channels, and 20,000 events were recorded per sample using a BD FACSCanto II cytometer. Mean fluorescence intensity (MFI) values were obtained after compensation and single-cell gating (Figure 21), with detailed gating strategy and data provided in Appendix 1.

Figure 21 shows representative histogram overlays plotted on a logarithmic x-axis (fluorescence intensity) and linear y-axis (event count), illustrating the distribution of MitoSOX and MitoTracker signals across cell populations. MitoTracker fluorescence was used as an indicator of mitochondrial content, whereas MitoSOX reflected superoxide accumulation. The ratio of MitoSOX to MitoTracker MFI provided a normalized index of ROS production per unit mitochondrial mass, and values shown in Figure 21C represent the mean of biological replicates. Among the variants, p.Tyr109* exhibited the highest mean ROS/mass ratio (1.14), followed by p.Cys114Trp (1.13) and p.Gly83Glu (1.04), while p.Cys52* and overexpression conditions remained near baseline (0.99 and 1.01, respectively). These results indicate that specific WISP3 variants elevate mitochondrial ROS beyond proportional changes in mitochondrial content, suggesting variant-dependent disruption of redox balance that may contribute to chondrocyte dysfunction.

Representative confocal microscopy images (Figure 21D) acquired under identical live-staining conditions supported these findings. Cells expressing p.Tyr109* and p.Cys114Trp displayed strong MitoSOX fluorescence relative to MitoTracker, whereas p.Cys52* expressing cells showed weak red signals. The imaging data align with flow cytometry results and highlight differential oxidative responses induced by individual *CCN6* variants.

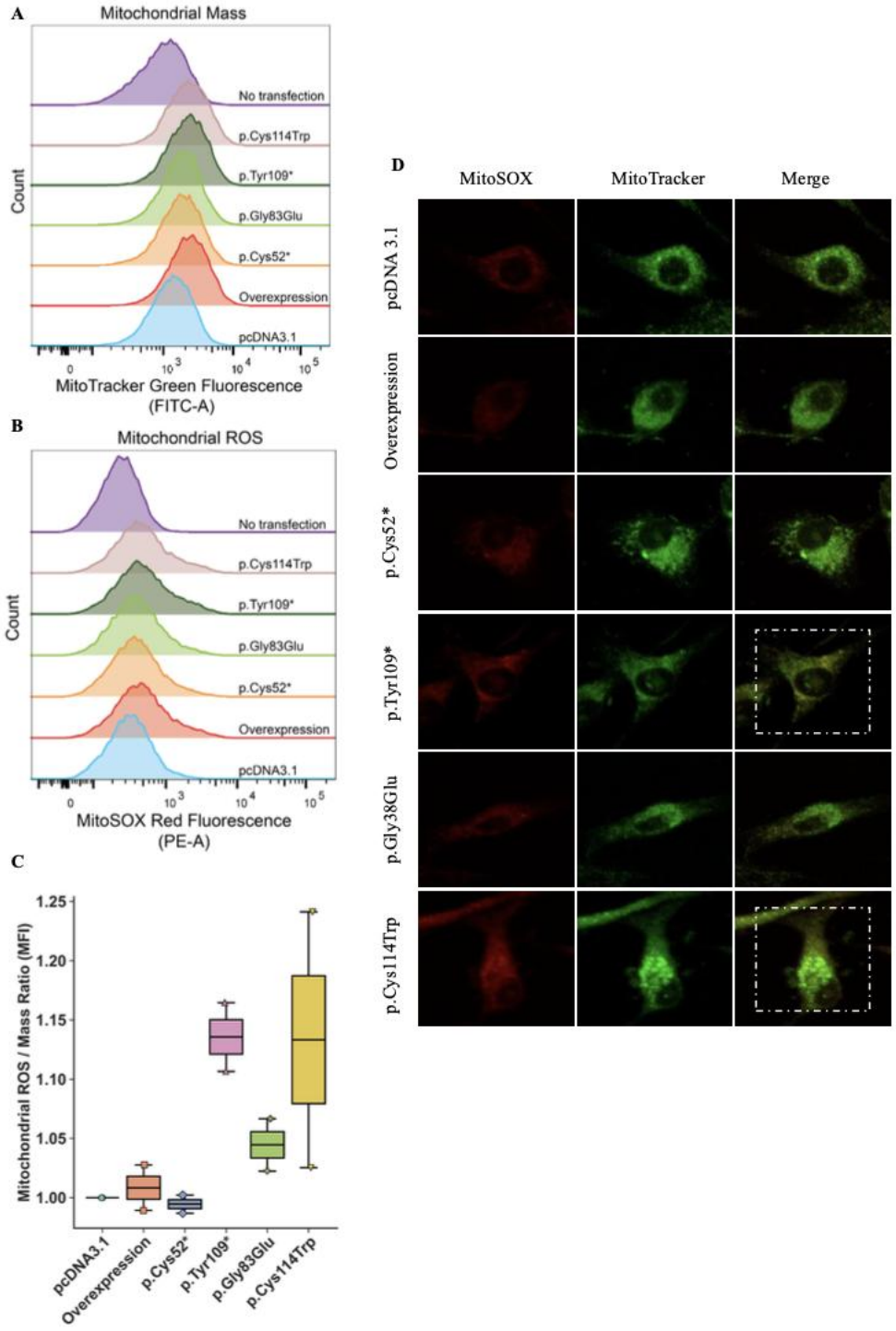

Figure 21. Mitochondrial ROS quantification and visualization in chondrocytes expressing WISP3 variants. (A) Representative flow cytometry histograms showing mitochondrial mass, measured by MitoTracker Green fluorescence (FITC-A). The x-axis represents fluorescence intensity on a logarithmic scale, and the y-axis indicates event count. (B) Histogram overlays of mitochondrial ROS levels, measured by MitoSOX Red fluorescence (PE-A), under identical acquisition settings. (C) Boxplot illustrating the mean mitochondrial ROS-to-mass ratio (MitoSOX/MitoTracker MFI)

calculated from biological replicates. Each data point represents the average of replicate measurements; error bars indicate standard deviation (n = 2). (D) Representative confocal microscopy images of live chondrocytes co-stained with MitoSOX Red (red) and MitoTracker Green FM (green). Merge panels show overlapping mitochondrial signals. Cells expressing p.Tyr109* and p.Cys114Trp display elevated MitoSOX intensity relative to MitoTracker, consistent with flow cytometry data. Scale bar = 10 µm.

4.9 Evaluation of ER Stress Marker Expression in WISP3 Variant–Expressing Chondrocytes

Endoplasmic reticulum (ER) stress plays a central role in maintaining chondrocyte proteostasis, and its dysregulation contributes to cellular dysfunction in several genetic skeletal disorders and matrix-related pathologies(28,132). Disturbances in protein folding and trafficking lead to the accumulation of unfolded proteins within the ER lumen, activating the unfolded protein response (UPR), a signaling network that coordinates protein refolding, degradation, and temporary reduction of protein synthesis to restore ER balance. When these mechanisms fail to resolve the stress, the UPR shifts from adaptive signaling toward apoptosis, compromising chondrocyte survival.

Among the key mediators of this pathway, *CHOP* (C/EBP homologous protein) acts as a transcription factor downstream of the *PERK–eIF2α–ATF4* cascade and promotes apoptosis during sustained ER stress, whereas spliced XBP1 (*sXBP1*) represents the active form generated through IRE1α-dependent mRNA splicing, enhancing ER protein folding capacity and the degradation of misfolded proteins. The ratio of spliced to unspliced XBP1 (*s/uXBP1*) reflects the adaptive potential of the cell. Assessing these two UPR markers therefore provides a means to distinguish terminal and compensatory responses. Since WISP3 has been linked to intracellular stress regulation, we investigated whether PPD-associated *CCN6* variants alter ER stress signaling in chondrocytes.

Each condition was analyzed by quantitative PCR in three biological replicates, each containing multiple technical replicates. Because averaging technical replicates may underestimate intra-sample variability, data were evaluated using a linear mixed-

effects (LME) model to account for both biological and technical levels of variation, allowing more accurate estimation of mean differences (133).

As shown in Figure 21D, all WISP3-expressing groups exhibited variable degrees of UPR activation compared with the pcDNA3.1 control (set as 1.00 ± 0.10). The p.Cys114Trp variant produced the highest induction of both *CHOP* (3.60 ± 1.37-fold) and *s/uXBP1* (4.77 ± 1.72-fold), indicating broad activation of ER stress signaling. Similarly, overexpression resulted in increased *CHOP* (3.00 ± 0.94-fold) and *s/uXBP1* (3.15 ± 0.82-fold) expression, suggesting that elevated WISP3 levels can challenge ER function even without sequence alterations. The p.Tyr109***** variant primarily upregulated *CHOP* (2.65 ± 1.18-fold) without a comparable increase in *s/uXBP1* (1.30 ± 0.57-fold), reflecting a pro-apoptotic response. In contrast, the p.Gly83Glu variant triggered a strong *s/uXBP1* increase (3.37 ± 0.92-fold) but only moderate *CHOP* elevation (2.16 ± 1.13-fold), consistent with an adaptive profile. The p.Cys52***** variant caused minimal upregulation of both transcripts (*CHOP* = 1.72 ± 0.56-fold; *s/uXBP1* = 1.47 ± 0.81-fold), indicating limited ER stress (Figure 22A).

To integrate these findings, the *CHOP/sXBP1* ratio was calculated as a quantitative indicator of the balance between pro-apoptotic and adaptive UPR signaling. A ratio above 1 denotes a predominance of *CHOP*-driven apoptosis, whereas a ratio below 1 reflects adaptive stress resolution. Among all variants, p.Tyr109***** displayed the highest ratio (2.63 ± 1.54), indicating insufficient activation of adaptive mechanisms. By contrast, p.Cys114Trp (0.76 ± 0.37) and p.Gly83Glu (0.80 ± 0.40) showed lower ratios, suggesting preserved adaptive capacity despite elevated ER stress (Figure 22B). The p.Cys52*****, overexpression, and control groups maintained ratios near 1.0, representing balanced UPR activation.

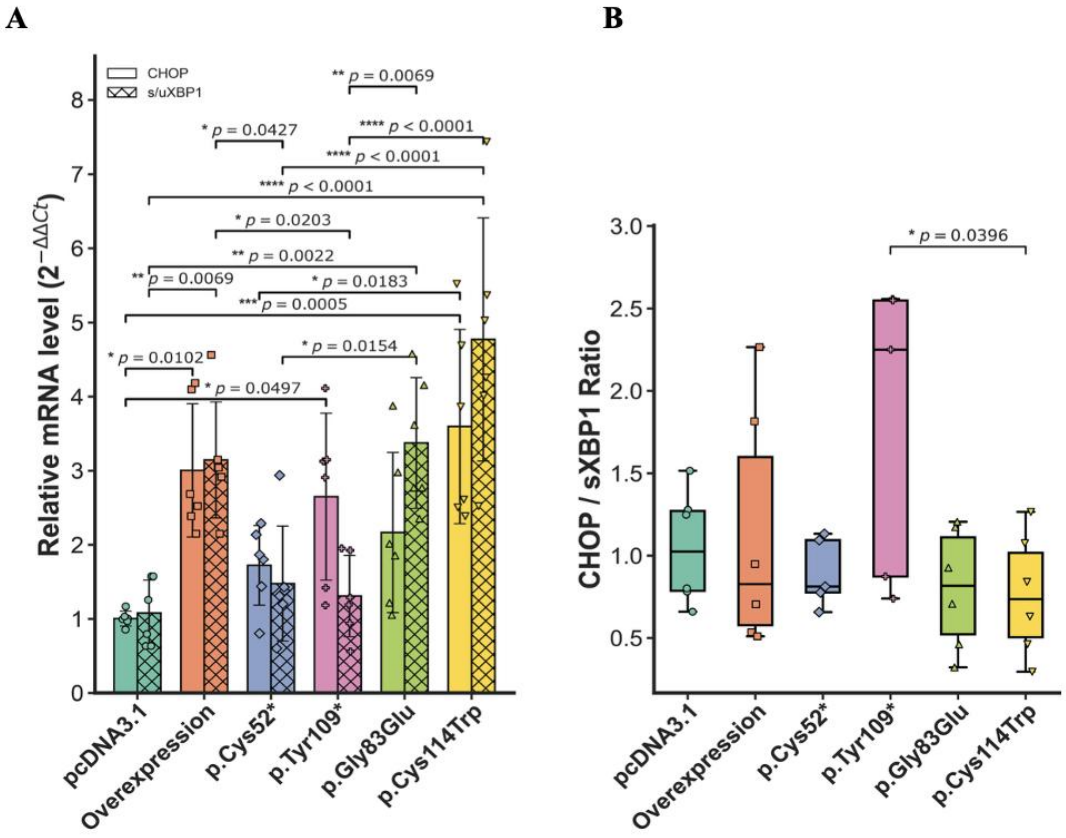

Figure 22. Expression analyses of ER stress markers in PPD-associated variants. (A) Relative mRNA expression levels of *CHOP* and spliced/unspliced *XBP1* (s/uXBP1) determined by quantitative PCR. Data represent mean ± SD (n = 6). (B) *CHOP/sXBP1* expression ratio calculated as an indicator of the balance between pro-apoptotic and adaptive UPR signaling. Statistical analysis was performed using one-way ANOVA followed by Tukey's post hoc test. Significance is indicated as *p < 0.05, **p < 0.01, ***p < 0.001, ****p < 0.0001.

Collectively, these data demonstrate that WISP3 variants differentially regulate ER stress signaling in chondrocytes. While p.Tyr109* favors a maladaptive, *CHOP*-dominant response, p.Cys114Trp and p.Gly83Glu primarily activate adaptive *XBP1*-dependent signaling. These variant-specific stress patterns may underlie distinct cellular outcomes contributing to PPD pathogenesis.

4.10 Subcellular Localization of WISP3 Variants by Co-Localization Analysis

WISP3 has been previously reported to localize within mitochondria in chondrocytes, suggesting a potential functional association with mitochondrial integrity and dynamics. TOM20, an outer mitochondrial membrane protein, was used as a reference marker to visualize mitochondria and evaluate whether disease-associated *CCN6* variants alter WISP3's subcellular localization pattern. Human chondrocytes were transfected with HA-tagged wild-type or variant constructs and subjected to immunofluorescence staining using anti-HA to detect WISP3 (red), TOM20 for mitochondria (green), and DAPI for nuclei (blue) (Figure 23A). The spatial relationship between WISP3 and mitochondrial signals was analyzed by confocal microscopy. Co-localization was quantified using the Pearson correlation coefficient (R^2), which reflects the linear intensity correlation between the two fluorescence channels, and the Manders' M2 coefficient, which measures the fraction of WISP3 signal overlapping with TOM20. Quantification was performed on ≥25 cells per biological replicate ($n = 3$).

Cells expressing wild-type WISP3 exhibited a Pearson coefficient of 0.539 and a Manders' M2 value of 0.682, indicating moderate mitochondrial localization. In contrast, control cells transfected with the empty vector showed much lower overlap (Pearson = 0.269; M2 = 0.307). Among the variants, p.Cys52* showed slightly reduced correlation (Pearson = 0.453; M2 = 0.666), whereas p.Gly83Glu (Pearson = 0.496; M2 = 0.689) and p.Tyr109* (Pearson = 0.518; M2 = 0.828) displayed higher values. The p.Cys114Trp variant demonstrated the strongest co-localization (Pearson = 0.562; M2 = 0.811), suggesting that these variants differentially influence WISP3's intracellular distribution, potentially through altered mitochondrial targeting or retention mechanisms (Figure 23B,C).

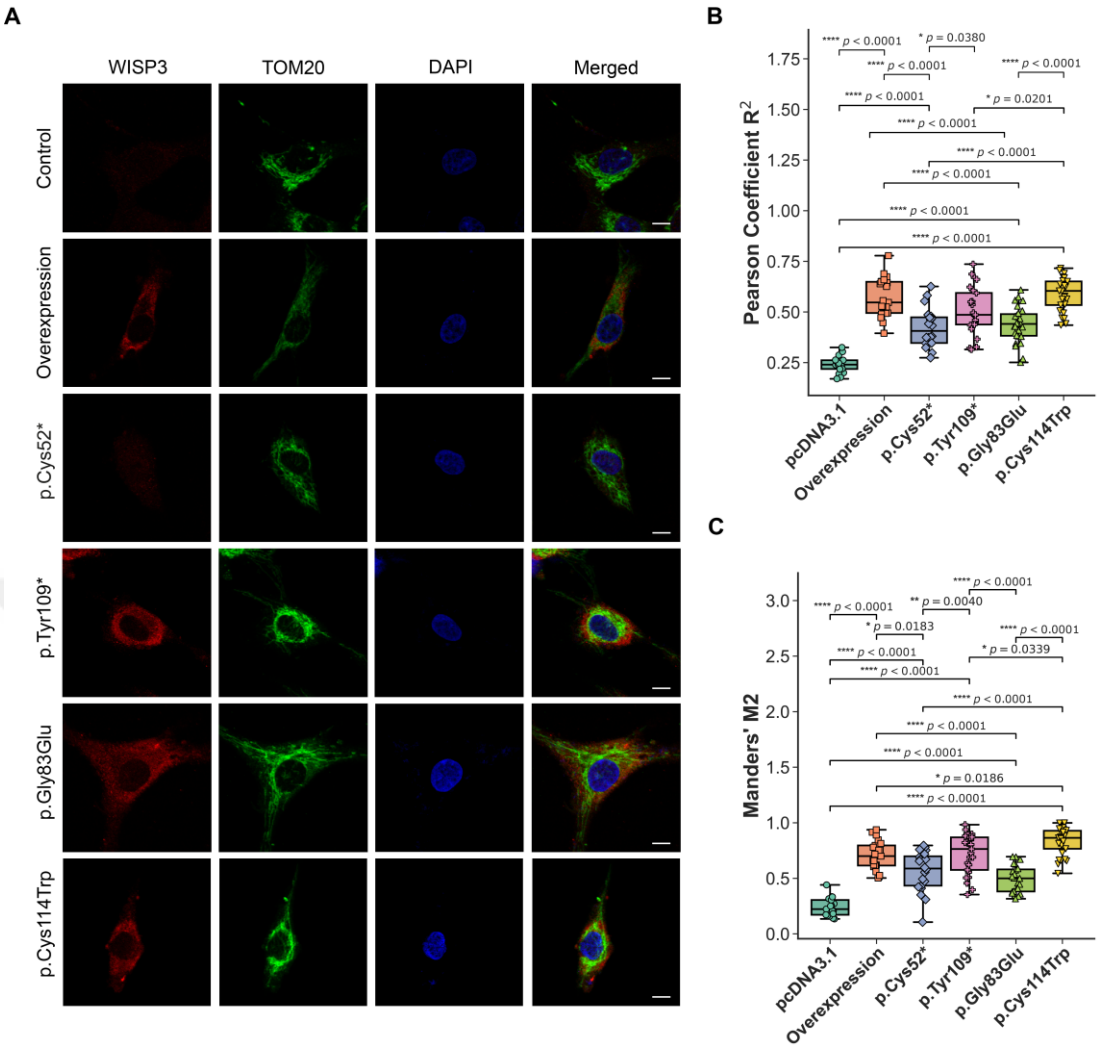

Figure 23. Mitochondrial localization patterns of wild-type and disease-associated WISP3 variants. (A) Representative confocal images showing WISP3 (red), mitochondrial marker TOM20 (green), and nuclei (DAPI, blue) in chondrocytes transfected with wild-type or variant WISP3 constructs. Merged images display the extent of co-localization between WISP3 and mitochondria. Scale bar: 10 µm. (B) Quantification of WISP3–TOM20 co-localization using the Pearson coefficient (R^2), showing a significantly lower value in p.Cys52* compared to other variants. (C) Manders' M2 coefficient representing the fraction of WISP3 signal overlapping with TOM20. Data represent ≥25 cells per condition from three independent biological replicates. Statistical analysis was performed using one-way ANOVA followed by Tukey's post hoc test. Significance is shown as * $p < 0.05$, ** $p < 0.01$, **** $p < 0.0001$.

4.11 Whole Transcriptome Profiling of *CCN6* Variants

RNA-seq analysis was conducted to investigate how nonsense and missense variants of *CCN6* affect the global transcriptional landscape of chondrocytes. Human chondrocytes were transfected with wild-type WISP3 (OE), p.Cys52*, or p.Cys114Trp constructs, and total RNA from two biological replicates per condition was sequenced using the Illumina NovaSeq 6000 platform. After adapter trimming and quality filtering, high-quality reads were aligned to the human reference genome, and expression levels were normalized as Transcripts Per Million (TPM).

Correlation and variance analyses were performed to assess the consistency and separation among transcriptomic profiles. The heatmap of pairwise Pearson correlation coefficients based on TPM values demonstrated high reproducibility between biological replicates ($R^2 > 0.95$) across all samples, confirming the reliability of the dataset (Figure 24A). Principal component analysis (PCA) further revealed distinct clustering of the OE, p.Cys52*, and p.Cys114Trp groups, which together accounted for 56% and 21.4% of the total variance along the first two principal components. This separation reflects clear transcriptomic divergence between the wild-type and variant conditions (Figure 24B).

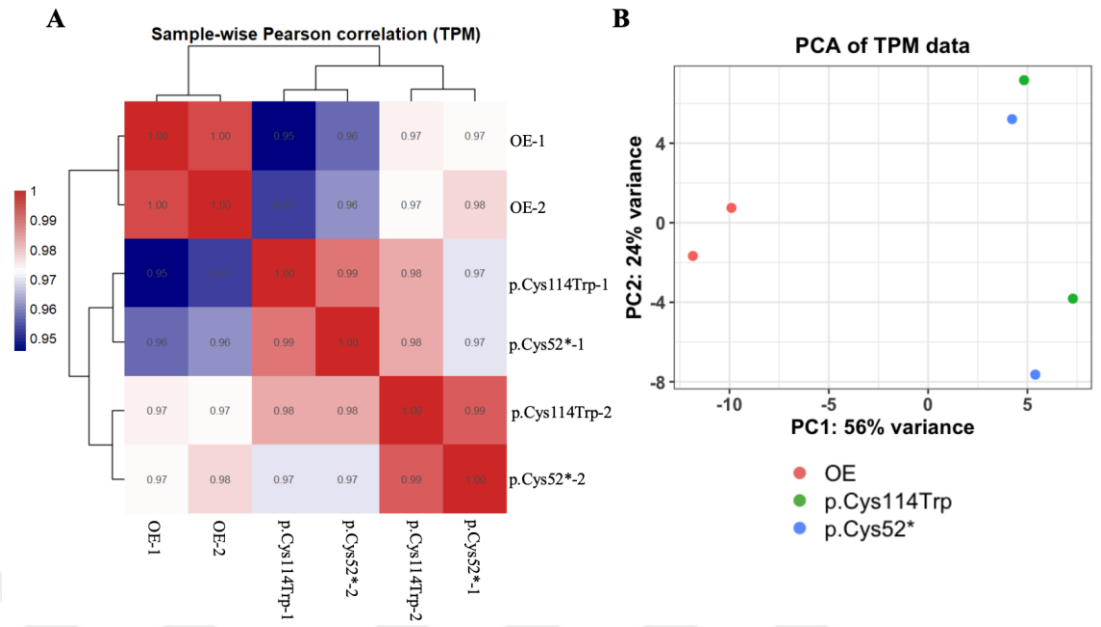

Figure 24. Transcriptomic similarity and variance among experimental groups. (A) Heatmap showing pairwise Pearson correlation coefficients (R^2) based on TPM values across all samples, confirming high reproducibility between replicates. (B) Principal component analysis (PCA) of TPM-normalized data. The first two components explain 56% and 21.4% of total variance, illustrating distinct clustering of OE, p.Cys52*, and p.Cys114Trp groups (n = 2).

Differential expression analysis identified 390 genes significantly altered in p.Cys52* (141 upregulated, 249 downregulated) and 406 genes in p.Cys114Trp (146 upregulated, 260 downregulated) relative to the wild-type overexpression group (Figure 25A,B). Both variants elicited notable transcriptomic alterations; however, the magnitude and complexity of these changes were greater in p.Cys114Trp.

Furthermore, GO enrichment analysis (Figure 25C,D) indicated that the p.Cys52* variant was associated with a smaller number of enriched biological processes, suggesting a more limited transcriptional response. This observation is consistent with earlier experimental results demonstrating that p.Cys52* does not produce a stable or functional protein, likely due to rapid degradation, resulting in a restricted transcriptional profile. In contrast, p.Cys114Trp activated a broader network of genes associated with ER stress, unfolded protein response (UPR), and cell death regulation, indicating an extensive stress-related adaptation at the transcriptomic level.

The significantly regulated genes were further categorized into eight functional groups, revealing three major expression patterns (Figure 25E). The first cluster, comprising *CSNK1A1L*, *ANP32CP*, *NME2P1*, and *RAB6D*, showed increased expression in both variants but remained low in the wild-type condition, representing a variant-driven transcriptional activation group. The second cluster included genes upregulated exclusively in p.Cys114Trp, such as *ATF3*, *PLCG2*, *PDIA2*, *DNAJB9*, *HERPUD1*, *HSPA5*, *DDIT3*, *PDIA4*, and *HYOU1*. These genes were suppressed or unchanged in p.Cys52* and OE cells and are functionally related to ER stress, UPR, and programmed cell death, indicating a variant-specific stress response pattern. The third group consisted of genes upregulated only in the wild-type overexpression condition, primarily linked to protein localization to the ER and cytoskeletal organization, reflecting preserved structural and trafficking processes that were attenuated in both variants.

Collectively, these results indicate that the nonsense and missense variants of *CCN6* produce distinct transcriptomic effects in chondrocytes: p.Cys52* displays a limited response consistent with loss of protein stability, whereas p.Cys114Trp drives a broader transcriptional activation involving ER stress and apoptotic pathways.

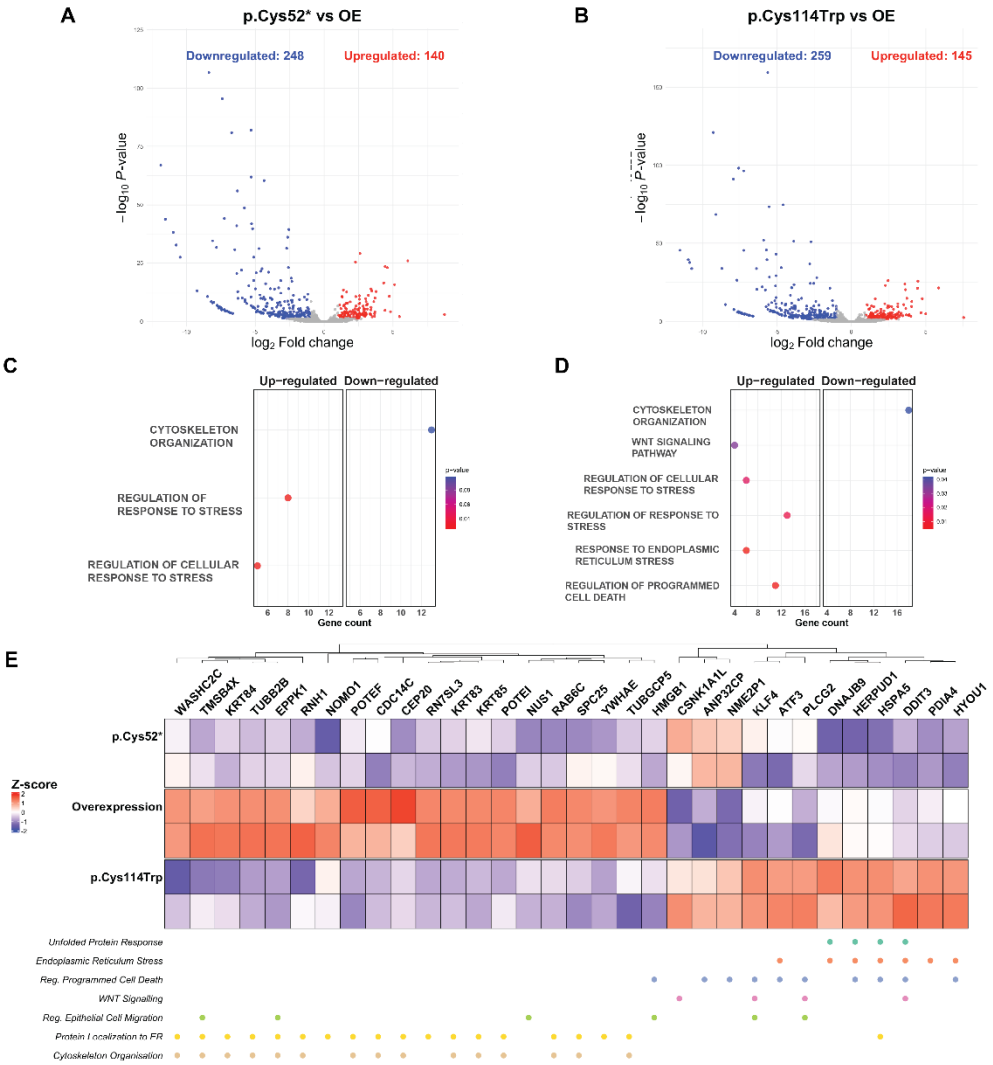

Figure 25. Transcriptomic profiling of disease associated *CCN6* variants. Human chondrocytes were transfected with wild-type *CCN6* (overexpression), p.Cys52*, or p.Cys114Trp constructs, and whole-transcriptome sequencing was carried out (n = 2). (A,B) Volcano plots showing differentially expressed genes (DEGs) in p.Cys52***** (A) and p.Cys114Trp (B) compared with wild-type WISP3-overexpressing cells. Red and blue points indicate significantly upregulated and downregulated genes, respectively (adjusted $p < 0.05$, $|\log_2 FC| > 1$). (C,D) Gene Ontology (GO) enrichment analysis of significantly regulated genes in p.Cys52***** (C) and p.Cys114Trp (D). The color gradient represents the adjusted p-value, and dot size indicates the number of genes associated with each GO term. (E) Heatmap displaying hierarchical clustering of significantly altered genes across p.Cys52*, wild-type, and p.Cys114Trp groups. Functionally related clusters associated with unfolded protein response, mitochondrial metabolism, and cytoskeletal organization are shown below. Z-scores represent normalized gene expression values.

4.12 Protein–Protein Interaction Profiling of WISP3

Variant-dependent interaction dynamics of WISP3 were examined by expressing HA-tagged wild-type, p.Tyr109*, and p.Cys114Trp constructs in chondrocyte cell lines. As the p.Cys52* variant did not produce detectable protein, another truncated form (p.Tyr109*) was chosen to enable comparison between full-length and partially truncated WISP3, thereby assessing the contribution of the C-terminal region to the interaction network. The p.Cys114Trp variant was included to evaluate the impact of structural destabilization and to facilitate direct comparison with transcriptomic findings.

Exogenous WISP3 proteins were enriched using anti-HA co-immunoprecipitation, ensuring selective isolation of WISP3-associated complexes. Pulldown efficiency and specificity were verified by Western blotting and Coomassie staining. The isolated complexes were subsequently analyzed by liquid chromatography–tandem mass spectrometry (LC–MS/MS), allowing systematic identification of both shared and variant-specific interactors.

Comparative proteomic analysis revealed both shared and variant-specific WISP3 interactors (Figure 26). Among all experimental groups, 18 proteins were identified as common interactors, whereas 35 were shared between wild-type and p.Tyr109*, 64 between wild-type and p.Cys114Trp, and 20 between the two variant conditions. Each construct also exhibited unique interaction partners reflecting distinct structural contexts. Quantitative analysis showed that the p.Tyr109* variant altered 34 proteins (16 upregulated, 18 downregulated), while p.Cys114Trp affected 40 proteins (20 upregulated, 20 downregulated). To ensure data quality, common LC–MS/MS contaminants such as keratins were excluded from the dataset.

These results indicate that both variants diverge from the wild-type interactome yet through different mechanisms. The truncated form (p.Tyr109*) displayed a reduced and compositionally restricted interaction profile, suggesting loss of critical binding interfaces. In contrast, the missense variant p.Cys114Trp demonstrated an

expanded yet reorganized set of protein associations, implying altered network stability and potential remodeling of WISP3's molecular interactions.

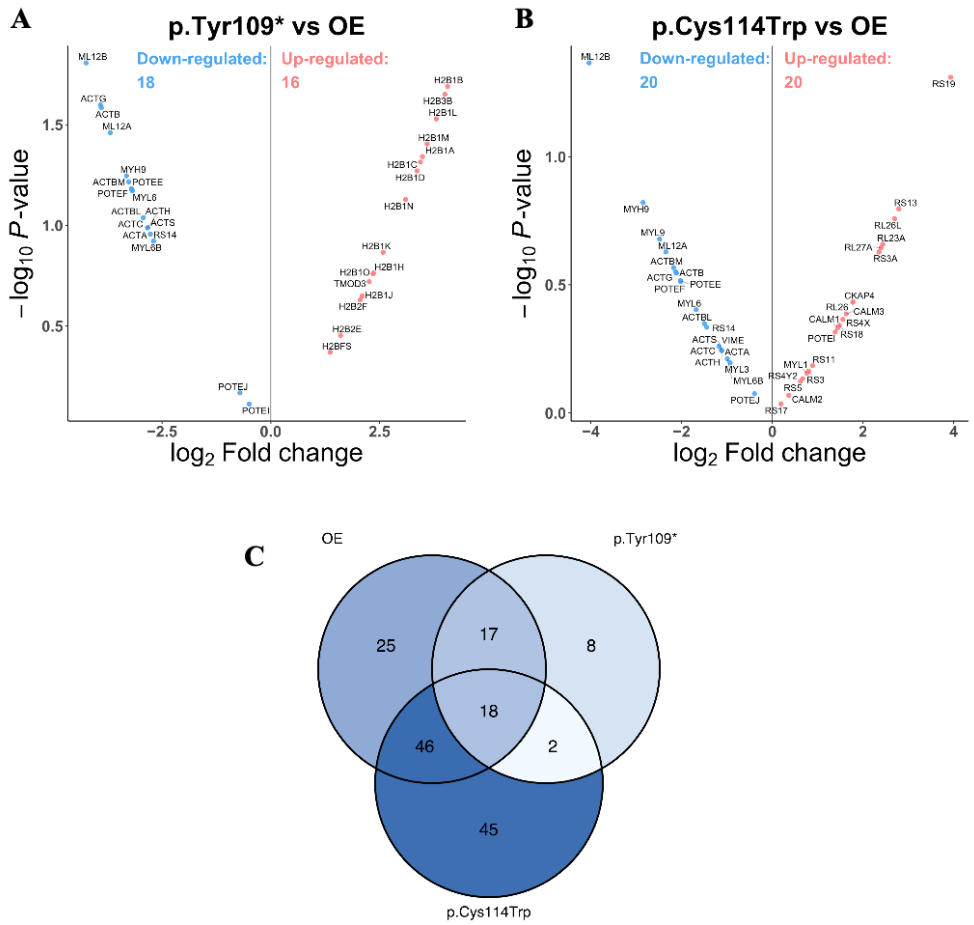

Figure 26. Comparative proteomic profiling of wild-type and variant WISP3 interactomes. (A,B) Volcano plots displaying differentially enriched proteins in chondrocytes expressing the truncated p.Tyr109* (A) and missense p.Cys114Trp (B) variants compared with wild-type WISP3 (OE). Significantly up- and downregulated proteins are shown in red and blue, respectively (adjusted $p < 0.05$, $|\log_2 FC| > 1$). (C) Venn diagram summarizing the overlap among wild-type (OE), p.Tyr109*, and p.Cys114Trp conditions, illustrating the number of shared and variant-specific interactors identified by LC–MS/MS ($n = 2$).

Protein–protein interaction network mapping (Figure 27) revealed clear differences in network organization among wild-type and variant WISP3 interactomes. The wild-type protein established a compact and highly connected network architecture, whereas the p.Cys114Trp variant interacted with a larger number of partners that were redistributed into a less cohesive structure, suggesting a

reorganization driven by reduced protein stability. In contrast, the truncated p.Tyr109* variant exhibited the fewest and most dispersed interactions, consistent with the loss of major binding interfaces following structural disruption of WISP3.

Functional classification of interactors showed enrichment across cell death, cytoskeletal organization, endoplasmic reticulum (ER) function, intracellular localization, mitochondrial processes, stress response, unfolded protein response (UPR), and WNT signaling categories. Cytoskeletal components constituted the dominant cluster, forming the core intersection shared by all three groups. This common subset included multiple actin and tubulin isoforms such as ACTB, ACTC, ACTG, ACTA, TUBA1A, TUBA1B, TUBB2A, TUBB3, and TUBB5, as well as MYH9, MYL6, and CALM1–3, reflecting WISP3's fundamental association with the cytoskeletal framework.

Variant-specific subsets highlighted distinct biological tendencies. Proteins unique to p.Cys114Trp, including HSPB1, DDX5, NACAM, AP2A1, and TBA8, were enriched in stress adaptation, ER function, and vesicular trafficking pathways, consistent with a stress-associated remodeling of cellular organization. Shared interactors between p.Cys114Trp and OE (e.g., TBB2A, MYL9, CALM1, CAVN1) represented retained but quantitatively altered associations. The overlap of p.Cys114Trp, p.Tyr109*, and OE was dominated by structural elements (ACTB, ACTC, ACTS, ACTBM, ML12A, ML12B, MYH9, POTEF, and POTEI), underscoring the persistence of cytoskeletal scaffolding despite variant-induced changes in network organization. Conversely, interactors unique to p.Tyr109*, such as ZC3HD, PI2R, SPSB3, and ZN792, were sparse and functionally scattered, consistent with network collapse in truncated WISP3.

Proteins associated with WNT signaling (e.g., CKAP4, CALM1–3) were present in multiple interaction categories, suggesting that WISP3 may influence signaling–structural coupling through shared intermediates. Several interactors overlapped with genes identified in the RNA-seq dataset, including TUBB1A, TUBB2A, TUBB2B, POTEF, and POTEI, supporting the cross-consistency of proteomic and transcriptomic

findings. Collectively, these data indicate that while p.Tyr109* primarily reflects a loss-of-function and interaction collapse, p.Cys114Trp promotes expansion and redistribution of the WISP3 network, aligning with its broader stress-related phenotype.

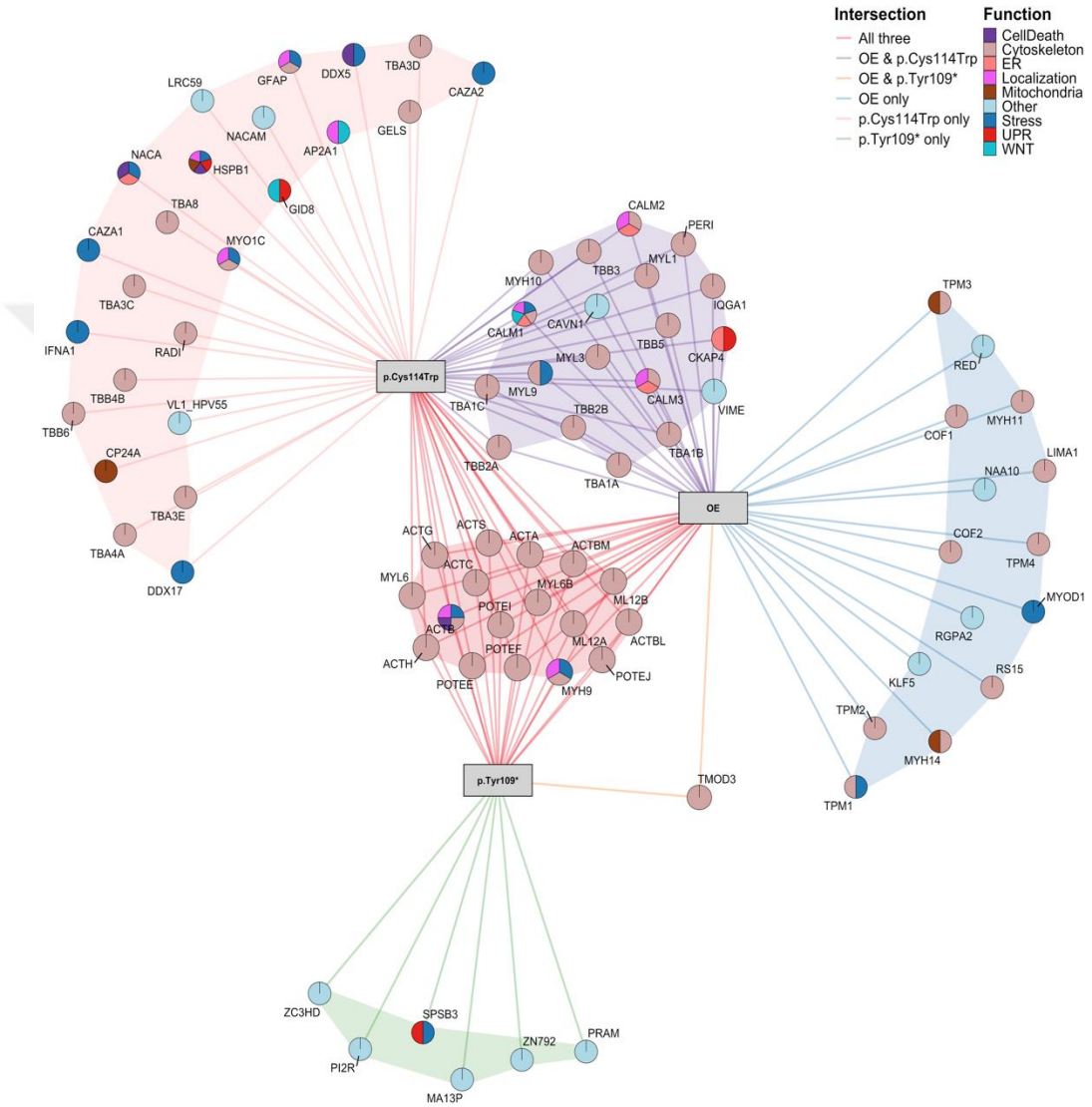

Figure 27. Protein-protein interaction network of wild-type and variant WISP3. Protein–protein interaction networks generated from LC–MS/MS–based co-immunoprecipitation analysis (n = 2) illustrate distinct interactome architectures for wild-type (OE), p.Tyr109*, and p.Cys114Trp constructs. Node colors correspond to functional categories: cell death, cytoskeletal organization, endoplasmic reticulum (ER) function, localization, mitochondrial processes, stress response, unfolded protein response (UPR), and WNT signaling. Node outlines indicate the interaction overlap among conditions.

The complete interactome dataset is available in Appendix 2, and the list of interactors and their classification is provided in Appendix 3.

5 DISCUSSION

In this study, four *CCN6* variants associated with Progressive Pseudorheumatoid Dysplasia (PPD) were functionally investigated using a human chondrocyte cell culture model. All variants are located within the IGFBP domain of WISP3, enabling a direct comparison between nonsense and missense alterations under controlled cellular conditions. Among these, p.Gly83Glu, p.Tyr109*, and p.Cys114Trp had not previously been functionally examined in cell-based systems, providing novel insights into their biological consequences.

Transcript and protein expression analyses were performed following transfection. qPCR revealed increased *CCN6* mRNA levels in all variant and wild-type expressing groups relative to the control group, indicating that none of the variants impaired transcription or destabilized the transcript. However, the downstream protein outcomes diverged markedly. Full-length WISP3 was observed in both missense variants, whereas nonsense variants exhibited distinct patterns: p.Tyr109* produced a truncated product, while p.Cys52* resulted in complete loss of detectable WISP3 protein despite robust transcript expression. The absence of detectable protein in p.Cys52* suggests either efficient targeting of its transcript by the nonsense-mediated mRNA decay (NMD) pathway or rapid post-translational degradation. In contrast, the presence of a truncated WISP3 product in p.Tyr109* implies partial escape from NMD surveillance or reduced efficiency of this pathway, depending on the sequence context of the premature termination codon (PTC). It is also important to note that immunoblotting was performed using an antibody recognizing the N-terminal region of WISP3, which allows detection of truncated species but not C-terminal fragments; therefore, the absence of full-length protein in nonsense variants cannot be attributed to antibody incompatibility. These findings highlight that NMD activity can vary depending on both the position and the local nucleotide environment of the PTC (134–136).

Beyond transcript-level regulation, structural stability analyses provided further insights into how specific variants may compromise WISP3 function through conformational disruption. The substantial destabilization predicted for the p.Cys114Trp variant aligns with its impaired functional behavior observed experimentally, as well as with its classification as pathogenic in clinical databases. In contrast, the p.Gly83Glu variant was associated with only a mild destabilizing effect. Large ΔΔG values exceeding +40 kcal/mol—such as those predicted for p.Cys114Trp—are unusual but not unprecedented. For example, β-amino-acid enzyme variants G165M and E391K yielded theoretical ΔΔG values of approximately +54 and +43 kcal/mol, respectively, despite FoldX's standard error margins being only around ±0.85–1.7 kcal/mol (105,137). Extreme ΔΔG magnitudes have also been reported in the BRCA1 BRCT domain, in which FoldX predicted ΔΔG ≈ +15.2 kcal/mol for the p.G1788V variant (138). Classic distribution studies also top-bin FoldX ΔΔG >14 kcal/mol, indicating that such large predictions do occur, albeit rarely (139). These previous studies could support the idea that such high values are meaningful rather than artifacts. In another benchmark study, extreme ΔΔG values were attributed to steric clashes and "hard collisions" in the mutated model, particularly for bulky substitutions (140).

Cys114 was known to interact with Cys92 through a disulfide bridge. Disruption of this bridge via insertion of a bulky tryptophan may have been penalized more severely, leading to the extreme ΔΔG value. When taken together, all these previous studies suggested that the +44 kcal/mol prediction indicated a possible catastrophic structural disruption rather than a numerical anomaly. However, since these predictions are solely based on FoldX calculations, further validation through extended molecular dynamics simulations or advanced free-energy estimation approaches is required (122).

Building on these structural insights, the potential functional consequences of the observed destabilizing effects were examined to determine whether they translated into alterations in chondrocyte physiology. MTT-based measurements of cellular metabolic activity revealed a reduction in viability across all groups expressing either

wild-type or variant *CCN6* compared to the empty vector control, suggesting that elevated *CCN6* expression may impose a metabolic burden on chondrocytes. Consistent with this notion, transfection of increasing amounts of wild-type *CCN6* plasmid resulted in a dose-dependent decrease in metabolic activity, indicating that excessive WISP3 levels may impair chondrocyte function.

Although previous studies have reported conflicting outcomes for WISP3 variants, ranging from increased proliferation to reduced cell survival, our findings suggest that the observed decline in viability is primarily related to overall *CCN6* expression levels rather than variant-specific effects (61,108). These observations raise the possibility that overexpression of WISP3 could trigger a stress response in a cell type-dependent manner, particularly in metabolically demanding tissues such as cartilage. Such findings underscore the importance of investigating *CCN6* dosage sensitivity in the context of chondrocyte homeostasis and cartilage integrity (141).

Building on the metabolic findings, the potential influence of CCN6 variants on dynamic chondrocyte behaviors that are critical for maintaining cartilage structure, specifically migration and wound-healing capacity, was examined. The limited regenerative potential of cartilage and the essential role of extracellular matrix (ECM) homeostasis underscore the importance of these processes in preserving joint integrity. Previous studies have demonstrated that WISP3 suppresses the Wnt/β-catenin signaling pathway, thereby inhibiting chondrocyte migration (65,82). Consistent with these reports, overexpression of WISP3 was found to reduce chondrocyte motility, supporting its inhibitory function in migration control.

Variant-specific analyses revealed distinct migratory phenotypes. The truncated p.Tyr109* variant exhibited a migration pattern comparable to the control group, likely reflecting the absence of essential structural domains required for signaling, whereas the missense variants displayed greater wound closure than wild-type, indicating partial loss of inhibitory function. The nonsense variants, in contrast, failed to effectively inhibit Wnt/β-catenin signaling, consistent with the absence of a functional protein (142).

Because Wnt/β-catenin is known to regulate not only cell migration but also ECM remodeling, these findings prompted us to investigate whether the same pathway mediates WISP3-dependent control of matrix turnover. MMP-13 (collagenase-3), a principal enzyme responsible for type II collagen degradation, was assessed as a marker of matrix remodeling. Pro-MMP-13 levels were markedly reduced upon wild-type WISP3 overexpression, consistent with its suppressive effect on matrix degradation. Among the variants, p.Cys52*, which lacks a functional product, exhibited the highest pro-MMP-13 levels, whereas the other variants exerted stronger suppression than wild-type. These findings raise the possibility that excessive inhibition of MMP-13 may interfere with physiological matrix renewal. The consistent detection of only the inactive pro-form across all conditions suggests that these alterations occur primarily at the transcriptional level. In addition, the absence of MMP-2 and MMP-9 activity in zymography confirmed the non-inflammatory nature of the experimental setting. Under homeostatic conditions, MMP-13 transcription is mainly regulated by the Wnt/β-catenin and TGF-β/SMAD3 signaling pathways (16,82,143–145).

Although TGF-β/SMAD3 can influence MMP-13 expression, the suppression pattern observed here aligns more closely with altered β-catenin signaling. Given that both chondrocyte migration and MMP-13 expression were affected in a variant-dependent manner, our findings support a model in which WISP3 governs a coordinated migratory–matrix remodeling program through β-catenin modulation. While contributions from alternative pathways such as FAK and MAPK/ERK cannot be entirely excluded, the overall data identify Wnt/β-catenin as the principal mediator of WISP3-dependent functional outcomes in chondrocytes, linking cellular dynamics to matrix homeostasis (146,147).

In addition to modulating cell motility and matrix turnover, WISP3 also contributes to cartilage homeostasis by regulating chondrocyte adhesion to ECM components. In adhesion assays, cells expressing wild-type WISP3 exhibited markedly higher attachment to collagen-coated surfaces compared to control, suggesting that WISP3 enhances chondrocyte anchorage and stabilizes their

interaction with the ECM. In contrast, cells expressing nonsense variants displayed markedly reduced adhesion, likely reflecting the absence of the C-terminal Thrombospondin-1 (TSP-1) and C-terminal cystine knot (CTCK) domains, both of which mediate physical interactions with key ECM components, including collagens I–V, fibronectin, laminin, integrins, and heparan sulfate proteoglycans (148,149).

Thrombospondin-1 (TSP-1), one of the signature domains of WISP3, is a key matricellular component of the ECM. Rather than serving as a primary structural element, TSP-1 functions as a dynamic regulator of cellular behavior and ECM organization. Its core biological roles include promoting cell adhesion, guiding cell migration, and coordinating matrix assembly. Importantly, TSP-1 has been shown to bind directly to various fibrillar collagens, thereby influencing collagen fibrillogenesis, processing, and higher-order assembly within the cartilage matrix (150). Loss of this domain in truncated WISP3 forms could therefore weaken the molecular anchoring between chondrocytes and the surrounding ECM scaffold.

The reduced adhesion observed in cells expressing missense variants further indicates that even minor alterations within functional domains can compromise matrix engagement. This observation suggests that maintaining the overall structure of WISP3 alone may not be sufficient to preserve its adhesive function if domain-specific integrity, particularly within the TSP-1 and CTCK regions, is not retained. Collectively, these findings underscore the pivotal role of WISP3 in supporting effective chondrocyte–matrix interactions and highlight how domain-level disruptions can compromise cartilage stability and homeostasis.

Given that WISP3-mediated adhesion and matrix remodeling are tightly coupled to cellular stress responses, the potential influence of *CCN6* variants on mitochondrial redox balance was next examined. Reactive oxygen species (ROS) are critical regulators of chondrocyte homeostasis, and their excessive accumulation contributes to cartilage degeneration in several skeletal disorders (151). Reduced endogenous WISP3 expression has been linked to elevated cellular and mitochondrial ROS levels,

suggesting that loss of WISP3 function may disturb intracellular redox control. Moreover, previous reports have shown that nonsense variants induce substantially higher cellular ROS compared with wild-type WISP3 expression (14,15).

To assess the contribution of mitochondria to this imbalance, we quantified mitochondrial superoxide levels instead of total ROS, providing organelle-level specificity. Because increased ROS can arise either from oxidative stress or from elevated mitochondrial mass, we normalized ROS intensity to mitochondrial content to distinguish between these potential sources of ROS elevation. Following this normalization, the control, p.Gly83Glu, and p.Cys52* groups showed ROS/mass ratios comparable to baseline, indicating preserved redox balance. By contrast, cells expressing p.Tyr109* and p.Cys114Trp variants exhibited higher ROS/mass ratios, implying that these variants may interfere with redox homeostasis and enhance cellular stress.

Excessive mitochondrial ROS is known to damage organelle structures and gradually impair mitochondrial function, thereby disrupting overall cellular homeostasis (94). The trend toward higher ROS/mass in p.Tyr109* and p.Cys114Trp thus suggests variant-specific susceptibility to oxidative imbalance. By focusing on mitochondrial-targeted ROS rather than total intracellular levels, our approach provided higher spatial precision and revealed that *CCN6* variants differentially affect redox signaling within mitochondria. Future studies examining mitochondrial membrane potential ($\Delta\psi$), ATP production, mitochondrial network organization, and fusion/fission dynamics will be essential to determine whether the observed ROS/mass increase represents genuine mitochondrial dysfunction (112)s mitochondrial dysfunction is closely associated with endoplasmic reticulum (ER) stress, we examined whether *CCN6* variants alter ER homeostasis in chondrocytes. ER stress results from protein misfolding and triggers the unfolded protein response (UPR), a cellular adaptive pathway known to contribute to the development of several skeletal dysplasias, including chondrodysplasias (28,152,153). To evaluate the activation pattern of the UPR, we analyzed *CHOP* and spliced/unspliced XBP1 (*s/uXBP1*)

expression levels in chondrocytes expressing disease-associated WISP3 variants, which reflect the pro-apoptotic and adaptive branches of the pathway.

WISP3 variants modulated the pattern and intensity of the UPR in chondrocytes in a variant-specific manner. The missense variants p.Gly83Glu and p.Cys114Trp were associated with increased *s/uXBP1* expression, indicating activation of adaptive signaling. However, the p.Cys114Trp variant also caused a pronounced elevation in *CHOP* levels, suggesting simultaneous engagement of both adaptive and pro-apoptotic branches of the UPR. In contrast, the nonsense variant p.Tyr109* displayed high *CHOP* expression, pointing to a predominantly pro-apoptotic response. This distinction was further supported by analysis of the *CHOP/sXBP1* ratio: while the ratio remained below 1 in the missense variants, consistent with an adaptive response, it was markedly elevated in p.Tyr109*, reflecting insufficient compensatory activation and a shift toward apoptosis. This trend implies that misfolded but partially functional missense proteins can still initiate adaptive mechanisms, whereas truncated products generated by premature termination codons are unable to maintain this capacity, thereby enhancing pro-apoptotic signaling. Increased *CHOP* expression has previously been linked not only to sustained ER stress but also to mitochondrial dysfunction (152). The elevated *CHOP* levels observed in both p.Tyr109* and p.Cys114Trp suggest that ER stress in these variants may be associated with secondary mitochondrial dysfunction.

The potential effect of disease-associated variants on the subcellular distribution of WISP3 was examined. Confocal co-localization analysis was performed using TOM20 as a mitochondrial marker. Consistent with previous observations reporting partial mitochondrial localization of WISP3 in human chondrocytes, wild-type WISP3 showed measurable overlap with the mitochondrial network. In contrast, the p.Cys52* variant, which does not produce detectable protein, exhibited markedly reduced WISP3 signal and low Pearson correlation coefficients (14). Although the Manders M2 coefficient appeared elevated, this most likely reflected background fluorescence rather than genuine spatial overlap.

Cells expressing p.Tyr109* and p.Cys114Trp variants exhibited stronger mitochondrial association compared with wild-type, indicating aberrant retention and intracellular redistribution of WISP3. Such accumulation within or adjacent to mitochondria is expected to disturb mitochondrial protein quality control and reduce the organelle's ability to manage nascent or misfolded proteins. Mislocalized proteins within mitochondria are known to stimulate ROS formation, thereby reinforcing oxidative stress and activating the UPR (154). This link aligns with the increased mitochondrial superoxide levels and ER stress marker expression observed in these variants, suggesting that WISP3 mislocalization contributes to mitochondrial dysfunction. In contrast, the p.Gly83Glu variant displayed a localization pattern similar to that of wild-type WISP3, without any apparent enrichment in the mitochondrial region. This observation suggests that the p.Gly83Glu substitution exerts a milder structural effect, sufficient to preserve WISP3 localization and maintain near-normal mitochondrial association.

Overall, these cellular and molecular findings converge into a coherent model linking WISP3 dysfunction with impaired coordination between endoplasmic reticulum and mitochondrial stress responses. Collectively, the data demonstrate that WISP3 variants alter redox balance, ER stress signaling, and intracellular distribution in a variant-dependent manner. The p.Tyr109* and p.Cys114Trp variants appear to disrupt ER–mitochondrial communication and compromise chondrocyte homeostasis through increased mitochondrial superoxide production, activation of the unfolded protein response, and excessive mitochondrial accumulation. In contrast, the p.Cys52* variant showed minimal cellular effects, likely reflecting complete loss of function due to the absence of detectable protein. Overall, this integrative analysis emphasizes the essential role of WISP3 in maintaining intracellular stress equilibrium and highlights its contribution to the pathogenesis of PPD.

Considering the observed ER stress responses, transcriptional programs were examined to assess differences among chondrocytes expressing wild-type or disease-associated WISP3 variants. Transcriptomic profiling of chondrocytes expressing either the p.Cys52* or p.Cys114Trp variant revealed pronounced yet qualitatively distinct

gene expression alterations compared to wild-type WISP3 overexpression. In both cases, downregulated genes outnumbered upregulated ones, with 1.76- and 1.78-fold differences respectively, suggesting an overarching trend toward transcriptional repression. However, enrichment analysis underscored that the nature of these transcriptional changes was highly variant-specific. Wild-type WISP3 overexpression promoted the expression of genes involved in cytoskeletal regulation and ER-directed protein transport. These pathways appeared markedly suppressed under variant conditions, indicating impaired structural and trafficking functions of WISP3 in a variant-dependent manner (Figure 25E).

The p.Cys114Trp variant triggered a broad transcriptional activation of genes associated with ER stress, the UPR, and programmed cell death. Upregulated transcripts included *HSPA5* and *DNAJB9*, key ER chaperones involved in misfolded protein recognition, as well as *HERPUD1*, which facilitates clearance via ER-associated degradation (ERAD) (155–157). Pro-apoptotic transcription factors *DDIT3* (*CHOP*) and *ATF3* were also elevated under this condition (158,159). In addition, *PLCG2*, implicated in calcium signaling and ROS production, may contribute to ER–mitochondria stress signaling while *KLF4* participates in adaptive stress responses, cellular differentiation, and redox balance (160,161). The collective induction of these transcripts supports the notion that p.Cys114Trp initiates a coordinated stress response extending beyond ER proteostasis to mitochondrial redox homeostasis. This interpretation is consistent with our prior observation of elevated mitochondrial ROS in cells expressing the same variant.

Conversely, the p.Cys52* variant elicited a much narrower transcriptional response. Among the heatmap-highlighted genes, only *CSNK1A1L*, *ANP32CP*, and *NME2P1* were upregulated. CSNK1A1L has been linked to Wnt signaling repression, whereas *ANP32CP* is associated with apoptotic regulation and nucleocytoplasmic transport (162,163). *NME2P1*, a predicted pseudogene, has been implicated in apoptosis regulation (164). These genes were consistently elevated in both variant conditions but absent in the wild-type expression profile, indicating a shared transcriptomic pattern across disease-associated variants. The gene-to-pathway

associations illustrated in the heatmap provide a clear depiction of overlapping biological functions. In p.Cys114Trp-expressing cells, multiple transcripts were linked to more than one functional category, suggesting that the variant induces coordinated disruptions across interconnected regulatory networks rather than isolated pathways.

This integrative disruption appears to manifest as a broad cellular stress response involving ER dysfunction and redox imbalance, potentially compromising chondrocyte viability. In contrast, the p.Cys52* variant, which does not yield a stable protein product, induced a markedly narrower transcriptional response and failed to activate canonical stress pathways. The consistent upregulation of select apoptosis-related transcripts suggests that limited secondary effects may still occur in the absence of WISP3 protein, while activation of adaptive or pro-apoptotic signaling pathways remained minimal. These divergent profiles highlight distinct pathological mechanisms: one marked by extensive stress engagement, the other shaped by the consequences of protein absence. Loss of ER localization and cytoskeletal regulatory capacity emerges as a shared outcome across both variants. While wild-type WISP3 maintains these essential cellular functions, pathogenic variants compromise them, leading to variant-dependent downstream effects. In the case of p.Cys114Trp, partial retention and accumulation within the ER appear to initiate a coordinated stress response involving ER–mitochondrial signaling and cell death pathways. By comparison, the truncated p.Cys52* variant exerts its impact through a markedly attenuated transcriptional profile, reflecting functional deficiency without active stress induction. These findings underscore the multifaceted role of WISP3 in chondrocytes and demonstrate how distinct molecular alterations result in divergent transcriptional and cellular phenotypes.

Building upon the transcriptomic findings, the first comprehensive proteomic analysis of WISP3 in human chondrocytes was conducted. Proteomic mapping was performed to identify intracellular interaction partners of WISP3 and to assess how disease-associated variants alter its interaction profile. The full-length wild-type protein was compared with the structurally destabilized missense variant p.Cys114Trp and the truncated isoform p.Tyr109*, which, despite harboring a premature

termination codon (PTC), remains translationally expressed. Comparative analysis revealed markedly distinct effects of the two variants on the WISP3 interactome. The truncated p.Tyr109* isoform exhibited a pronounced reduction in both the number and diversity of interactors, underscoring the essential contribution of WISP3's C-terminal domains to protein–protein interactions and network stability. In contrast, the structurally unstable p.Cys114Trp variant showed an expanded range of interactions compared with wild-type, possibly reflecting compensatory or aberrant binding events arising from altered conformation or subcellular distribution. Together, these findings reveal that structural perturbations in WISP3 redefine its molecular connectivity and contribute to variant-specific pathogenic mechanisms.

Across both transcriptomic and proteomic datasets, several cytoskeletal proteins—ACTBM, TUBB1A, TUBB2A, TUBB2B, POTEF, and POTEI—were consistently identified as WISP3-associated partners. The beta-tubulin isoforms contribute to microtubule organization, while POTEF and POTEI are implicated in ATP/protein/nucleotide binding and cytoskeletal regulation (165). ACTBM, a beta-actin isoform, supports cell shape, motility, and mechanical stability. Phylogenetic analysis places POTEF and POTEI in close evolutionary proximity to ACTBM, suggesting functional convergence (166,167). Downregulation of ACTBM transcripts in variant-expressing cells implies that WISP3 disruption may compromise actin dynamics. The stable detection of these proteins across all isoforms indicates that WISP3 engages a conserved cytoskeletal module, representing a shared molecular signature that may contribute to chondrocyte dysfunction in PPD.

Among the variant-dependent differences, LIM domain and actin-binding protein 1 (LIMA1), which stabilizes cell–cell adhesion and connects E-cadherin–catenin complexes to actin filaments, was detected in the wild-type WISP3 interactome (166,167). This observation suggests that functional WISP3 is required to maintain LIMA1 expression and the integrity of adhesion complexes. Loss of this interaction could trigger cytoskeletal remodeling and activate β-catenin signaling, potentially promoting mesenchymal transitions. In the context of WISP3 dysfunction, reduced

LIMA1 levels may therefore weaken adhesion strength and exacerbate cytoskeletal disorganization, leading to impaired cartilage stability.

Calmodulin (CALM), a central calcium-binding protein involved in chondrogenesis and intracellular signaling (168,169), was identified only in cells expressing full-length WISP3 (wild-type and p.Cys114Trp) and was absent in p.Tyr109* variant. In humans, calmodulin is encoded by three distinct genes (*CALM1*, *CALM2*, and *CALM3*) that produce an identical protein under differential transcriptional control, allowing spatial and temporal regulation of expression. This indicates that the full structural integrity of WISP3 is required to sustain Ca^{2+}–calmodulin interactions. Given that WISP3-deficient chondrocytes display elevated mitochondrial Ca^{2+} levels, the absence of calmodulin interaction in truncation variants may reflect a loss of buffering capacity, aggravating mitochondrial stress(14,159) Impaired calmodulin signaling could further disturb differentiation, matrix homeostasis, and signaling, emphasizing WISP3's potential role as both a structural regulator and a modulator of intracellular calcium balance and mitochondrial stability.

Cytoskeleton-associated protein 4 (CKAP4) was identified as a key interactor of WISP3, serving multiple cellular functions in both ER homeostasis and signaling regulation.CKAP4 contributes to the selective autophagic clearance of damaged ER fragments (ER-phagy) through coordination with the autophagosome system, thereby preventing the accumulation of misfolded proteins and maintaining proteostatic balance under stress conditions (170). It also forms a functional complex with DKK1, establishing the DKK1–CKAP4–LRP6 axis that suppresses Wnt signaling while activating the PI3K/AKT pathway (171). WISP3 has previously been reported to interact with LRP6 and Frizzled receptors, thereby modulating Wnt and BMP signaling (82). In our study, we identified a previously unrecognized interaction between full-length WISP3 (wild-type and p.Cys114Trp variant) and CKAP4, suggesting that WISP3 may integrate into the DKK1–CKAP4–LRP6–Frizzled signaling network. Increased CKAP4 association in cells expressing p.Cys114Trp likely reflects a compensatory attempt to restore ER proteostasis; however, the structural instability of the variant appears to limit this response, resulting in sustained

ER stress and mitochondrial dysfunction (172). We propose that disruption of this signaling complex may disturb the balance between Wnt suppression and PI3K/AKT activation, thereby weakening the overall stress adaptation capacity. Collectively, our findings highlight WISP3 as a potential regulator of ER–mitochondrial crosstalk through CKAP4-mediated pathways, emphasizing its contribution to coordinated cellular stress adaptation mechanisms.

Proteomic mapping also revealed the exclusive interaction of p.Cys114Trp with the RNA helicases DDX5 and DDX17, both of which play key roles in transcriptional regulation, alternative splicing, and ribonucleoprotein complex remodeling (173,174). DDX5 is also known to regulate ER stress and autophagy, while both helicases modulate Wnt/β-catenin signaling. Their selective association with p.Cys114Trp may result from variant-induced structural destabilization, allowing aberrant binding and sequestration from native RNA substrates. Such misinteraction could disturb RNA processing and transcriptional regulation, contributing to the enhanced stress responses observed in this variant.

Another variant-specific interactor was HSPB1, a small heat-shock protein detected only in complexes formed with p.Cys114Trp. HSPB1 binds misfolded proteins, prevents aggregation, and alleviates proteotoxic stress (175). Beyond its canonical chaperone function, it stabilizes actin filaments, reduces oxidative damage, and inhibits mitochondrial apoptosis by preventing cytochrome c release (176). These cytoprotective roles are essential for cartilage maintenance, where decreased HSPB1 levels have been associated with enhanced chondrocyte apoptosis in osteoarthritis (177). Its selective association with p.Cys114Trp likely reflects a compensatory response to increased proteostatic burden, consistent with the transcriptomic upregulation of DNAJB9, an ER co-chaperone promoting misfolded-protein degradation via the ERAD pathway. Together, these observations suggest that p.Cys114Trp imposes a dual burden on protein quality control by engaging both cytoplasmic and ER-localized chaperone systems, which may eventually fail under stress and lead to progressive chondrocyte loss and cartilage degeneration in PPD.

In summary, the findings demonstrate that the absence of WISP3 or the expression of structurally unstable variants can disrupt chondrocyte function through distinct yet converging mechanisms, ultimately contributing to the pathogenesis of PPD. While the specific mode of disruption varies, ranging from complete protein loss to the accumulation of misfolded or unstable forms, the resulting cellular consequences converge on shared downstream pathways. Rather than acting through a single molecular axis, WISP3 functions as a multifaceted regulator that integrates intracellular homeostasis, skeletal organization, and cytoskeletal stability. This interpretation aligns with its extensive interactome and its proposed role as a ligand mediating autocrine and paracrine signaling, which may explain how diverse molecular alterations give rise to overlapping clinical features. Given that PPD is a rare disorder typically diagnosed in late childhood, variant-specific molecular differences may be more pronounced during early disease stages; however, as cartilage deterioration advances, these differences likely converge, resulting in similar clinical outcomes. The observed alterations implicate dysregulation of the Wnt/β-catenin pathway as a central mechanism, providing new insight into the complexity of WISP3-mediated regulatory networks. Understanding these variant-dependent mechanisms may help guide the development of targeted therapeutic strategies applicable at earlier disease stages.

Despite the comprehensive scope of this study, several limitations must be acknowledged. The number of biological replicates in RNA-seq and LC–MS/MS analyses was limited due to resource constraints, reducing statistical robustness. Moreover, reliance on an overexpression model may not fully represent physiological expression levels or context-specific regulation. Future research employing CRISPR/Cas9-engineered cell lines, 3-D chondrogenic organoids, and *in vivo* validation will be critical to confirm these findings. While access to patient-derived chondrocytes remains technically challenging, such models would provide valuable translational insights. Nevertheless, by integrating structural modeling, functional assays, and multi-omics profiling, we have established a coherent framework that captures complementary aspects of WISP3 dysfunction. This integrated approach enables a deeper understanding of how distinct variants alter cellular stress responses,

redox balance, and extracellular matrix organization. Collectively, our work provides a mechanistic foundation for future investigations and contributes to the growing understanding of how molecular disruptions in WISP3 underlie skeletal disease pathology.

6 CONCLUSION

This study aimed to elucidate the functional consequences of disease-associated *CCN6* variants in Progressive Pseudorheumatoid Dysplasia (PPD) and to determine how these alterations affect chondrocyte homeostasis. Through an integrative strategy combining molecular, transcriptomic, and proteomic analyses, the research objectives were successfully achieved. The results revealed that WISP3 dysfunction occurs through both loss- and gain-of-function mechanisms. Variants p.Cys52* and p.Tyr109* resulted in absent or truncated proteins with severely reduced interaction capacity, consistent with classical loss-of-function effects. In contrast, p.Cys114Trp produced a structurally unstable full-length protein associated with misfolded-protein accumulation, ER stress, and aberrant signaling activation, supporting a gain-of-function model. Meanwhile, p.Gly83Glu led to only mild alterations in chondrocyte behavior, confirming its limited functional impact within the WISP3 network.

The data presented in this study deepen our understanding of how WISP3 contributes to cartilage integrity by maintaining ER homeostasis, modulating cytoskeletal organization, and sustaining redox maintenance. Distinct molecular disruptions, either due to protein loss or structural instability, appear to converge on shared downstream mechanisms affecting chondrocyte survival and ECM regulation. The integration of structural modeling, functional assays, and multi-omics profiling established a coherent and multidimensional framework for evaluating the pathogenicity of uncertain variants in skeletal diseases. This framework not only clarifies the molecular basis of PPD but also offers a model for investigating other cartilage-related disorders linked to matrix and signaling imbalance.

Future research should extend these investigations to other domains of WISP3 and to additional *CCN6* variants that remain uncharacterized, as their contribution to disease heterogeneity is not yet fully understood. Such studies will be crucial for establishing a more complete genotype–phenotype map and identifying molecular checkpoints that can be targeted therapeutically. Ultimately, this work represents an initial step toward a mechanistic and variant-specific understanding of PPD, providing

the conceptual basis for designing therapeutic strategies aimed at restoring WISP3 function and maintaining cartilage homeostasis.

7 REFERENCES

1. Ye J. Patients with progressive pseudorheumatoid dysplasia: From clinical diagnosis to molecular studies. Mol Med Rep. 2011 Oct 11;
2. Huang W, Martin EE, Burman B, Gonzalez ME, Kleer CG. The matricellular protein CCN6 (WISP3) decreases Notch1 and suppresses breast cancer initiating cells. Oncotarget. 2016 May 3;7(18):25180–93.
3. Garcia Segarra N, Mittaz L, Campos-Xavier AB, Bartels CF, Tuysuz B, Alanay Y, et al. The diagnostic challenge of progressive pseudorheumatoid dysplasia (PPRD): A review of clinical features, radiographic features, and *WISP3* mutations in 63 affected individuals. Am J Med Genet C Semin Med Genet. 2012 Aug 15;160C(3):217–29.
4. Liu Z, Chen X. Progressive pseudorheumatoid dysplasia: a case series report. Transl Pediatr. 2021 Jul;10(7):1932–9.
5. Omar AA, Ahmed S, Rodrigues JC, Kayiza A, Owino L. Progressive pseudorheumatoid dysplasia misdiagnosed as juvenile idiopathic arthritis: a case report. J Med Case Rep. 2021 Dec 8;15(1):551.
6. Bhavani GS, Shah H, Shukla A, Dalal A, Girisha KM. Progressive Pseudorheumatoid Dysplasia. 1993.
7. Chen PC, Cheng HC, Yang SF, Lin CW, Tang CH. The CCN Family Proteins: Modulators of Bone Development and Novel Targets in Bone-Associated Tumors. Biomed Res Int. 2014;2014:1–11.
8. Perbal B. CCN proteins: multifunctional signalling regulators. The Lancet. 2004 Jan;363(9402):62–4.
9. Jun JI, Lau LF. Taking aim at the extracellular matrix: CCN proteins as emerging therapeutic targets. Nat Rev Drug Discov. 2011 Dec 1;10(12):945–63.
10. Holbourn KP, Acharya KR, Perbal B. The CCN family of proteins: structure–function relationships. Trends Biochem Sci. 2008 Oct;33(10):461–73.
11. Yao Q, Wu X, Tao C, Gong W, Chen M, Qu M, et al. Osteoarthritis: pathogenic signaling pathways and therapeutic targets. Signal Transduct Target Ther. 2023 Feb 3;8(1):56.
12. Li X, Han Y, Li G, Zhang Y, Wang J, Feng C. Role of Wnt signaling pathway in joint development and cartilage degeneration. Front Cell Dev Biol. 2023;11:1181619.
13. Sen M, Cheng Y, Goldring MB, Lotz MK, Carson DA. WISP3-dependent regulation of type II collagen and aggrecan production in chondrocytes. Arthritis Rheum. 2004 Feb 5;50(2):488–97.
14. Patra M, Mahata SK, Padhan DK, Sen M. CCN6 regulates mitochondrial function. J Cell Sci. 2016 Jul 15;129(14):2841–51.
15. Miller DS, Sen M. Potential role of WISP3 (CCN6) in regulating the accumulation of reactive oxygen species. Biochem Biophys Res Commun. 2007 Mar;355(1):156–61.

16. Karalexi MA, Papadopoulou A, Papakonstantinou O, Mitrogiorgou M, Skarantavos G, Papaevangelou V, et al. Late Diagnosis of Progressive Pseudorheumatoid Dysplasia in an Adolescent Patient: A Case Report and Review of the Literature. The Journal of Pediatric Research. 2021 May 25;8(2):209–13.
17. Delague V, Chouery E, Corbani S, Ghanem I, Aamar S, Fischer J, et al. Molecular study of *WISP3* in nine families originating from the Middle-East and presenting with progressive pseudorheumatoid dysplasia: Identification of two novel mutations, and description of a founder effect. Am J Med Genet A. 2005 Oct 8;138A(2):118–26.
18. Panda A. Skeletal dysplasias: A radiographic approach and review of common non-lethal skeletal dysplasias. World J Radiol. 2014;6(10):808.
19. Krakow D, Rimoin DL. The skeletal dysplasias. Genetics in Medicine. 2010 Jun;12(6):327–41.
20. Warman ML, Cormier-Daire V, Hall C, Krakow D, Lachman R, LeMerrer M, et al. Nosology and classification of genetic skeletal disorders: 2010 revision. Am J Med Genet A. 2011 May 15;155(5):943–68.
21. Alam Z, Syed MU, Siddiqui TA, Gunturi A, Reddy B, Alam Z, et al. Spinal lesions: a comprehensive radiologic overview. Frontiers in Radiology. 2025 Jun 27;5.
22. Geister KA, Camper SA. Advances in Skeletal Dysplasia Genetics. Annu Rev Genomics Hum Genet. 2015 Aug 24;16(1):199–227.
23. Ikegawa S. Genetic analysis of skeletal dysplasia: recent advances and perspectives in the post-genome-sequence era. J Hum Genet. 2006 Jul 3;51(7):581–6.
24. Krakow D. Skeletal Dysplasias. Clin Perinatol. 2015 Jun;42(2):301–19.
25. Neben CL, Merrill AE. Signaling Pathways in Craniofacial Development. In 2015. p. 493–542.
26. Wu M, Chen G, Li YP. TGF-β and BMP signaling in osteoblast, skeletal development, and bone formation, homeostasis and disease. Bone Res. 2016;4:16009.
27. Guasto A, Cormier-Daire V. Signaling Pathways in Bone Development and Their Related Skeletal Dysplasia. Int J Mol Sci. 2021 Apr 21;22(9):4321.
28. Kimura M, Ichimura S, Sasaki K, Masuya H, Suzuki T, Wakana S, et al. Endoplasmic reticulum stress-mediated apoptosis contributes to a skeletal dysplasia resembling platyspondylic lethal skeletal dysplasia, Torrance type, in a novel Col2a1 mutant mouse line. Biochem Biophys Res Commun. 2015 Dec;468(1–2):86–91.
29. Giusti V, Scotlandi K. CCN proteins in the musculoskeletal system: current understanding and challenges in physiology and pathology. J Cell Commun Signal. 2021 Dec 6;15(4):545–66.
30. Alawbathani S, Kawalia A, Karakaya M, Altmüller J, Nürnberg P, Cirak S. Late diagnosis of a truncating *WISP3* mutation entails a severe phenotype of progressive pseudorheumatoid dysplasia. Molecular Case Studies. 2018 Feb;4(1):a002139.
31. Dalal A, Bhavani G SL, Togarrati PP, Bierhals T, Nandineni MR, Danda S, et al. Analysis of the *WISP3* gene in Indian families with progressive pseudorheumatoid dysplasia. Am J Med Genet A. 2012 Nov 17;158A(11):2820–8.

32. Gupta A, Bagri N, Chandola S, Jana M. Case 316: Progressive Pseudorheumatoid Dysplasia. Radiology. 2023 Aug 1;308(2).
33. Kılıç G. An Unusual Coexistence of Progressive Pseudorheumatoid Dysplasia and Relapsing Polychondritis. Arch Rheumatol. 2016 Aug 17;31(3):290–4.
34. Ye J. Patients with progressive pseudorheumatoid dysplasia: From clinical diagnosis to molecular studies. Mol Med Rep. 2011 Oct 11;
35. Alkhaldi Z, Allawati M, Alhashmi N. Progressive pseudorheumatoid dysplasia in an Omani family: a case report. Journal of Biochemical and Clinical Genetics. 2023 Jun 30;6(1):85–8.
36. Gaboon NEA, Parveen A, El Beheiry A, Al-Aama JY, Alsaedi MS, Wasif N. A Novel Homozygous Frameshift Mutation in CCN6 Causing Progressive Pseudorheumatoid Dysplasia (PPRD) in a Consanguineous Yemeni Family. Front Pediatr. 2019 Jun 25;7.
37. Chouery E, Corbani S, Dahmen J, Zouari L, Gribaa M, Leban N, et al. Progressive pseudorheumatoid dysplasia in North and West Africa: Clinical description in ten patients with mutations of WISP3. Egyptian Journal of Medical Human Genetics. 2017 Jul;18(3):299–303.
38. Torreggiani S, Torcoletti M, Campos-Xavier B, Baldo F, Agostoni C, Superti-Furga A, et al. Progressive pseudorheumatoid dysplasia: a rare childhood disease. Rheumatol Int. 2019 Mar 16;39(3):441–52.
39. Giray E. Progressive pseudorheumotoid dysplasia: A presentation of four cases with slow and rapid progression and effects of early rehabilitation program. Turk J Phys Med Rehabil. 2019 Sep 2;65(3):290–7.
40. Sailani MR, Chappell J, Jingga I, Narasimha A, Zia A, Lynch JL, et al. *WISP3* mutation associated with pseudorheumatoid dysplasia. Molecular Case Studies. 2018 Feb;4(1):a001990.
41. Wynne-Davies R, Hall C, Ansell B. Spondylo-epiphysial dysplasia tarda with progressive arthropathy. A “new” disorder of autosomal recessive inheritance. J Bone Joint Surg Br. 1982 Aug;64-B(4):442–5.
42. Hurvitz JR, Suwairi WM, Van Hul W, El-Shanti H, Superti-Furga A, Roudier J, et al. Mutations in the CCN gene family member WISP3 cause progressive pseudorheumatoid dysplasia. Nat Genet. 1999 Sep;23(1):94–8.
43. Malik AR, Liszewska E, Jaworski J. Matricellular proteins of the Cyr61/CTGF/NOV (CCN) family and the nervous system. Front Cell Neurosci. 2015 Jun 24;9.
44. McKusick VA, Hartz PA. OMIM: Cellular Communication Network Factor 6; CCN6 [Internet]. 2021 [cited 2025 Aug 23]. Available from: https://www.omim.org/entry/603400
45. GTEx Analysis Release V10 dbGaP accession phs000424. v10. p2. CCN6 - GTEx Portal [Internet]. [cited 2025 Nov 5]. Available from: https://gtexportal.org/home/gene/CCN6/exonExpressionTab
46. Neerinckx B, Thues C, Wouters C, Lechner S, Westhovens R, Van Esch H. A homozygous deletion of exon 1 in WISP3 causes progressive pseudorheumatoid dysplasia in two siblings. Hum Genome Var. 2015 Dec 3;2(1):15049.

47. Chen CC, Lau LF. Functions and mechanisms of action of CCN matricellular proteins. Int J Biochem Cell Biol. 2009 Apr;41(4):771–83.
48. Rachfal AW, Brigstock DR. Structural and Functional Properties of CCN Proteins. In 2005. p. 69–103.
49. Bornstein P. EXTRACELLULAR MATRIX | Matricellular Proteins. In: Encyclopedia of Respiratory Medicine. Elsevier; 2006. p. 175–83.
50. Kim H, Son S, Shin I. Role of the CCN protein family in cancer. BMB Rep. 2018 Oct 31;51(10):486–92.
51. Chen PC, Cheng HC, Yang SF, Lin CW, Tang CH. The CCN Family Proteins: Modulators of Bone Development and Novel Targets in Bone-Associated Tumors. Biomed Res Int. 2014;2014:1–11.
52. Leask A. A sticky situation: CCN1 promotes both proliferation and apoptosis of cancer cells. J Cell Commun Signal. 2010 Mar 16;4(1):71–2.
53. Quan T, Shao Y, Purohit T, Jiang Y, Qin Z, Fisher GJ, et al. CCN2 functions as a modulator of cell cycle regulation in human dermal fibroblasts. J Cell Commun Signal. 2025 Mar;19(1).
54. Lu W, McCallum L, Perbal B, Lazar N, Irvine A. CCN3, a Novel Growth Inhibitory Factor for Chronic Myeloid Leukemia. Blood. 2008 Nov 16;112(11):4230–4230.
55. Chen CC, Lau LF. Functions and mechanisms of action of CCN matricellular proteins. Int J Biochem Cell Biol. 2009 Apr;41(4):771–83.
56. Holbourn KP, Perbal B, Ravi Acharya K. Proteins on the catwalk: modelling the structural domains of the CCN family of proteins. J Cell Commun Signal. 2009 Mar 8;3(1):25–41.
57. Arnott JA, Doane K, Planey SL. CCN Family: Matricellular Proteins in Cartilage and Bone Development. In: Composition and Function of the Extracellular Matrix in the Human Body. InTech; 2016.
58. UniProt- WISP3 Protein [Internet]. 2025 [cited 2025 Nov 8]. Available from: https://www.uniprot.org/uniprotkb/O95389/entry
59. Guerriero CJ, Brodsky JL. The delicate balance between secreted protein folding and endoplasmic reticulum-associated degradation in human physiology. Physiol Rev. 2012 Apr;92(2):537–76.
60. Wu J, Chen Y. Signal peptide stabilizes folding and inhibits misfolding of serum amyloid A. Protein Science. 2022 Dec 16;31(12).
61. Wang M, Man XF, Liu YQ, Liao EY, Shen ZF, Luo XH, et al. Dysfunction of Collagen Synthesis and Secretion in Chondrocytes Induced by *Wisp3* Mutation. Int J Endocrinol. 2013;2013:1–9.
62. Rao RS, Patra M, Sen M. WISP3 - IGF1 interaction regulates chondrocyte hypertrophy. J Cell Sci. 2013 Jan 1;

63. Madhuri V, Santhanam M, Rajagopal K, Sugumar LK, Balaji V. *WISP3* mutational analysis in Indian patients diagnosed with progressive pseudorheumatoid dysplasia and report of a novel mutation at p.Y198*. Bone Joint Res. 2016 Jul;5(7):301–6.
64. Baker N, Sharpe P, Culley K, Otero M, Bevan D, Newham P, et al. Dual regulation of metalloproteinase expression in chondrocytes by Wnt-1-inducible signaling pathway protein 3/CCN6. Arthritis Rheum. 2012 Jul;64(7):2289–99.
65. Gao H, Yin FF, Guan DX, Feng YX, Zheng QW, Wang X, et al. Liver cancer: WISP3 suppresses hepatocellular carcinoma progression by negative regulation of β-catenin/TCF/LEF signalling. Cell Prolif. 2019 May;52(3):e12583.
66. Nam MW, Lee HK, Kim CW, Choi Y, Ahn D, Go RE, et al. Effects of CCN6 overexpression on the cell motility and activation of p38/bone morphogenetic protein signaling pathways in pancreatic cancer cells. Biomedicine & Pharmacotherapy. 2023 Jul;163:114780.
67. Becerra J, Andrades JA, Guerado E, Zamora-Navas P, López-Puertas JM, Reddi AH. Articular Cartilage: Structure and Regeneration. Tissue Eng Part B Rev. 2010 Dec;16(6):617–27.
68. Sophia Fox AJ, Bedi A, Rodeo SA. The Basic Science of Articular Cartilage: Structure, Composition, and Function. Sports Health: A Multidisciplinary Approach. 2009 Nov 2;1(6):461–8.
69. Hall BK. Vertebrate Cartilages. In: Bones and Cartilage. Elsevier; 2015. p. 43–59.
70. Sussman WI, Pitts J, Williams C. Introduction to Interventional Orthopedics and Review of the Pathophysiology of Orthopedic Conditions. In: Atlas of Interventional Orthopedics Procedures. Elsevier; 2022. p. 1–13.
71. Li X, Sheng S, Li G, Hu Y, Zhou F, Geng Z, et al. Research Progress in Hydrogels for Cartilage Organoids. Adv Healthc Mater. 2024 Sep 27;13(22).
72. ur Rehman S, Iqbal S, Umair Shahid M, Soman Jahangir M, Latif Malik A. Cartilage: Structure, Function, and the Pathogenesis of Osteoarthritis. In: Advancements in Synovial Joint Science - Structure, Function, and Beyond. IntechOpen; 2024.
73. Berdiaki A, Neagu M, Tzanakakis P, Spyridaki I, Pérez S, Nikitovic D. Extracellular Matrix Components and Mechanosensing Pathways in Health and Disease. Biomolecules. 2024 Sep 20;14(9).
74. Bačenková D, Trebuňová M, Demeterová J, Živčák J. Human Chondrocytes, Metabolism of Articular Cartilage, and Strategies for Application to Tissue Engineering. Int J Mol Sci. 2023 Dec 4;24(23):17096.
75. Komiya Y, Habas R. Wnt signal transduction pathways. Organogenesis. 2008 Apr;4(2):68–75.
76. Usami Y, Gunawardena AT, Iwamoto M, Enomoto-Iwamoto M. Wnt signaling in cartilage development and diseases: lessons from animal studies. Laboratory Investigation. 2016 Feb;96(2):186–96.
77. Chen H, Tan XN, Hu S, Liu RQ, Peng LH, Li YM, et al. Molecular Mechanisms of Chondrocyte Proliferation and Differentiation. Front Cell Dev Biol. 2021 May 28;9.

78. Xue C, Chu Q, Shi Q, Zeng Y, Lu J, Li L. Wnt signaling pathways in biology and disease: mechanisms and therapeutic advances. Signal Transduct Target Ther. 2025 Apr 4;10(1):106.
79. Rim EY, Clevers H, Nusse R. The Wnt Pathway: From Signaling Mechanisms to Synthetic Modulators. Annu Rev Biochem. 2022 Jun 21;91:571–98.
80. Liu J, Xiao Q, Xiao J, Niu C, Li Y, Zhang X, et al. Wnt/β-catenin signalling: function, biological mechanisms, and therapeutic opportunities. Signal Transduct Target Ther. 2022 Jan 3;7(1):3.
81. Held A, Glas A, Dietrich L, Bollmann M, Brandstädter K, Grossmann TN, et al. Targeting β-catenin dependent Wnt signaling via peptidomimetic inhibitors in murine chondrocytes and OA cartilage. Osteoarthritis Cartilage. 2018 Jun;26(6):818–23.
82. Nakamura Y, Weidinger G, Liang JO, Aquilina-Beck A, Tamai K, Moon RT, et al. The CCN family member Wisp3, mutant in progressive pseudorheumatoid dysplasia, modulates BMP and Wnt signaling. Journal of Clinical Investigation. 2007 Oct 1;117(10):3075–86.
83. Thielen N, van der Kraan P, van Caam A. TGFβ/BMP Signaling Pathway in Cartilage Homeostasis. Cells. 2019 Aug 24;8(9):969.
84. Costantini A, Guasto A, Cormier-Daire V. TGF-β and BMP Signaling Pathways in Skeletal Dysplasia with Short and Tall Stature. Annu Rev Genomics Hum Genet. 2023 Aug 25;24(1):225–53.
85. van der Kraan PM, Blaney Davidson EN, van den Berg WB. Bone Morphogenetic Proteins and articular cartilage. Osteoarthritis Cartilage. 2010 Jun;18(6):735–41.
86. Wu M, Wu S, Chen W, Li YP. The roles and regulatory mechanisms of TGF-β and BMP signaling in bone and cartilage development, homeostasis and disease. Cell Res. 2024 Jan 24;34(2):101–23.
87. Lu Y, Zhou J, Wang H, Gao H, Ning E, Shao Z, et al. Endoplasmic reticulum stress-mediated apoptosis and autophagy in osteoarthritis: From molecular mechanisms to therapeutic applications. Cell Stress Chaperones. 2024 Dec;29(6):805–30.
88. Hetz C. The unfolded protein response: controlling cell fate decisions under ER stress and beyond. Nat Rev Mol Cell Biol. 2012 Feb 18;13(2):89–102.
89. Hetz C, Zhang K, Kaufman RJ. Mechanisms, regulation and functions of the unfolded protein response. Nat Rev Mol Cell Biol. 2020 Aug 26;21(8):421–38.
90. Huang W, Gong Y, Yan L. ER Stress, the Unfolded Protein Response and Osteoclastogenesis: A Review. Biomolecules. 2023 Jun 28;13(7):1050.
91. Read A, Schröder M. The Unfolded Protein Response: An Overview. Biology (Basel). 2021 Apr 29;10(5):384.
92. Briggs MD, Dennis EP, Dietmar HF, Pirog KA. New developments in chondrocyte ER-stress and related diseases. F1000Res. 2020 Apr 24;9:290.
93. Hughes A, Oxford A, Tawara K, Jorcyk C, Oxford J. Endoplasmic Reticulum Stress and Unfolded Protein Response in Cartilage Pathophysiology; Contributing Factors to Apoptosis and Osteoarthritis. Int J Mol Sci. 2017 Mar 20;18(3):665.

94. Kan S, Duan M, Liu Y, Wang C, Xie J. Role of Mitochondria in Physiology of Chondrocytes and Diseases of Osteoarthritis and Rheumatoid Arthritis. Cartilage. 2021 Dec 11;13(2_suppl):1102S-1121S.
95. Kowaltowski AJ, de Souza-Pinto NC, Castilho RF, Vercesi AE. Mitochondria and reactive oxygen species. Free Radic Biol Med. 2009 Aug;47(4):333–43.
96. Palma FR, Gantner BN, Sakiyama MJ, Kayzuka C, Shukla S, Lacchini R, et al. ROS production by mitochondria: function or dysfunction? Oncogene. 2024 Jan 29;43(5):295–303.
97. Ray PD, Huang BW, Tsuji Y. Reactive oxygen species (ROS) homeostasis and redox regulation in cellular signaling. Cell Signal. 2012 May;24(5):981–90.
98. Tirichen H, Yaigoub H, Xu W, Wu C, Li R, Li Y. Mitochondrial Reactive Oxygen Species and Their Contribution in Chronic Kidney Disease Progression Through Oxidative Stress. Front Physiol. 2021 Apr 23;12.
99. Zhao C. Cell culture: *in vitro* model system and a promising path to *in vivo* applications. J Histotechnol. 2023 Jan 2;46(1):1–4.
100. Kutz WE, Gong Y, Warman ML. *WISP3* , the Gene Responsible for the Human Skeletal Disease Progressive Pseudorheumatoid Dysplasia, Is Not Essential for Skeletal Function in Mice. Mol Cell Biol. 2005 Jan 1;25(1):414–21.
101. Zhang K, Yin X, Shi K, Zhang S, Wang J, Zhao S, et al. A high-efficiency method for site-directed mutagenesis of large plasmids based on large DNA fragment amplification and recombinational ligation. Sci Rep. 2021 May 17;11(1):10454.
102. Bachman J. Site-Directed Mutagenesis. In 2013. p. 241–8.
103. Carrigan PE, Ballar P, Tuzmen S. Site-Directed Mutagenesis. In 2011. p. 107–24.
104. Edelheit O, Hanukoglu A, Hanukoglu I. Simple and efficient site-directed mutagenesis using two single-primer reactions in parallel to generate mutants for protein structure-function studies. BMC Biotechnol. 2009 Dec 30;9(1):61.
105. Buß O, Rudat J, Ochsenreither K. FoldX as Protein Engineering Tool: Better Than Random Based Approaches? Comput Struct Biotechnol J. 2018;16:25–33.
106. Schymkowitz J, Borg J, Stricher F, Nys R, Rousseau F, Serrano L. The FoldX web server: an online force field. Nucleic Acids Res. 2005 Jul 1;33(Web Server):W382–8.
107. McKinnon KM. Flow Cytometry: An Overview. Curr Protoc Immunol. 2018 Jan 21;120(1).
108. Padhan DK, Sengupta A, Patra M, Ganguly A, Mahata SK, Sen M. CCN6 regulates mitochondrial respiratory complex assembly and activity. The FASEB Journal. 2020 Sep 20;34(9):12163–76.
109. Sundqvist M, Christenson K, Björnsdottir H, Osla V, Karlsson A, Dahlgren C, et al. Elevated Mitochondrial Reactive Oxygen Species and Cellular Redox Imbalance in Human NADPH-Oxidase-Deficient Phagocytes. Front Immunol. 2017 Dec 21;8.

110. Hong JY, Kim H, Lee J, Jeon WJ, Baek SH, Ha IH. Neurotherapeutic Effect of Inula britannica var. Chinensis against H2O2-Induced Oxidative Stress and Mitochondrial Dysfunction in Cortical Neurons. Antioxidants. 2021 Mar 3;10(3):375.
111. Kim D, Kim Y, Son N, Kang C, Kim A. Recent omics technologies and their emerging applications for personalised medicine. IET Syst Biol. 2017 Jun 19;11(3):87–98.
112. Pendergrass W, Wolf N, Poot M. Efficacy of MitoTracker GreenTM and CMXrosamine to measure changes in mitochondrial membrane potentials in living cells and tissues. Cytometry Part A. 2004 Oct 26;61A(2):162–9.
113. D'Agostino N, Li W, Wang D. High-throughput transcriptomics. Sci Rep. 2022 Nov 29;12(1):20313.
114. Conesa A, Madrigal P, Tarazona S, Gomez-Cabrero D, Cervera A, McPherson A, et al. A survey of best practices for RNA-seq data analysis. Genome Biol. 2016 Dec 26;17(1):13.
115. Tzec-Interián JA, González-Padilla D, Góngora-Castillo EB. Bioinformatics perspectives on transcriptomics: A comprehensive review of bulk and single-cell RNA sequencing analyses. Quantitative Biology. 2025 Jun 6;13(2).
116. McGettigan PA. Transcriptomics in the RNA-seq era. Curr Opin Chem Biol. 2013 Feb;17(1):4–11.
117. Cutillas PR, Timms JF, editors. LC-MS/MS in Proteomics. Vol. 658. Totowa, NJ: Humana Press; 2010.
118. Bian Y, Bayer FP, Chang YC, Meng C, Hoefer S, Deng N, et al. Robust Microflow LC-MS/MS for Proteome Analysis: 38 000 Runs and Counting. Anal Chem. 2021 Mar 2;93(8):3686–90.
119. Bian Y, Zheng R, Bayer FP, Wong C, Chang YC, Meng C, et al. Robust, reproducible and quantitative analysis of thousands of proteomes by micro-flow LC–MS/MS. Nat Commun. 2020 Jan 9;11(1):157.
120. Richards AL, Eckhardt M, Krogan NJ. Mass spectrometry-based protein–protein interaction networks for the study of human diseases. Mol Syst Biol. 2021 Jan 12;17(1).
121. Wu S, Zhang S, Liu CM, Fernie AR, Yan S. Recent Advances in Mass Spectrometry-Based Protein Interactome Studies. Molecular & Cellular Proteomics. 2025 Jan;24(1):100887.
122. Delgado J, Radusky LG, Cianferoni D, Serrano L. FoldX 5.0: working with RNA, small molecules and a new graphical interface. Bioinformatics. 2019 Oct 15;35(20):4168–9.
123. Humphrey W, Dalke A, Schulten K. VMD: Visual molecular dynamics. J Mol Graph. 1996 Feb;14(1):33–8.
124. Li C, Wen A, Shen B, Lu J, Huang Y, Chang Y. FastCloning: a highly simplified, purification-free, sequence- and ligation-independent PCR cloning method. BMC Biotechnol. 2011 Dec 12;11(1):92.
125. Livak KJ, Schmittgen TD. Analysis of Relative Gene Expression Data Using Real-Time Quantitative PCR and the 2−ΔΔCT Method. Methods. 2001 Dec;25(4):402–8.
126. Priel Avi. Snake and spider toxins : methods and protocols. Humana Press; 2020. 293 p.

127. Luo D, Huang L, Bai B, Zhang H, Liu W, Wen B, et al. Sequential drug-release microsphere system for scarless wound healing. Mater Today Bio. 2025 Dec;35:102310.
128. Bormann T, Maus R, Stolper J, Tort Tarrés M, Brandenberger C, Wedekind D, et al. Role of matrix metalloprotease-2 and MMP-9 in experimental lung fibrosis in mice. Respir Res. 2022 Dec 8;23(1):180.
129. BOLTE S, CORDELIÈRES FP. A guided tour into subcellular colocalization analysis in light microscopy. J Microsc. 2006 Dec 20;224(3):213–32.
130. Bressert Eli. SciPy and NumPy. O'Reilly; 2013. 57 p.
131. Zhou F, Sun J, Ye L, Jiang T, Li W, Su C, et al. Fibronectin promotes tumor angiogenesis and progression of non-small-cell lung cancer by elevating WISP3 expression via FAK/MAPK/HIF-1α axis and activating wnt signaling pathway. Exp Hematol Oncol. 2023 Jul 19;12(1):61.
132. Marzin P, Cormier-Daire V. New perspectives on the treatment of skeletal dysplasia. Ther Adv Endocrinol Metab. 2020 Jan 3;11.
133. Ritz C, Spiess AN. *qpcR* : an R package for sigmoidal model selection in quantitative real-time polymerase chain reaction analysis. Bioinformatics. 2008 Jul 1;24(13):1549–51.
134. Carter MS, Li S, Wilkinson MF. A splicing-dependent regulatory mechanism that detects translation signals. EMBO J. 1996 Nov;15(21):5965–75.
135. Popp MWL, Maquat LE. Organizing Principles of Mammalian Nonsense-Mediated mRNA Decay. Annu Rev Genet. 2013 Nov 23;47(1):139–65.
136. Schweingruber C, Rufener SC, Zünd D, Yamashita A, Mühlemann O. Nonsense-mediated mRNA decay — Mechanisms of substrate mRNA recognition and degradation in mammalian cells. Biochimica et Biophysica Acta (BBA) - Gene Regulatory Mechanisms. 2013 Jun;1829(6–7):612–23.
137. Buß O, Muller D, Jager S, Rudat J, Rabe KS. Improvement in the Thermostability of a β-Amino Acid Converting ω-Transaminase by Using FoldX. ChemBioChem. 2018 Feb 16;19(4):379–87.
138. Petrosino M, Novak L, Pasquo A, Chiaraluce R, Turina P, Capriotti E, et al. Analysis and Interpretation of the Impact of Missense Variants in Cancer. Int J Mol Sci. 2021 May 21;22(11):5416.
139. Tokuriki N, Stricher F, Serrano L, Tawfik DS. How Protein Stability and New Functions Trade Off. PLoS Comput Biol. 2008 Feb 29;4(2):e1000002.
140. Hernández IM, Dehouck Y, Bastolla U, López-Blanco JR, Chacón P. Predicting protein stability changes upon mutation using a simple orientational potential. Bioinformatics. 2023 Jan 1;39(1).
141. Rehm HL, Berg JS, Brooks LD, Bustamante CD, Evans JP, Landrum MJ, et al. ClinGen — The Clinical Genome Resource. New England Journal of Medicine. 2015 Jun 4;372(23):2235–42.
142. Monsen VT, Attramadal H. Structural insights into regulation of CCN protein activities and functions. J Cell Commun Signal. 2023 Jun 28;17(2):371–90.

143. Ehl S, Uhl M, Berner R, Bonaf L, Superti-Furga A, Kirchhoff A. Clinical, radiographic, and genetic diagnosis of progressive pseudorheumatoid dysplasia in a patient with severe polyarthropathy. Rheumatol Int. 2004 Jan 1;24(1):53–6.
144. Li C, Alemany-Ribes M, Raftery RM, Nwoko U, Warman ML, Craft AM. Directed differentiation of human pluripotent stem cells into articular cartilage reveals effects caused by absence of WISP3, the gene responsible for progressive pseudorheumatoid arthropathy of childhood. Ann Rheum Dis. 2023 Dec;82(12):1547–57.
145. Lechuga CG, Hernández-Nazara ZH, Rosales JAD, Morris ER, Rincón AR, Rivas-Estilla AM, et al. TGF-β1 modulates matrix metalloproteinase-13 expression in hepatic stellate cells by complex mechanisms involving p38MAPK, PI3-kinase, AKT, and p70 S6k. American Journal of Physiology-Gastrointestinal and Liver Physiology. 2004 Nov;287(5):G974–87.
146. Lu Y, Xu Y, Yin Z, Yang X, Jiang Y, Gui J. Chondrocyte Migration Affects Tissue-Engineered Cartilage Integration by Activating the Signal Transduction Pathways Involving Src, PLCγ1, and ERK1/2. Tissue Eng Part A. 2013 Nov;19(21–22):2506–16.
147. Chen S, He T, Zhong Y, Chen M, Yao Q, Chen D, et al. Roles of focal adhesion proteins in skeleton and diseases. Acta Pharm Sin B. 2023 Mar;13(3):998–1013.
148. YU Y, HU M, XING X, LI F, SONG Y, LUO Y, et al. Identification of a mutation in the WISP3 gene in three unrelated families with progressive pseudorheumatoid dysplasia. Mol Med Rep. 2015 Jul;12(1):419–25.
149. Cockburn CG, Barnes MJ. Characterization of Thrombospondin Binding to Collagen (Type I) Fibres: Role of Collagen Telopeptides. Matrix. 1991 Jun;11(3):168–76.
150. Murphy-Ullrich JE. Thrombospondin 1 and Its Diverse Roles as a Regulator of Extracellular Matrix in Fibrotic Disease. Journal of Histochemistry & Cytochemistry. 2019 Sep 22;67(9):683–99.
151. Jiang Z, Wang H, Zhang Z, Pan J, Yuan H. Cartilage targeting therapy with reactive oxygen species-responsive nanocarrier for osteoarthritis. J Nanobiotechnology. 2022 Sep 19;20(1):419.
152. Chen X, Shi C, He M, Xiong S, Xia X. Endoplasmic reticulum stress: molecular mechanism and therapeutic targets. Signal Transduct Target Ther. 2023 Sep 15;8(1):352.
153. Lamandé SR, Bateman JF. Genetic Disorders of the Extracellular Matrix. Anat Rec. 2020 Jun 6;303(6):1527–42.
154. Tran HC, Van Aken O. Mitochondrial unfolded protein-related responses across kingdoms: similar problems, different regulators. Mitochondrion. 2020 Jul;53:166–77.
155. Falahatpisheh H, Nanez A, Montoya-Durango D, Qian Y, Tiffany-Castiglioni E, Ramos KS. Activation profiles of HSPA5 during the glomerular mesangial cell stress response to chemical injury. Cell Stress Chaperones. 2007;12(3):209.
156. Huang Y, Arora K, Mun KS, Yang F, Moon C, Yarlagadda S, et al. Targeting DNAJB9, a novel ER luminal co-chaperone, to rescue ΔF508-CFTR. Sci Rep. 2019 Jul 8;9(1):9808.

157. Paredes F, Parra V, Torrealba N, Navarro-Marquez M, Gatica D, Bravo-Sagua R, et al. HERPUD1 protects against oxidative stress-induced apoptosis through downregulation of the inositol 1,4,5-trisphosphate receptor. Free Radic Biol Med. 2016 Jan;90:206–18.
158. Liu S, Li Z, Lan S, Hao H, Baz AA, Yan X, et al. The Dual Roles of Activating Transcription Factor 3 (ATF3) in Inflammation, Apoptosis, Ferroptosis, and Pathogen Infection Responses. Int J Mol Sci. 2024 Jan 9;25(2):824.
159. Turpin J, El-Safadi D, Lebeau G, Frumence E, Desprès P, Viranaïcken W, et al. CHOP Pro-Apoptotic Transcriptional Program in Response to ER Stress Is Hacked by Zika Virus. Int J Mol Sci. 2021 Apr 3;22(7):3750.
160. Sojoudi K, Azizi H, Skutella T. A Study of Dual Function and Expression Pattern of *Klf4* between Two Different Processes of Differentiation and Maintenance of Pluripotency in Spermatogonial Stem Cells. Andrologia. 2024 Jan 12;2024(1).
161. Jackson JT, Mulazzani E, Nutt SL, Masters SL. The role of PLCγ2 in immunological disorders, cancer, and neurodegeneration. Journal of Biological Chemistry. 2021 Aug;297(2):100905.
162. ANP32CP Acidic Nuclear Phosphoprotein 32 Family Member C, Pseudogene [Internet]. [cited 2025 Oct 28]. Available from: https://www.ncbi.nlm.nih.gov/gene?Db=gene&Cmd=DetailsSearch&Term=23520
163. CSNK1A1L Casein Kinase 1 Alpha 1 like [Internet]. [cited 2025 Oct 28]. Available from: https://www.ncbi.nlm.nih.gov/gene?Db=gene&Cmd=DetailsSearch&Term=122011 (
164. NME2P1 NME2 Pseudogene 1 [Internet]. [cited 2025 Oct 28]. Available from: https://www.genecards.org/cgi-bin/carddisp.pl?gene=NME2P1
165. Qazi S, Jit BP, Das A, Karthikeyan M, Saxena A, Ray MD, et al. BESFA: bioinformatics based evolutionary, structural & functional analysis of Prostate, Placenta, Ovary, Testis, and Embryo (POTE) paralogs. Heliyon. 2022 Sep;8(9):e10476.
166. Wang X, Zhang C, Song H, Yuan J, Zhang X, Yuan Y, et al. Characterization of LIMA1 and its emerging roles and potential therapeutic prospects in cancers. Front Oncol. 2023 May 19;13.
167. Huang H, Du Y, Zhao D, Chen K. The Relationship between the Prognostic Marker LIMA1 in Head and Neck Squamous Cell Carcinoma and Immune Infiltration. J Oncol. 2022 Aug 31;2022:1–14.
168. Mototani H, Mabuchi A, Saito S, Fujioka M, Iida A, Takatori Y, et al. A functional single nucleotide polymorphism in the core promoter region of CALM1 is associated with hip osteoarthritis in Japanese. Hum Mol Genet. 2005 Apr 15;14(8):1009–17.
169. Loughlin J, Sinsheimer JS, Carr A, Chapman K. The CALM1 core promoter polymorphism is not associated with hip osteoarthritis in a United Kingdom Caucasian population. Osteoarthritis Cartilage. 2006 Mar;14(3):295–8.
170. Li CM, Kang J, Baek J, Kim Y, Park H, Jung YK. Cytosolic FKBPL and ER-resident CKAP4 co-regulates ER-phagy and protein secretion. Nat Commun. 2024 Sep 9;15(1):7886.

171. Despotidis M, Lyros O, Driva TS, Sarantis P, Kapetanakis EI, Mylonakis A, et al. DKK1 and Its Receptors in Esophageal Adenocarcinoma: A Promising Molecular Target. Diagnostics. 2025 Jan 2;15(1):85.
172. Harada T, Sada R, Osugi Y, Matsumoto S, Matsuda T, Hayashi-Nishino M, et al. Palmitoylated CKAP4 regulates mitochondrial functions through an interaction with VDAC2 at ER–mitochondria contact sites. J Cell Sci. 2020 Nov 1;133(21).
173. Xu K, Sun S, Yan M, Cui J, Yang Y, Li W, et al. DDX5 and DDX17—multifaceted proteins in the regulation of tumorigenesis and tumor progression. Front Oncol. 2022 Aug 3;12.
174. Ma L, Zhao X, Wang S, Zheng Y, Yang S, Hou Y, et al. Decreased expression of DEAD-Box helicase 5 inhibits esophageal squamous cell carcinomas by regulating endoplasmic reticulum stress and autophagy. Biochem Biophys Res Commun. 2020 Dec;533(4):1449–56.
175. Lambrecht S, Dhaenens M, Almqvist F, Verdonk P, Verbruggen G, Deforce D, et al. Proteome characterization of human articular chondrocytes leads to novel insights in the function of small heat-shock proteins in chondrocyte homeostasis. Osteoarthritis Cartilage. 2010 Mar;18(3):440–6.
176. Bruey JM, Ducasse C, Bonniaud P, Ravagnan L, Susin SA, Diaz-Latoud C, et al. Hsp27 negatively regulates cell death by interacting with cytochrome c. Nat Cell Biol. 2000 Sep 17;2(9):645–52.
177. Fu Q, Li Y, Shi C. HSPB1 as an RNA-binding protein mediates the pathological process of osteoarthritis. J Orthop Surg Res. 2024 Mar 1;19(1):156.

APPENDIX 1

A

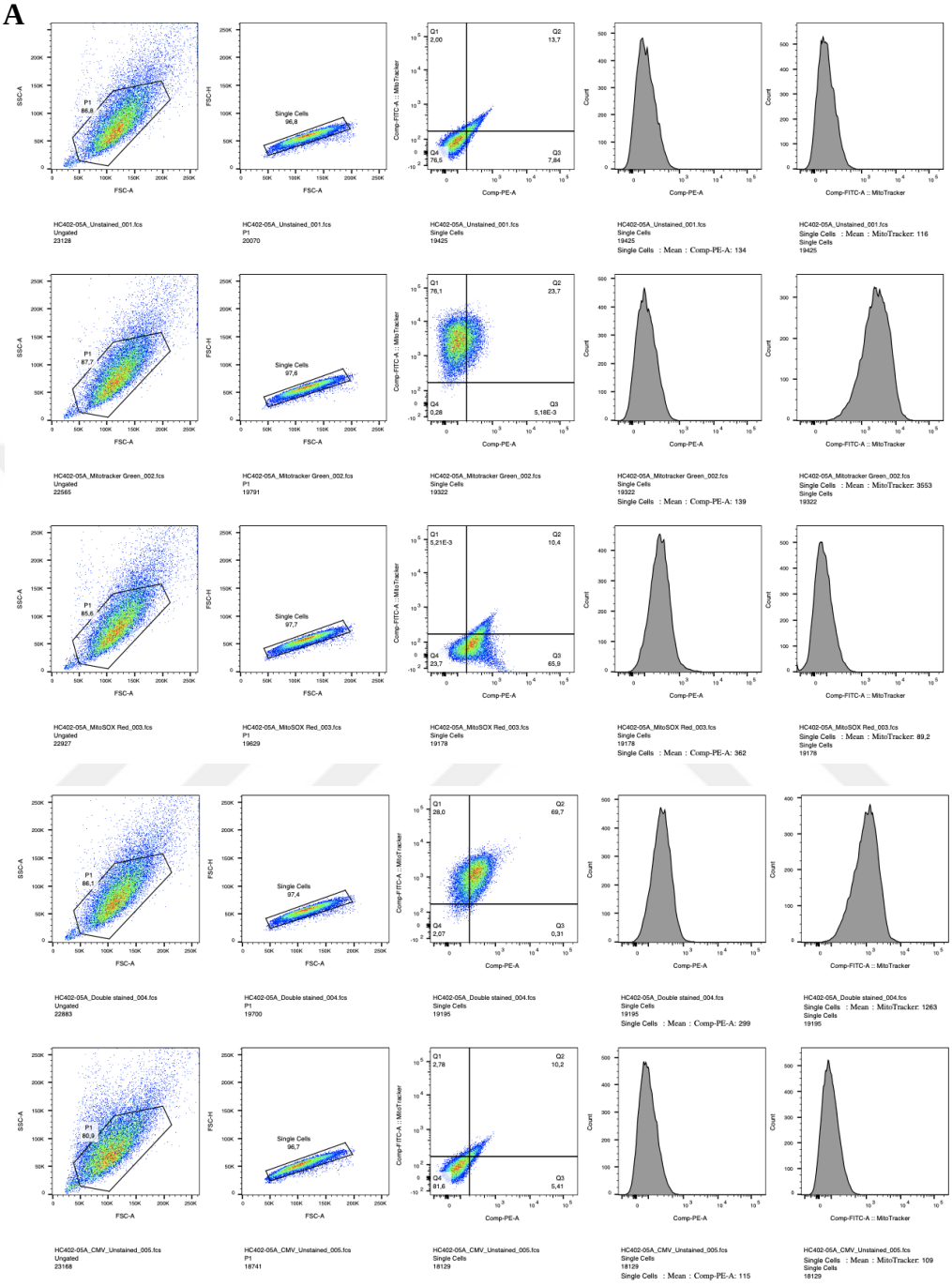
SSC-A
FSC-A
P1
86,8
FSC-H
Single Cells
96,8
Comp-FITC-A :: MitoTracker
Comp-PE-A
Q1
2,00
Q2
13,7
Q4
76,5
Q3
7,84
Count
HC402-05A_Unstained_001.fcs
Ungated
23128
P1
20070
Single Cells
19425
Single Cells : Mean : Comp-PE-A: 134
Single Cells : Mean : MitoTracker: 116
P1
87,7
97,6
Q1
76,1
Q2
23,7
Q4
0,28
Q3
5,18E-3
HC402-05A_Mitotracker Green_002.fcs
22565
19791
19322
Single Cells : Mean : Comp-PE-A: 139
Single Cells : Mean : MitoTracker: 3553
P1
85,6
97,7
Q1
5,21E-3
Q2
10,4
Q4
23,7
Q3
65,9
HC402-05A_MitoSOX Red_003.fcs
22927
19629
19178
Single Cells : Mean : Comp-PE-A: 362
Single Cells : Mean : MitoTracker: 89,2
P1
86,1
97,4
Q1
28,0
Q2
69,7
Q4
2,07
Q3
0,31
HC402-05A_Double stained_004.fcs
22883
19700
19195
Single Cells : Mean : Comp-PE-A: 299
Single Cells : Mean : MitoTracker: 1263
P1
80,9
96,7
Q1
2,78
Q2
10,2
Q4
81,6
Q3
5,41
HC402-05A_CMV_Unstained_005.fcs
23168
18741
18129
Single Cells : Mean : Comp-PE-A: 115
Single Cells : Mean : MitoTracker: 109

APPENDIX 1 (continued)

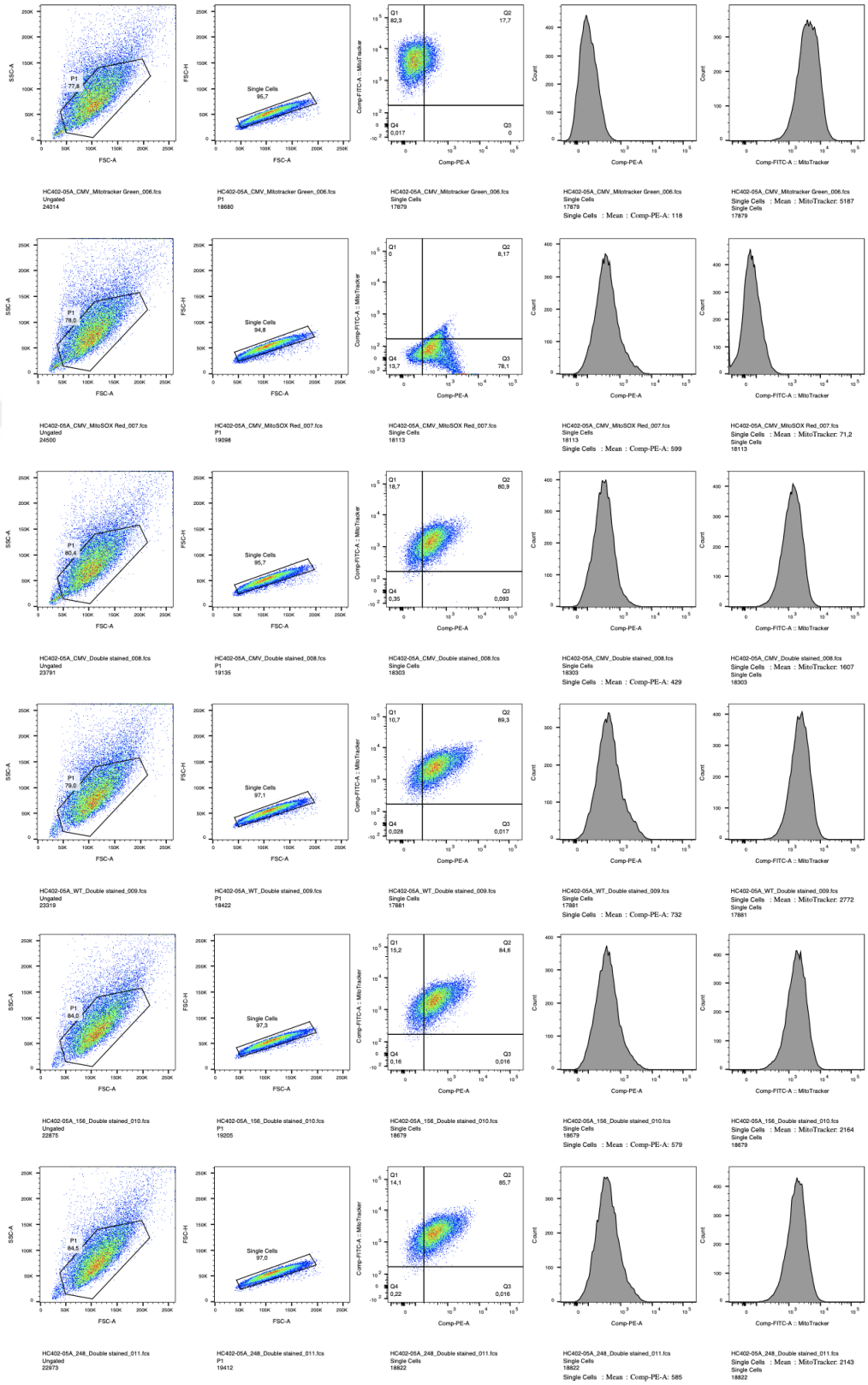

APPENDIX 1 (continued)

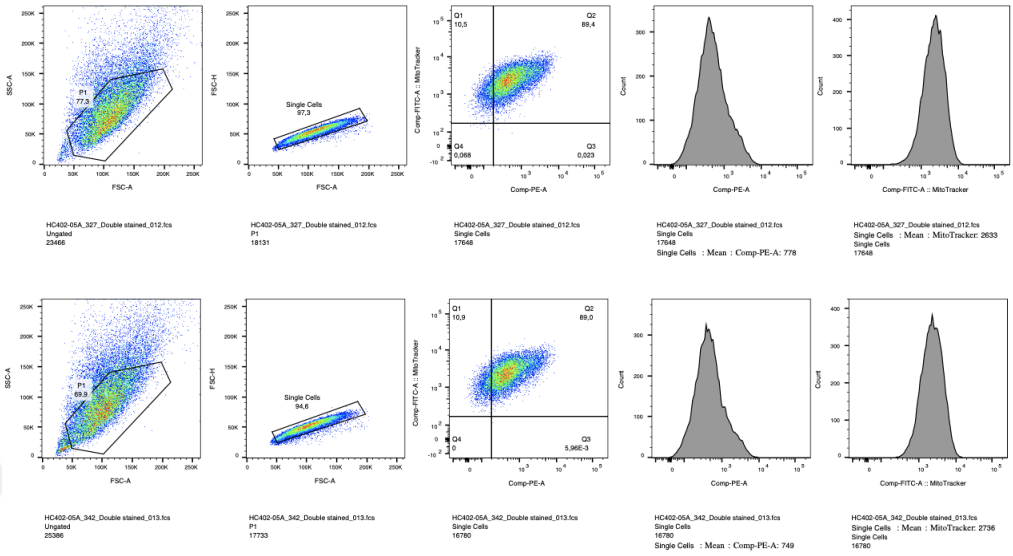

B

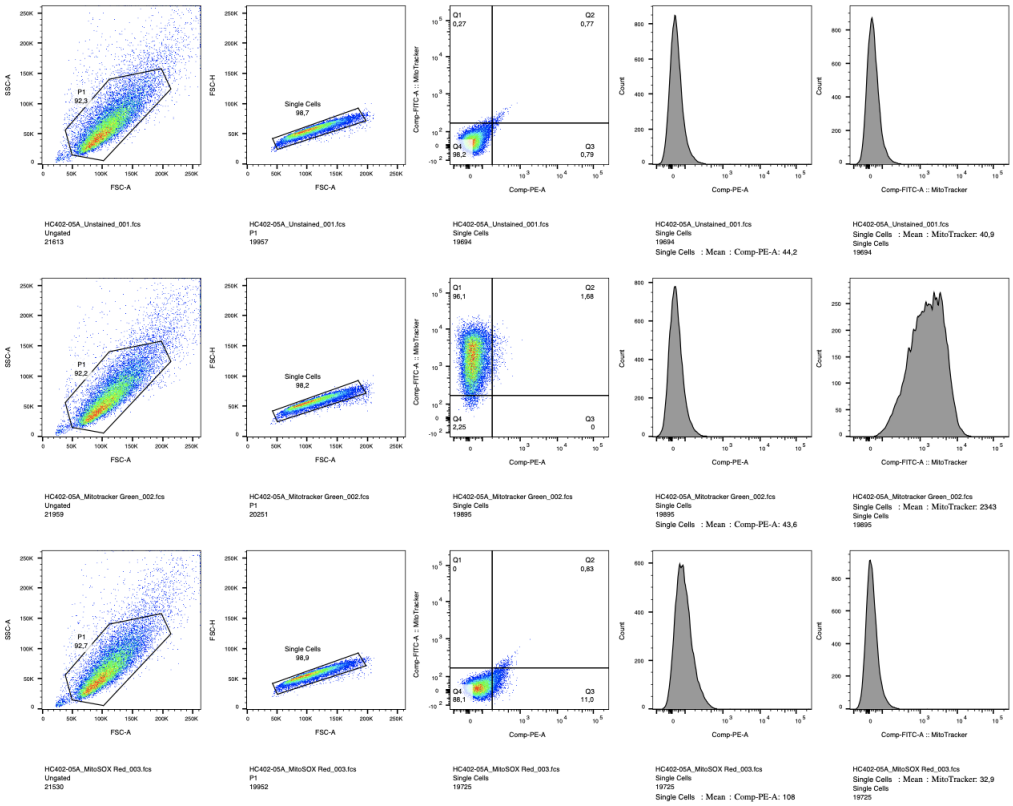

APPENDIX 1 (continued)

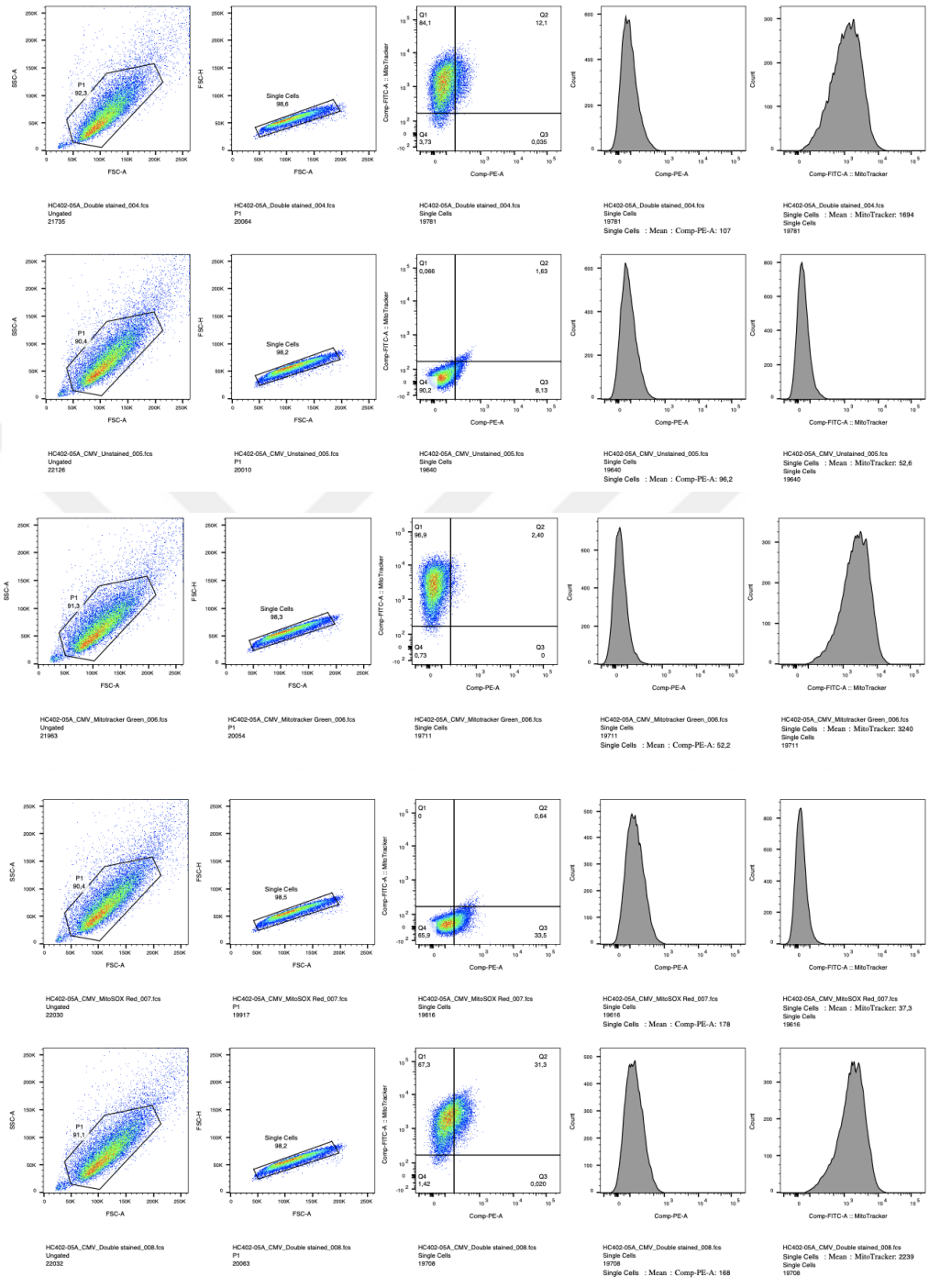

APPENDIX 1 (continued)

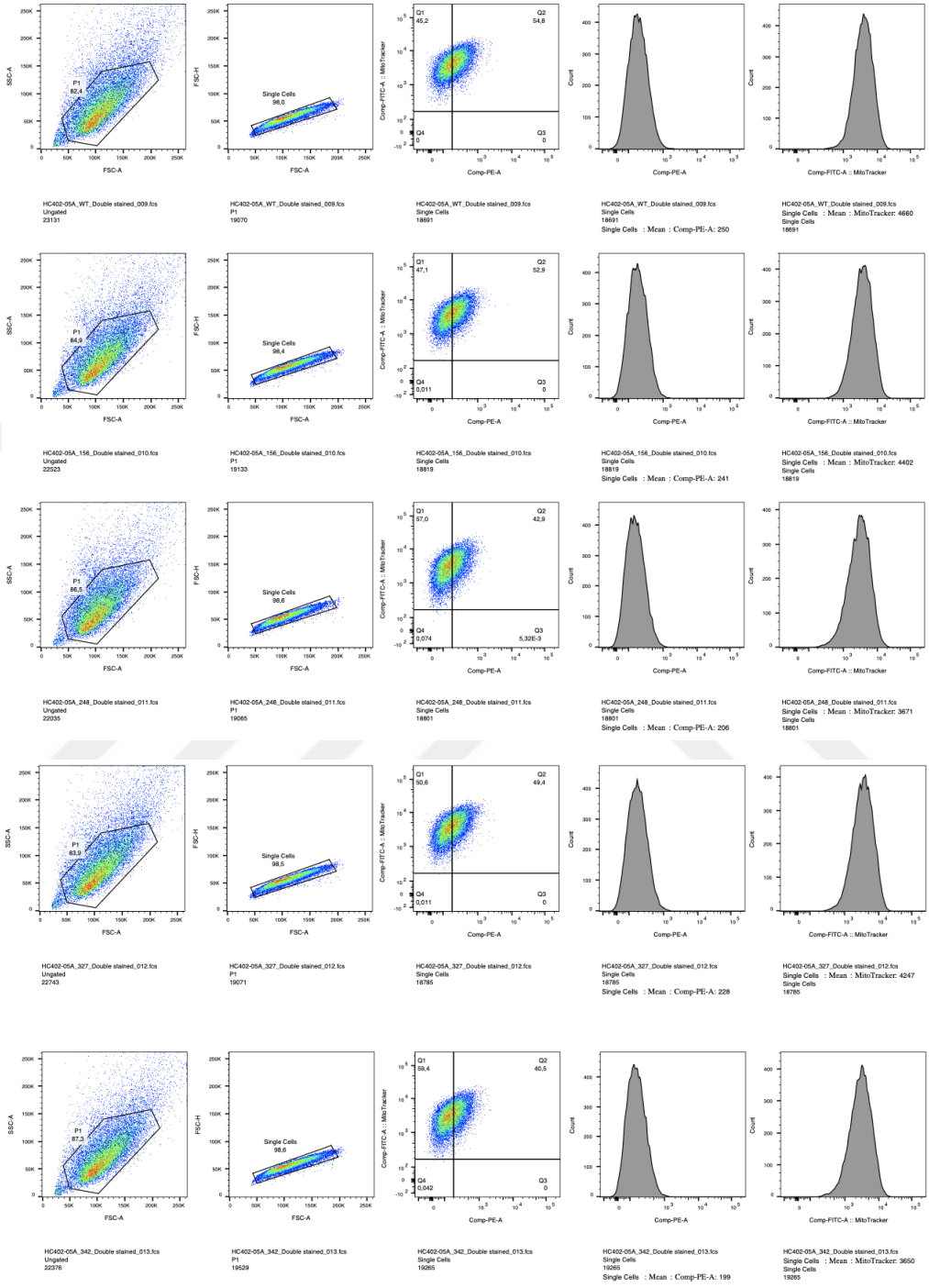

Figure 28. Flow cytometric analysis of mitochondrial parameters in PPD chondrocyte models. (A–B) Human chondrocytes transfected with WISP3 variants or control plasmids (pcDNA3.1) were stained with MitoTracker Green and MitoSOX Red to evaluate mitochondrial mass and superoxide levels. Flow cytometry was performed using FITC and PE channels. Control and pcDNA3.1-transfected cells were analyzed with both single and double staining, while variant-expressing cells were assessed with double staining only. Panels display representative ungated and single-cell populations, quadrant distribution (Q1–Q4), and corresponding MFI values (n = 2).

APPENDIX 2

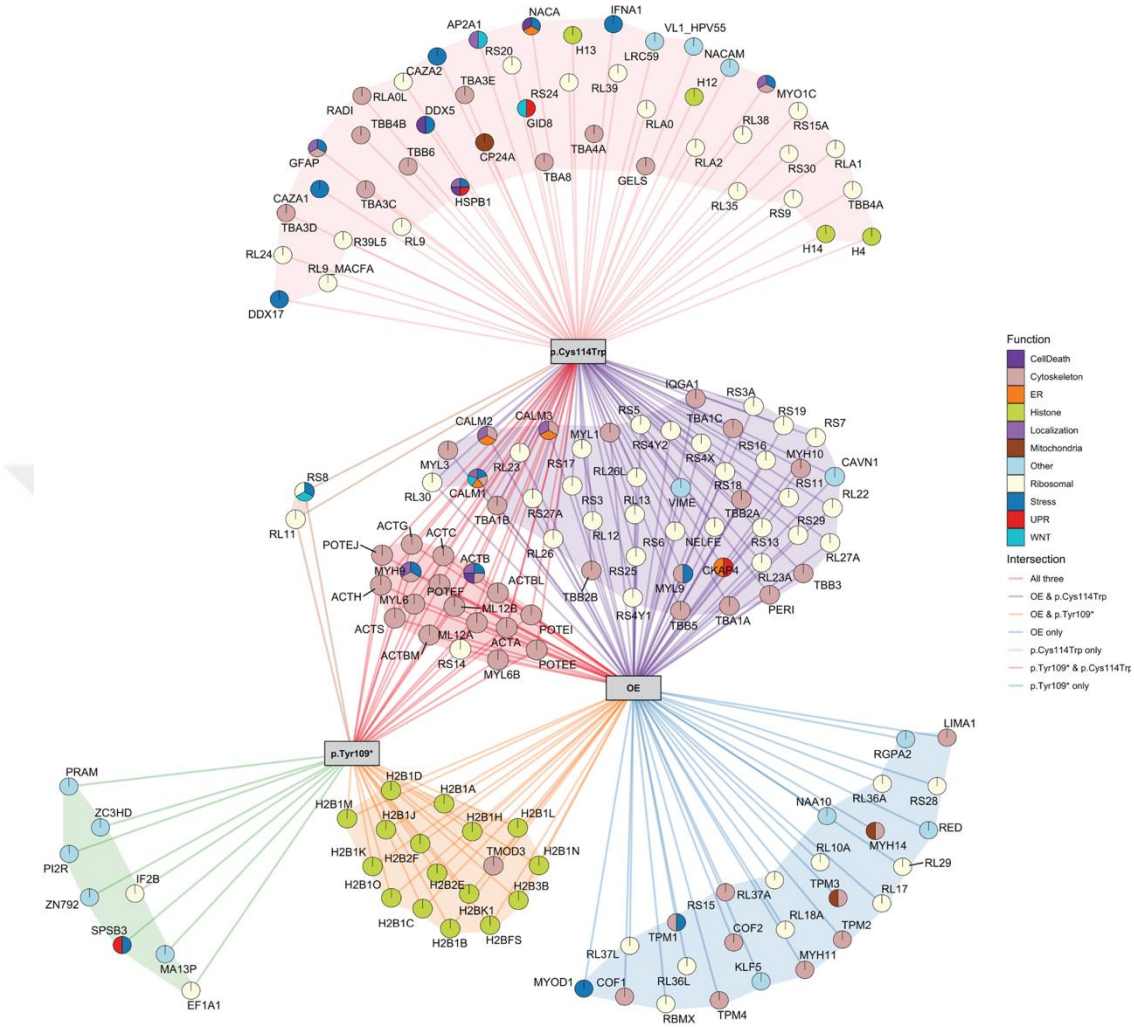

Figure 29. Whole PPI network of WISP3 variants identified by LC-MS/MS. Whole PPI network of WISP3 variants identified by LC–MS/MS. Expanded, unfiltered protein–protein interaction (PPI) map generated from co-immunoprecipitation of HA-tagged WISP3 constructs (OE, p.Cys114Trp, and p.Tyr109*) in human chondrocytes. Nodes represent unique interactors grouped by variant-specific or shared associations, and node colors indicate functional categories (cytoskeletal, mitochondrial, ER-associated, ribosomal, stress-related). The network depicts the distinct interaction profile of p.Cys114Trp relative to OE.

APPENDIX 2 (continued)

Table 18. Filtered list of WISP3-interacting proteins identified by LC-MS/MS

Only p.Cys114Trp	p.Cys114Trp and OE	p.Cys114Trp, p.Tyr109* and OE	Only OE	p.Tyr109* and OE	Only p.Tyr109*
CAZA2	TBB2A	ACTG	TPM3	TMOD3	ZC3HD
GELS	TBA1C	ACTS	RED		PI2R
TBA3D	MYL9	ACTA	COF1		SPSB3
DDX5	CALM1	ACTBM	MYH11		ZN792
AP2A1	MYH10	MYL6	NAA10		PRAM
NACAM	CAVN1	ACTC	LIMA1		
IGD8	YML3	MYL6B	COF2		
LRC59	TBB2B	ML12B	TPM4		
HSPB1	TBA1A	ACTBL	RGPA2		
MYO1C	TBA1B	ML12A	MYOD1		
TBA8	CALM3	ACTH	RS15		
NACAM	VIME	ACTB	KLF5		
CAZA1	CKAP4	POTEI	TPM2		
TBA3C	TBB5	POTEF	MYH14		
RADI	TBB3	POTEE	TPM1		
IFNA1	MYL1	MYH9			
TBB4B	IQGA1	POTEJ			
VL1_HPV55	PERI				
TBB6	CALM2				
CP24A					
TBA3E					
TBA4A					
DDX17					
GFAP					

8 CURRICULUM VITAE

Personal Information